Structure and Dynamics of Small Molecules and Anions:

Negative-ion photoelectron spectroscopy

by

Elisa M. Miller

B.A., Boston University, 2005

A thesis submitted to the

Faculty of the Graduate School of the

University of Colorado in partial fulfillment

of the requirements for the degree of

Doctor of Philosophy

Department of Chemistry and Biochemistry

This thesis entitled:

Structure and Dynamics of Small Molecules and Anions:

Negative-ion photoelectron spectroscopy

written by Elisa M. Miller

has been approved for the Department of Chemistry and Biochemistry by

_____

W. Carl Lineberger

_____

Veronica M. Bierbaum

Date: _____

The final copy of this thesis has been examined by the signatories, and we find that both the content and the form meet acceptable presentation standards of scholarly work in the above mentioned discipline.

Miller, Elisa M. (Ph.D. Physical Chemistry)

Structure and Dynamics of Small Molecules and Anions: Negative-ion photoelectron spectroscopy

Thesis directed by Professor W. Carl Lineberger

Photoelectron spectroscopy of gas-phase anions is utilized to study the spectroscopic and dynamic properties of anions and anionic clusters. The photoelectron spectrum of $IBr^-(\tilde{X}^2\Sigma^+)$ leads to more accurate measurements of a number of molecular properties, such as the electron affinity of IBr (EA(IBr) = 2.512±0.003 eV), equilibrium geometry of the anion ground state ($R_e(I–Br^-)$ = 3.01±0.01 Å), and dissociation energy of the anion ground state ($D_0(I–Br^-)$ = 0.966±0.003 eV). The photoelectron spectrum of $IBr^-(CO_2)_n$, n = 1 – 3, demonstrates minimal perturbation to the IBr^- electronic structure, and the EAs for solvated $IBr(CO_2)_n$, n = 1 – 3, are determined. The presence of the CO_2 influences the dissociation dynamics along two excited states of IBr^- by enabling nonadiabatic transitions. Time-resolved photoelectron spectra of IBr^- and $IBr^-(CO_2)$ are taken to measure these dissociation dynamics, which when combined with theory leads to a mechanism. The solvation energy of CO_2 and the ability of CO_2 to temporarily acquire partial charge as it bends facilitate the charge transfer in the two photoexcitation/ photodissociation channels studied.

Photoelectron spectroscopy of ICN^- $(\tilde{X}^2\Sigma^+)$ probes transitions to the ground state and first five excited states of neutral ICN. The first three excited states and a conical intersection region between the $^3\Pi_{0^+}$ and $^1\Pi_1$ states are spectroscopically resolved. Through thermochemical cycles

involving narrow transitions to excited states, the EA(ICN) is found to be 1.34(+.04/-.02) eV and the $D_0(ICN^-)$ equals 0.83(+.04/-.02) eV. In addition, four spectral peaks are observed with photoelectron kinetic energies of ~0, ~45, ~70, and ~150 – 200 meV, and the kinetic energy is unchanged as the photodetachment photon energy is varied from 2.5 to 4.2 eV. These autodetachment features are a result of photoexcited ICN^- converting internal energy into CN rotation followed by a quasi-thermionic emission of electrons to produce neutral ICN/INC in its ground electronic state. The autodetachment features persist when ICN^- is solvated by Ar or CO_2, indicating that solvation does not modify the autodetachment mechanism. In addition to these investigations, current projects are in progress, such as HO_3^-, that require abundant Ar cooling and an entrainment block as part of the anion source.

To my Yia Yia and Papou, and my Reddinger Grandparents whom I wish I had met.

Acknowledgements

First, I would like to thank Carl for all of his support and guidance over the past seven years. Thank you for allowing me to be a part of your group and providing me with so many opportunities to network and meet various people, such as Anne McCoy, Mark Johnson, Marsha Lester, John Stanton, John Maier, and David Osborn. You have created an amazing research family that I am so honored to be a part of. To the Lineberger group, thank you so much for your help with not only science but with life. I have learned so much over the past seven years from interacting with you guys on a daily basis. Specifically, I would like to thank Lenny Sheps for putting up with me for four great years! Thanks to Jack Barbera for preparing me early on for the group and advice on teaching. To Scott Wren, we had some great times together from class to lab to outside of school. To Yu-Ju, thanks for keeping me honest when you joined the group. You really helped to push my understanding of the instrument. To Amanda Case, Kristen Lemke, Josh Martin, and Wilson Gichuhi, thanks for always listening and helping to troubleshoot when needed.

To my committee members, Mathias Weber, Ronnie Bierbaum, Robert Parson, and Heather Lewandowski, as well as Barney Ellison, all of you have helped to shape and guide my graduate career. Thank you so much for always lending an ear and giving advice! Together you have all been involved in one way or another with the Super Group meetings, which has been a great exposure to science. Thank you for that.

In addition to my time researching, I have interacted with some exceptional teachers and people while taking classes at CU and TAing. Thanks to Casey Hynes, Niels Damrauer, and Robert Parson for teaching me physical chemistry. Also, thanks to Mathias for allowing me to

sit in on his quantum class. I really enjoyed my TAing experience and am grateful for the relationships formed with Ronnie Bierbaum, Robert Parson, Margaret Asirvatham, and Elaine Butler.

Without the help of the staff at JILA, I may have gone crazy a few times. Thank you Krista Beck for always being there for me. To the machine shop (especially Hans, Ariel, Todd, Dave, and Blaine), electrical shop (especially James), computing (especially J.R.), and supply office, thank you for saving me so many times!

I could not have made it this far without my Boulder friends (Nicole Pitre, Anthony Morfa, Pat Veres, Melissa Butler, Jess Best, Jesse and Kim Marcum, Dave McAdams, Joey Wolf, Sarah White, Zach Bucuvalas, and CSAW), Boston University friends (Erica Lembo, Jess Blood, and Tessa Benau),and high school friends (Jocelyn Noya Quintana, Laura Mathers, Sara Morrow, and Kristy Hepak). Thank you for being there for me! And to Erica, without all of those long distance minutes, I do not know if I would still be sane. Thanks for always talking to me no matter the time. My education at BU and in HS is critical to me making it this far; so thank you to Amy Mullin, Mort Hoffman, and Bernie Vogler. Researching in Amy's group throughout my undergrad career is the reason that I chose to focus on physical chemistry, so thank you for showing me how much fun p.chem is.

Finally to my family, I owe you the biggest thanks. Without your love and support, I would not have been able to make it this far. You have believed and encouraged me from day one! So thank you. To the Link family (Rick, Debi, Emily, Sarah, Mikie, EJ, and Millie), thank you for loving me without hesitation! I am so grateful to be a part of such an amazing, loving family. To my cousins (Alex, Jackie, Jim, Lynne, Jodie, Jamie, John, Jess, Caitlin, and Lizzy),

aunts (Nana, Marty, Mary Ellen, Mo, Pat, and honorary Rose) and uncles (Nono, Tom, Ed, and Duck), thank you for keeping it real with me. To my brothers and sister-in-laws, (Wendy, Taki, Edward, Lisa, Patrick, Amanda, Andrew, and Ben), thanks for distracting me when needed (especially Ruby, Pearl, and Julia) and supporting me throughout the years in whatever I chose to do, such as wrestling, football, cheerleading, track, and chemistry. Mom and Dad I cannot thank you enough for never letting me quit. You have taught me so much about life but, more importantly, have given me the opportunity to explore and create my life. Thanks for your undying love, support, and advice. And to my Richie, you are my best friend and companion. Thank you for braving the storm with me and supporting me to the end! I love you and cannot thank you enough for all that you have given me. I look forward to our life together and helping each other through many more adventures.

Table of Contents

List of Figures

List of Tables

Chapter I: Introduction to Photoelectron Spectroscopy of Anions

1.1 Overview of Photoelectron Spectroscopy of Anions

The quantum mechanical concepts pertaining to the photoelectric effect are the same as those for photoelectron spectroscopy. In general, the photoelectric effect explains how electrons are ejected from a metal surface by radiation. If the photon energy exceeds the work function of the metal, then electrons can be emitted with a distribution of kinetic energies; the maximum electron kinetic energy (eKE_{max}) is

$$eKE_{max} = h\nu - \varphi, \qquad \text{Eqn. 1.1}$$

where $h\nu$ is the energy of the photon and φ is the work function of the metal. φ is the minimum amount of energy needed to remove an electron from a metal surface. If the energy of the photon does not exceed φ, then an electron is not ejected and remains on the surface even if multiple low-energy photons hit the metal surface. To a first approximation, one electron receives all of the energy from one photon; therefore, the photoelectron distribution is independent of the photon flux and is only dependent on the photon energy.

The technique of photoelectron spectroscopy measures the kinetic energy distribution of ejected electrons (or photoelectrons) to yield a photoelectron spectrum. All of the experiments presented in this thesis are carried out with gas-phase anions as the target; therefore, we photodetach electrons from anions to generate neutral species plus photoelectrons. A schematic of photoelectron spectroscopy of anions (AB^-) is shown in Fig. 1.1. To photodetach an electron, a photon with known energy, hν, interacts with the anion, AB^-. If the photon energy exceeds the

electron binding energy (*eBE*), then electrons are photodetached with a distribution of electron kinetic energies (*eKE*):

$$eKE = h\nu - eBE \; . \qquad \text{Eqn. 1.2}$$

In our experiments, the energy of the photon is measured with an optical spectrometer and the eKE is determined with an electron velocity-map imaging spectrometer. The photoelectron spectroscopy of anions (AB^-) yields information about both the anion (AB^-) and the neutral species (AB).

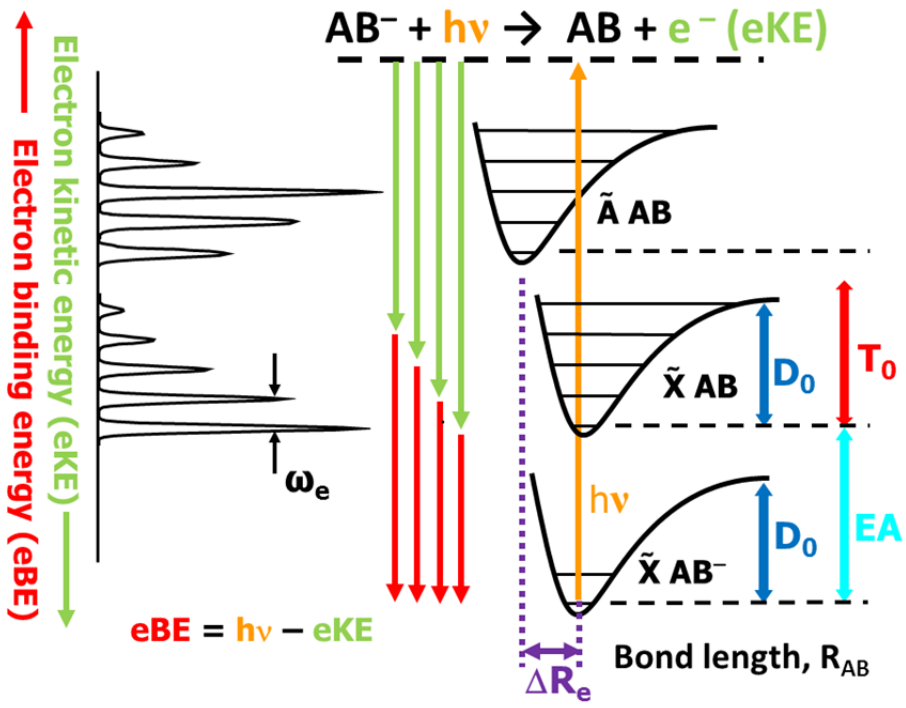

Figure 1.1 Schematic of photoelectron spectroscopy of AB^- and the spectroscopic properties determined from photoelectron spectroscopy of AB^-.

Besides learning about the anion and neutral species, there are some practical advantages to measuring the photoelectron spectra of gas-phase anions, such as the ability to mass-select

anions of choice and the lower photon energy needed to photodetach electrons. By coupling mass spectrometry with photoelectron spectroscopy, an assortment of ions can be separated by mass and charge prior to interacting with the laser radiation. This allows the desired anion to be measured without contamination from other ions. Also, photodetaching an electron from an anion typically requires lower photon energy (< 4 eV) than photodetaching an electron from a neutral (about 10 eV or more).[1] In general, anions have lower electron binding energies because the extra electron increases screening of the positive nucleus, which increases the size of the anion relative to the neutral, thus lowering the binding energy. The lower photon energy required for photodetaching electrons from anions is readily available with commercial laser systems. Measuring the photoelectron spectroscopy of anions generates considerable amounts of information in addition to the binding energy of the electron. Many useful reviews have been written about photoelectron spectroscopy, and the reader is referred to these articles for additional information.[2-8]

1.2 Spectroscopic and Dynamics Investigations

Photoelectron spectroscopy of anions can be summarized in one equation:

$$AB^- + h\nu \rightarrow AB + e^-(eKE) , \qquad \text{Eqn. 1.3}$$

where AB^- is the generic diatomic anion and AB is the generic neutral molecule. In Fig. 1.1, the anion AB^- is prepared in the ground vibrational state ($\upsilon = 0$) of the ground electronic state $\tilde{X}$. To simplify Fig. 1.1, the anion is depicted as being purely in $\upsilon = 0$, and vibrationally excited anions are discussed later in the chapter. After the anion interacts with a photon of energy hν, the electron is ejected from an anion to produce the neutral electronic state, $\tilde{X}$ AB or $\tilde{A}$ AB, plus a corresponding photoelectron. The neutral molecule is left in some ro-vibrational state of $\tilde{X}$ AB

or $\tilde{A}$ AB and the distribution of ejected electrons corresponds to quantized states of the neutral molecule AB . This distribution of photoelectrons is measured to generate the photoelectron spectrum, as shown on the left side of Fig. 1.1. The spectrum can either be reported in terms of eKE or eBE (Eqn. 1.2). However, we typically report the spectra as a function of eBE because this makes the spectra independent of the photon energy used.

In Fig. 1.1, the measured spectrum contains two groups of peaks (vibrational progressions) corresponding to transitions between $\tilde{X}$ AB^- (v = 0) and $\tilde{X}$ AB or $\tilde{A}$ AB. The different shapes of the progressions depend upon the overlap between the anion and neutral states. As the hν arrow indicates in Fig. 1.1, transitions between the anion and neutral AB are "vertical". The geometry of the anion (or Bond Length, R_{AB}) is essentially unchanged as the electron is photodetached from the anion because the nuclei (A and B) are so much heavier than the electron that the nuclei do not have time to respond to the changing electronic structure as the electron is photodetached to yield the neutral molecule. Thus, photoelectron spectroscopy follows the Born-Oppenheimer approximation. Therefore, the neutral electronic states are accessed at the geometry of the anion in its ground electronic and vibrational state.

Interpreting the measured photoelectron spectrum yields a number of properties of both the anion and neutral, where some properties are depicted in Fig. 1.1. The shapes of the vibrational progressions are dictated by the overlap between the vibrational levels of the anion and neutral electronic states. Analysis of the intensity and distribution of the vibrational progressions tells us about the change in equilibrium geometries between the anion and neutral electronic states (ΔR_e). For example, the ΔR_e is small between the ground states of AB^- and AB; therefore, the vibrational progression in Fig. 1.1 that corresponds to transitions to the $\tilde{X}$ AB state

is more narrow with the largest contribution from the $\upsilon'' = 0 \rightarrow \upsilon' = 0$ transition. Conversely, the vibrational progression corresponding to transitions to the Ã AB electronic state is more extended and the vertical detachment energy corresponds to $\upsilon' = 2$, which indicates that the ΔR_e is greater between the $\tilde{X}$ AB^- and Ã AB states. Both vibrational progressions contain peaks which are separated by the vibrational spacing within the neural electronic states, ω_e. Since ΔR_e is small between the ground states of AB^- and AB, the electron affinity (EA) of AB is directly measured, which is the $\tilde{X}$ $AB^-(\upsilon'' = 0) \rightarrow \tilde{X}$ $AB(\upsilon' = 0)$ transition. Also, both spectral envelopes contain transitions to the $\upsilon' = 0$ state; the energy between these two peaks in the photoelectron spectrum is related to the term energy (T_0) splitting between the two neutral states. Finally, these properties are used to give the dissociation energy (D_0) of the anion or neutral molecule.

The generic photoelectron spectrum in Fig. 1.1 is interpreted assuming that all of the anions are populated in the $\upsilon = 0$ state and that rotational energy is not significant. If the anions have population in vibrational states other than $\upsilon = 0$ of the ground electronic state, then transitions from these "hot" anions produce hot bands in the photoelectron spectrum. The presence of hot bands can add congestion to the measured spectrum. However, if the vibrational spacing is large enough in both the anion and neutral electronic states, then the hot bands can be assigned and the vibrational frequency of the anion can be measured. Unlike the vibrational energy spacing, the rotational energy spacing is usually too small to resolve and congests the spectrum. There are higher resolution techniques, such as ZEKE (Zero Electron Kinetic Energy) and SEVI (Slow Electron Velocity-map Imaging), that can more easily resolve rotational energies; however, these techniques tend to be the exception for measuring rotational energies with photoelectron spectroscopy. Depending on the rotational temperature of the anion and the

change in rotational energy between the anion and neutral electronic states, the true origin of vibrationally resolved features can be shifted away from the center of the measured peaks.[9] Therefore, considerable effort is taken to produce cold anions with little rotational and vibrational excitation, which reduces congestion in the measured photoelectron spectrum.

In addition to using photoelectron spectroscopy for spectroscopic investigations of the anion and neutral electronic states, the dissociation dynamics of the anion can be probed with time-resolved photoelectron spectroscopy.[6,7] Figure 1.2 shows a schematic representation of time-resolved photoelectron spectroscopy of AB^-. In these pump-probe experiments, the first photon excites the ground state anion, $\tilde{X}$ AB^-, to a dissociative excited state, $\tilde{A}$ AB^-. The photoexcited anion dissociates according to the $\tilde{A}$ AB^- potential energy curve to yield the photofragments that correspond to the adiabatic channel, A^- and B. The second photon, delayed by some time (Δt), probes the dissociating anion by photodetaching the electron. By measuring the eKE as a function of Δt, the dissociating anion is tracked in real time; therefore, the evolving photoelectron spectra can be interpreted in terms of the evolving electronic wave function as the excited anion dissociates. This technique directly gives the time for charge localization onto the photofragments. Moreover, if the dissociating species undergoes a nonadiabatic transition to a lower energy state and the photofragments are changed, the time-resolved photoelectron spectra will monitor the transition by following the electronic character of the dissociating anion. Time-resolved photoelectron spectroscopy is a very powerful tool for investigating nonadiabatic dissociation dynamics.

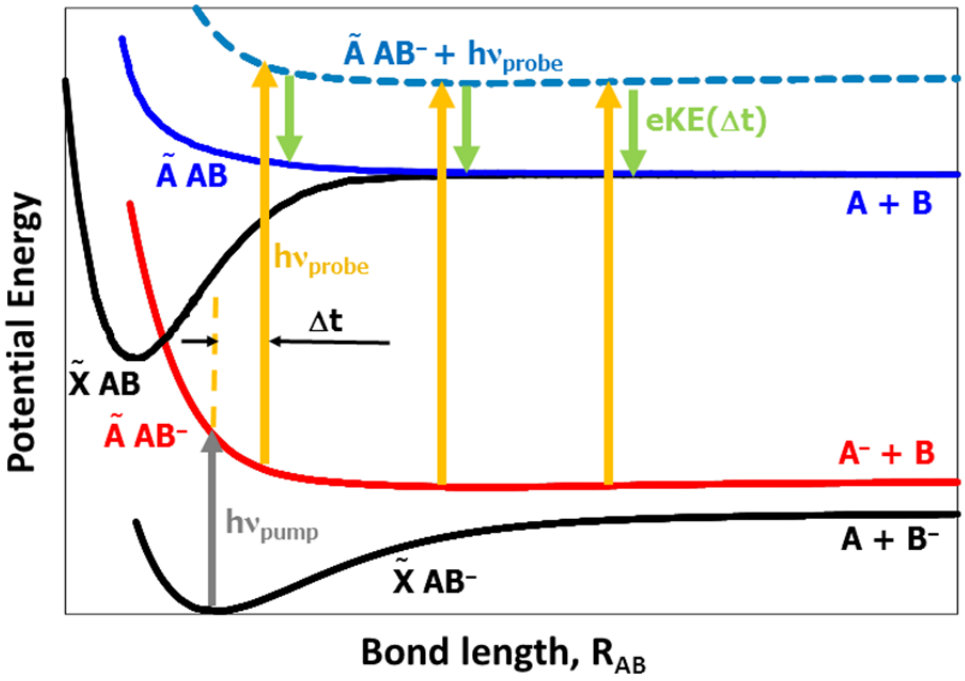

Figure 1.2 Schematic for time-resolved photoelectron spectroscopy of AB^-.

1.3 Collecting the Photoelectron Spectrum of Anions

Experimentally, there are a few common ways to measure the photodetached electrons, which ultimately lead to the photoelectron spectrum. Table 1.1 compares the three most common methods for measuring the energy of photoelectrons: hemispherical analyzer, magnetic bottle, and velocity-map imaging. This table includes the most general values and does not include the many improvements and modifications that could be made to each technique. The readers are referred to additional resources for more details on the hemispherical analyzer[8] and magnetic bottle;[10] the velocity-map imaging is discussed in greater detail in the following chapter.

Table 1.1 Comparison between a typical hemispherical analyzer, magnetic bottle, and velocity-map imaging for detecting photoelectrons

	Hemispherical Analyzer	Magnetic Bottle	Velocity-Map Imaging
Instrument Resolution	~ 8 meV	~ 30 meV	$\Delta KE/KE$[b] ≈ 5%
Collection Efficiency	0.2%	~100%	100%
Pulsed/CW[a] Operation	CW	Pulsed	Pulsed
Photoelectron Angular Distribution	Yes	No	Yes

[a] CW stands for continuous wave
[b] For example, a peak at a kinetic energy (KE) of 1 eV has a full width at half maximum (ΔKE) of 50 meV

Briefly, the hemispherical analyzer, operating in a continuous wave (CW) mode, detects photodetached electrons with a U-shaped analyzer, where only certain electron kinetic energies make it through for a given set of voltages. To allow for the hemispherical analyzer to measure the angular distribution of the photoelectrons, the collection angle is very small, leading to 0.2% collection efficiency of the photoelectrons. The magnetic bottle apparatus is operated in a pulsed mode and the magnetic field within the interaction and detection region is shaped like an inverted bottle. The electrons are photodetached in a strong, inhomogeneous magnetic field (1500 G) that decreases to a smaller magnetic field (2 G) within a few centimeters. The gradient within the field aligns the electrons and directs them through a drift tube where the photoelectrons are temporally separated by kinetic energy prior to impinging upon a detector. Typically, this method loses all information about the angular distribution of the photoelectrons. The velocity-map imaging technique, which is pulsed, focuses the photoelectrons with the same velocity vector (speed and direction) onto the same place on the detector. This focusing is done

with a three-element electrostatic lens followed by a field-free flight region to capture 100% of the photoelectrons.

Each method has its advantages and disadvantages; therefore, the choice of method depends on what is most important for a given experiment. For the experiments presented in this thesis, the velocity-map imaging method is used. With this technique, the photoelectrons are collected as a function of velocity (v), where the instrument resolution is a function of $\Delta v/v$. Therefore, the resolution is not constant over kinetic energy (KE), which leads to the $\Delta KE/KE$ description for instrument resolution. By changing the photodetachment energy, the KE of the ejected photoelectrons can be changed, and the photoelectron spectrum can be shifted in kinetic energy to have different resolutions. The higher collection efficiency leads to shorter collection times. Pulsed versus continuous wave (CW) methods complement different types of anion (or cation or neutral) sources. With velocity-map imaging, the angular distribution and kinetic energy of the photoelectrons are collected simultaneously.

The angular distribution of the photoelectrons is related to the symmetry of the orbital from which the photoelectron originated. The photoelectron angular distribution is defined by the following equation:[11]

$$I(\theta) = (4\pi)^{-1}[1 + \beta P_2(\cos\theta)] \,, \qquad \text{Eqn. 1.4}$$

where θ is the angle between the photoelectron velocity vector and the electric field vector (polarization of the laser light), β is the anisotropy parameter (ranging from -1 to 2, where β = -1, 0, and 2 is a $\sin^2\theta$, isotropic, and $\cos^2\theta$ distribution of photoelectrons, respectively), and $P_2(\cos\theta)$ is the second order Legendre polynomial, $(3\cos^2\theta - 1)/2$. As long as the photoelectron is above

threshold (eKE > 200 meV), the anisotropy value does not vary significantly as a function of eKE. For an atom, it may be possible to define the orbital from which the photoelectron is removed because photodetachment leads to a change of one unit of angular momentum, $\Delta l = \pm 1$. For example, if an electron is removed from an s orbital ($l = 0$), the photoelectron is a p wave ($l = 1$) and $\beta = +2$, where the photoelectron intensity maximum is along the electric field vector, $\theta = 0°$.

The situation is not so simple for molecules because molecules do not have pure s or p (or higher orders of angular momentum) orbitals but a mixture. The β-parameters can still be useful in distinguishing between different electronic states, where each electronic state has a characteristic β value. If the anisotropy difference between the two electronic states is significant, then determining the β-parameters can separate the spectral contribution from two overlapping electronic states. For the experiments presented here, the anisotropy values are not used in our analysis but still remain an important advantage of velocity-map imaging.

1.4 Analyzing the Photoelectron Spectrum of Anions

Regardless of the technique used to collect the photoelectrons, the measured photoelectron spectra can be interpreted by simulating the spectra. However, the "governing forces" involved in photoelectron spectroscopy of anions need to be understood prior to successfully modeling the spectra, such as the overlap between the anion and neutral states, selection rules, and the photodetachment cross section. As is discussed in a previous section, the transitions between the anion and neutral species in photoelectron spectroscopy obey the Born-Oppenheimer approximation, and the nuclei do not move when the electron is photodetached. Therefore, the transition moment, M, is defined as

$$M = \langle \Psi'' | \mu | \Psi' \rangle, \qquad \text{Eqn. 1.5}$$

where the initial and final wave functions are Ψ'' and Ψ', respectively, and μ is the electronic transition moment between the states.[8] The Born-Oppenheimer approximation allows the total wave function (Ψ) to be broken down into independent electronic (ψ_e), vibrational (ψ_v), and rotational (ψ_r) wave functions for both the initial and final states:

$$\Psi = \psi_e \psi_v \psi_r \, . \qquad \text{Eqn. 1.6}$$

After substituting Eqn. 1.6 into Eqn. 1.5, ψ_e and ψ_r can be neglected if it is assumed that μ is constant over different vibrational modes within an electronic state and the rotational overlap integral is constant for all vibrational states, respectively.[8] Therefore, M is proportional only to the overlap between the vibrational wave functions, and the square of this overlap gives the Franck-Condon Factors (FCF) or vibrational overlap intensity:[8]

$$FCF = |\langle \psi_v'' | \psi_v' \rangle|^2 \, . \qquad \text{Eqn. 1.7}$$

For a diatomic molecule, the stretch is the only vibrational mode, and the analysis of the FCF is fairly straightforward. For polyatomic anions, the Franck-Condon analysis becomes more complicated because more than one vibrational mode can be active. If there is a large change in the coordinate that corresponds to a vibrational mode between the anion and neutral species (i.e., large changes in the equilibrium bond angle corresponding to a bending vibration), then there will be an extended Franck-Condon progression for that vibrational mode. Conversely, if there is not a large geometry change along a vibrational coordinate between the anion and neutral species, then the $v'' = 0 \rightarrow v' = 0$ transition will be the strongest with minimal contribution from higher v' states. All symmetric transitions are allowed, which includes

transitions to symmetric normal modes and $\Delta v = 0, \pm2, \pm4, \pm6, \ldots$ transitions between non-totally symmetric normal modes. The intensities for different vibrational progressions are determined by the FCF, which includes the change in equilibrium geometries between the anion and neutral electronic states.

In general, selection rules for photoelectron spectroscopy are much less restrictive than absorption spectroscopy. For example, the only selection rule for electronic transitions in photoelectron spectroscopy of anions is that the anion and neutral species vary by one electron ($\Delta S = \pm1/2$). To a first approximation, the electronic configuration of the neutral species is identical to the anion with the exception of one electron missing. If the anion is a doublet (S = 1/2), then transitions to the singlet (S = 0) or triplet (S = 1) are allowed. However, in absorption spectroscopy $\Delta S \neq 0$ are strongly forbidden transitions, making transitions between singlet and triplet states very weak to nonexistent. For the studies presented in this thesis, all of the lowest energy electronic states of the neutral species are observed; our limitation to detecting other electronic states is not caused by the $\Delta S = \pm1/2$ selection rule but is limited by our laser energy ($E_{photon} < 5.6$ eV).

The photodetachment cross section varies as a function of the kinetic energy of the ejected photoelectron, and this change becomes significant at low eKEs (< 200 meV): Wigner-Threshold Law.[12] In general, the photoelectron has to overcome not only the binding energy of the electron but the long-range attraction, which has different cross sections depending on the angular momentum of the departing electron.[8] The higher the angular momentum is for the departing electron, then the stronger the long-range interaction. For example, the photodetachment cross section for an s-wave electron (ejected from a p orbital) has less

dependence on the kinetic energy, where the cross section scales as $eKE^{1/2}$. A photodetached p electron (ejected from an s or d orbital) has a larger dependence on the kinetic energy, and the photodetachment cross section scales as $eKE^{3/2}$. For molecules, the cross section dependence is not trivial to model. Therefore, we typically do not account for the changing photodetachment cross section when modeling the spectra, but do qualitatively justify spectral features at low eKE using the Wigner-Threshold Law.

The spectra can be simulated by determining the FCF between the anion and neutral species and plotting the FCF as a function of eKE or eBE, where the FCF are convoluted with a lineshape that is representative of the experimental resolution. The PESCAL program written by Kent Ervin does all this in one interactive program, where parameters of the anion and neutral can be changed to best simulate the measured photoelectron spectra.[13] This program calculates the FCF for harmonic oscillators, Morse oscillators, or arbitrary potentials, where all vibrational modes are treated as independent and hot bands can be included. The values that lead to the simulated spectrum are the spectroscopic parameters of the anion and neutral species, such as ω_e, EA, ΔR_e, and T_0. Understanding which vibrational modes are active, which electronic states can be accessed, and how the photodetachment cross section changes become important in interpreting and simulating the measured photoelectron spectra.

1.5 Introduction to Gas-Phase Clusters

Clusters are collections of atoms or molecules that are not covalently bound to each other but weakly interact with each other through electrostatic intermolecular forces.[14,15] Cluster properties are categorized somewhere between the gas phase and condensed phase and are widely applicable. For example, studying cluster formation leads to understanding how particles

are formed in combustion processes and the atmosphere.[14] Moreover, they can also be used to simplify solution-phase processes by removing the bulk (or averaging) aspect of solution phase while still capturing the important dynamics, such as caging, recombination, isomerization, etc., in a more controlled environment.[16] We take advantage of this unique ability of clusters to study anionic clusters in the gas-phase, where size-selected clusters are studied.

There are two types of charged clusters: delocalized (hydrated electrons, ammoniated electrons, etc.) and localized (ionic chromophore with weakly bound solvent molecules (Ar, CO_2, H_2O, etc.)).[15] Of these two types of clusters, this thesis has a focus on the latter, where the influence of the solvent on the anionic chromophore is determined. The spectroscopic properties and dynamics of the ionic chromophore can be shifted or altogether changed depending on the number of solvent molecules, the binding energy of the solvent, and the geometry of the solvent around the ionic chromophore. Studies of anionic clusters give spectroscopic and dynamical information on a microscopic scale that can be transferred and applied to bulk solution, such as electrolytic chemistry.[14,15]

Another advantage of ion solvation with weakly bound solvents is the evaporation of solvent molecules from the clustered anion during the interval between formation and mass analysis to reduce the internal temperature of the ionic chromophore and/or cluster. For example, anions or anionic clusters that are solvated by Ar (binding energy ~50 meV) can only have a small amount of internal energy in order for the solvent to remain bound and not be "boiled off".[17-19] Tagging with weakly bound solvents is a commonly used technique for preparing anions in (or close to) their ground vibrational state.[20,21] More recently H_2 tagging has been used,[22,23] which lowers the internal temperature even more than Ar, but will not be used in

the work presented in this thesis. Before the influence of the solvent can be determined, the bare anionic chromophore must first be understood to see how the solvent affects the chromophore.

1.6 Overview of Thesis

The remainder of the thesis contains the experimental setup, four complete stories (which are part of five published journal articles), and works in progress. The experimental chapter (Chapter II) describes how the photoelectron spectrum is measured. The spectrometer setup, the anion source, mass-selection region, and anion-laser interaction region are described. The chemical systems presented in this thesis require two laser systems: the nanosecond laser system for spectroscopic studies and the femtosecond laser system to study time-resolved dynamics. The photodetached electrons are measured with velocity-map imaging, where the raw images are converted into the photoelectron spectra as a function of energy.

The remaining chapters describe both spectroscopic properties and dynamics of small anions and anionic clusters. In chapter III, the photoelectron spectroscopy of $IBr^-(CO_2)_n$, n = 0 – 3, is discussed.[24] The dissociation dynamics of $IBr^-(CO_2)_n$, n = 0 and 1, are investigated with time-resolved photoelectron spectroscopy in Chapter IV.[25,26] Chapters V and VI contain discussions of photoelectron spectroscopy of ICN^- and $ICN^-(Ar)$ and the dynamics of electronically excited states of bare and solvated ICN^-.[27,28] The final chapter, Chapter VII, describes current projects that are underway, such as HO_3^-. This chapter also includes recent changes to the anion source, which is essential for the formation of HO_3^- and upcoming investigations.

Chapter II: Experimental Methods and Data Analysis

2.1 Overview of Experiment and Data Analysis

The experimental methods used to measure the photoelectron spectra of small anions in the gas phase are described in this chapter. As is typical with physical chemistry experiments, the experimental procedure and analysis change depending on the species being studied and whether or not the experiment is a spectroscopic or dynamics study. This chapter includes the general procedure and analysis for the photoelectron spectroscopy presented in this thesis. However, within each chapter, specific information for that study will be provided.

Overall, the experimental hardware for photoelectron spectroscopy has been previously built and established. The apparatus includes a spectrometer (the ion source, Wiley-McLaren–Time-of-Flight (WM-TOF) mass spectrometer, and photoelectron-velocity–map-imaging (VMI) spectrometer) and laser system, which is illustrated in Fig. 2.1. Following the ion production in a vacuum chamber, the anions are mass separated and focused into the anion-laser interaction region where the anions interact with a pulse of laser radiation to photodetach an electron. The photodetached electrons are measured with the VMI spectrometer to produce an image, which can then be analyzed. For the spectroscopic investigations, the nanosecond laser system is used because energy resolution is necessary; conversely, the dynamics (time-resolved) studies incorporate the femtosecond laser system, which gives good temporal resolution.

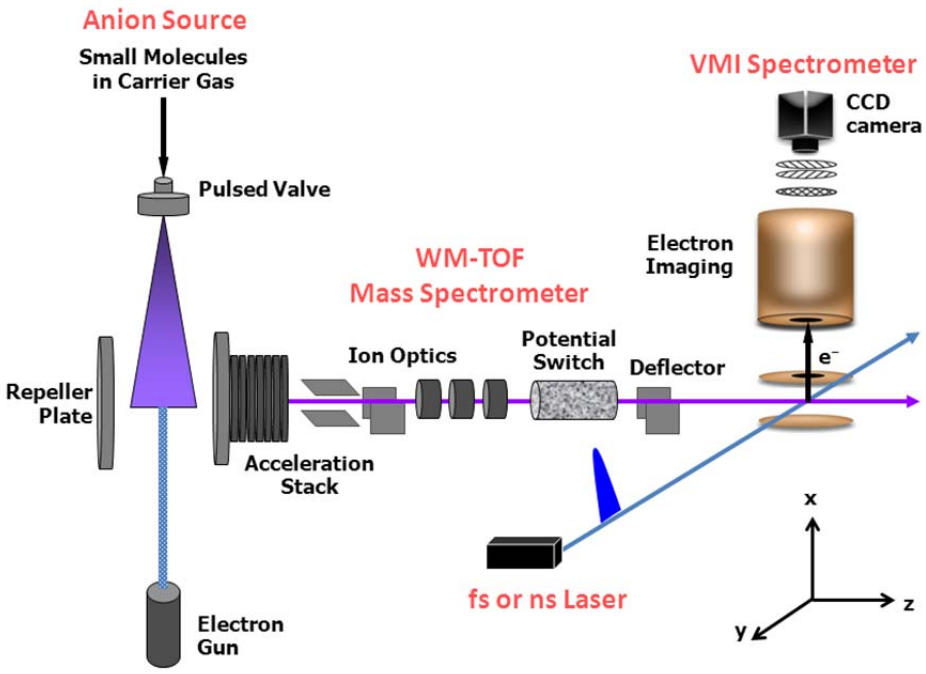

Figure 2.1 Illustration of the anion-photoelectron spectrometer. The anion source generates a plasma containing electrons, neutrals, anions, and cations. The anions are extracted into the WM-TOF, where the anions are separated by their mass-to-charge ratio and focused into the anion-laser interaction region. Here, the anion of choice is overlapped with a pulse of laser radiation, where electrons are photodetached. The ejected electrons are extracted into the VMI setup, and a photoelectron image is measured.

Gathering and analyzing the data really depends on the type of study. The photodetachment images are captured with the DaVis software, where they are converted into the photoelectron spectra using a reconstruction program, BASEX.[29] The number of images that are taken depend on the signal-to-noise for each data set. Low signal can be a result of many things but is mostly attributed to a small density of ions in the anion-laser interaction region and a low photodetachment cross section of the anion. The noise arises from many sources. The largest sources are from the laser radiation photoionizing oil in our vacuum chamber (when the laser

radiation exceeds ~4.1 eV (λ ~ 300 nm)) and from metastable ions in the ion beam autodetaching electrons.

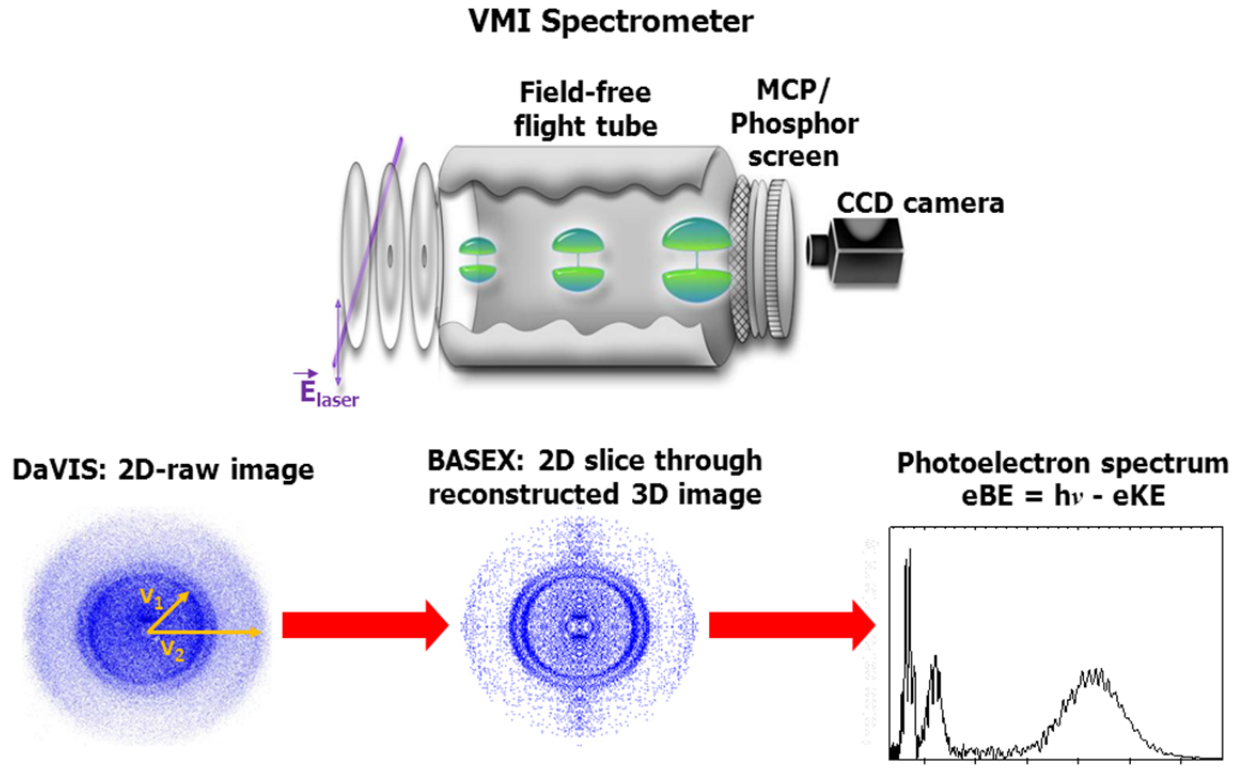

Figure 2.2 Illustration of converting an image to a spectrum. The VMI spectrometer measures the image, and the raw images are compiled with the DaVis software. The 2D-raw images are reconstructed with the BASEX program, which ultimately leads to the photoelectron spectrum.

2.2 Spectrometer Setup

A full description of the spectrometer that includes the anion source, the Wiley-McLaren mass spectrometer, and the photoelectron-velocity–map-imaging (VMI) spectrometer is also available in previous publications.[24,30-34] Two major changes have occurred in the Spectrometer Setup and have not been previously recorded. The first is that the Wiley-McLaren region no longer contains a 1.5° bend in the ion beam path. This was originally in the beam path so that

neutrals would not enter the detection region. However, the 1.5° bend was removed because the neutrals arising from collisional detachment did not pose a major problem and to allow direct optical alignment of the components along the beam path. We also removed a reflectron in the detection region. Before using it again, the structure of the reflectron needs to be reinforced since it is hung horizontally along the ion beam path. Experiments that use the reflectron are not currently being performed on this apparatus, and it has been temporarily removed and stored in the laboratory.

2.2.1 Anion Source

The anion source, as seen in Fig. 2.1 consists of a pulsed valve and electron gun. The pulsed valve is the General Valve, series 9 from Parker Hannifin and is powered by a commercial driver, Iota 1, which is also from Parker Hannifin. The General Valve is a solenoid valve that is made up of an armature, a Kel-F poppet, o-ring, a front spring, a back spring and a faceplate (components bought from Parker Hannifin). The material of the poppet and o-ring can be varied. However, we have found the Kel-F poppet to be the most durable material that is also fairly chemical resistant and the Viton o-ring to be the most affordable and fairly chemical resistant. The faceplate can also be varied, where the size of the orifice and the shape of the orifice cone can be changed. The shape of the cone becomes crucial for changing the expansion characteristics, such as making large clusters, colder beams, collimated beams, etc.[35] After making many alterations, we have found the Parker Hannifin faceplate to be sufficient for our experiments, where we use an 800 μm orifice opening with a 90° cone.

The electron gun is homebuilt and produces ~1000 eV electrons. Within the electron-gun assembly, roughly ~6 A of current flows through a thoriated iridium filament (-1000 V) to

generate thermionic emission of electrons that are radiated in all directions. Because the filament tip is just above the anode knife-edge, the electrons that are generated above this knife-edge are repelled away from the charged (~ -1200 V) electrode and towards the focusing and steering optics. An einzel lens (~ -1000 V) focuses the electron beam at the valve faceplate while the two pairs of deflectors (-100 – +100 V) adjust the vertical and horizontal alignment. To increase the electron density and stability of the electron density at the faceplate orifice, the faceplate has a disc magnet (Magcraft, neodymium-iron-boron, outer diameter 0.75", inner diameter 0.375", thickness 0.125") placed around the orifice.

In these experiments, the carrier gas (CO_2 or Ar, 0 – 60 psig backing pressure) passes over a solid sample of either ICN or IBr, where the vapor pressure of the room temperature sample mixes with the carrier gas. The mixed gas is pulsed into the vacuum chamber through the valve, where molecules are collisionally cooled in the expansion. To prevent condensation of the ICN or IBr, the General Valve is thermoelectrically heated to ~30 – 45 °C. The General Valve can be pulsed at repetition rates up to 100 Hz. For the spectroscopic studies, we pulse the valve at 80 Hz, and for the time-resolved studies, the valve is pulsed at 100 Hz. At these repetition rates, the gas load is fairly large. The entire anion-source region is pumped by a 10" diffusion pump to pressures of ~5×10^{-7} Torr without a gas load and up to ~2×10^{-4} Torr with a gas load (~120 – 250 μs pulse width of General Valve).

Near the orifice of the faceplate, the expanding gas interacts with the collinear beam of electrons from the electron gun to produce a plasma. The plasma contains a plethora of species, such as electrons, anions, cations, neutrals, and clusters. In this region, slow secondary electrons

attach to neutral ICN or IBr, to yield the desired anions. Also, if the gas expansion is cold enough, then molecules condense onto the anion to form clusters of varying sizes.

2.2.2 Wiley-McLaren–Time-of-Flight (WM-TOF) Mass Spectrometer

In the anion-source region, many ions and neutral clusters are made; however, only the anions are extracted into the WM-TOF spectrometer by applying a negative voltage (~ -600 V) to the repeller plate, in Fig. 2.1. The repeller plate is pulsed at the repetition rate of the valve but is delayed from the valve pulse, such that the onset and duration of the repeller-plate pulse maximizes the ion signal in the anion-laser interaction region.

The anions are focused into the anion-laser interaction region with the WM-TOF and additional ion optics. The WM-TOF is a dual stage accelerator that focuses the ion beam along the z coordinate (Fig. 2.1), compensating for the initial spatial spread within the ion packet.[36] The first acceleration occurs between the repeller plate and the first plate in the acceleration stack, which is held at earth ground, to accelerate the anions to ~600 eV. The second acceleration occurs in the stack, which adds an additional ~2300 eV, to give the anions a total of ~2900 eV of kinetic energy. After the ions are accelerated, the anions are guided by two sets of deflectors (variable voltages) and focused along the x and y coordinates by the einzel lens (~+1000 V). In order to avoid floating the detection region at ~2300 V, we use a pulsed potential switch, which abruptly (~20 ns) re-references the ions from 2300 V to earth ground as they pass through the potential switch. Finally there is a last set of horizontal deflectors (-10 – +10 V), which gives a small correction to the ion trajectory prior to the anion-laser interaction region. When the detection region is closed off and the gas is not being pulsed, the WM-TOF region is kept at ~5×10^{-8} Torr by two diffusion pumps (6” and 4”). When the experiment is

running (gate valve to the detection region is open and the gas is being pulsed), the pressure in the WM-TOF region rises to ~$1x10^{-7}$ Torr.

2.2.3 Photoelectron-velocity–map-imaging (VMI) Spectrometer

As can be seen in Fig. 2.1, the anion-laser interaction occurs within the VMI spectrometer to produce a "cloud" of photodetached electrons. The VMI spectrometer consists of a three-element electrostatic lens, a field-free flight region, and a spatially sensitive electron detector.[37-39] Figure 2.2 shows a close-up of the VMI spectrometer. The lens has potentials arranged to give a velocity focusing of the photoelectrons over an extended volume. The three elements are separated by 1", and the second and third elements have a 1" inner diameter hole, as is depicted in Fig. 2.2. The anion-laser interaction region is between the first two elements, where photodetached electrons are ejected in all directions. The electron cloud is repelled through the lens before entering the field-free flight tube, where it continues to expand before striking the detector. The flight tube is 15-cm long, magnetically shielded, and held at the voltage of the third lens element. To maintain a field-free region for the photodetached electrons, the front plate of the detector is also held at the same voltage as the third element in the lens assembly and the flight tube.

The detector is comprised of a dual set of 40-mm imaging-quality microchannel plates in a chevron design (Burle, Inc.), a P47 phosphor screen (Burle, Inc.), and a cooled charge-coupled device (CCD) camera (LaVision) that captures the 2D projection of the 3D-photoelectron velocity distribution. The microchannel plates have ~10^6 gain when they are operated at their maximum, which corresponds to 1100 V across each plate. After exiting the microchannel plates, the electrons are attracted to the phosphor screen, which is held at an additional +3000 V

above the back end of the plates. The fluorescence of the P47 screen (~400 nm) is captured by the CCD camera. To reduce electrical noise within the camera, it is cooled to -11°C. The captured image (1280 x 1024 pixels) is transferred to the computer through a PCI-Interface Board and processed by the DaVis software.

The voltages on the focusing lens (and, therefore, flight tube and detector) are chosen such that the photodetached electrons that have the same velocity (magnitude and direction) impinge onto the detector at the same spot. This is relatively straightforward, if the photodetached electrons originate from a point source. However, the anion-laser interaction region is a finite volume (around 2x2x2 mm) and requires the three-element lensing setup. Discovering this set of conditions is the key feature of the famous VMI spectrometer.[37] For our setup, the voltages on the first and third elements are close to a -1:3 ratio. The voltage on the first element is negative to repel the electrons, and the photodetached electrons are extracted through the other two elements, where the middle element is held at earth ground. Depending on the kinetic energy of the electrons that we want to measure, the voltages are varied. If the electrons of interest have a small kinetic energy, then the voltages are set low to allow the electron cloud to expand and fill the detector; conversely, if we want to measure electrons with a large kinetic energy, then the electron cloud must be extracted with higher voltages so that photoelectron "cloud" does not expand past the size of the detector. To determine the voltages that are applied to the VMI spectrometer elements, we focus the images of known atomic transitions of anions, such as I^- and Br^-, to obtain the narrowest features on the detector.

Within the VMI spectrometer, the first element in the lens and the microchannel plates are individually pulsed. The first element in the electrostatic lens is pulsed on for 300 ns. The

pulsing of the lens produces electrical fluctuations, "ringing", in the spectrometer at early times. Therefore, the first element of the lens is on and stable by the time that the laser interacts with the anion packet and is kept on until the photodetached electrons are through the field-free flight tube. However, the "on time" of the first element prior to the anion-laser interaction is minimized so that the charged element negligibly perturbs the ion-beam trajectories. The microchannel plates are pulsed to minimize background signal. The plates are pulsed on for 5 μs, and the timing of the anion-laser interaction is centered on the pulse. When the microchannel plates are pulsed on, there is ~2000 V difference across the two plates, and when the pulse is absent, there is ~1350 V difference across the plates. In the off mode, the gain across the microchannel plates is drastically reduced and there is minimal noise from background electrons.

The pressure in the detection region is kept low to reduce background photoelectrons from oil. Two turbo pumps (Balzers TPU 240: 230 L/s and Pfeiffer Vacuum HiPace 700: 685 L/s), which are backed by an Alcatel mechanical pump, maintain the detection region at ~3×10^{-9} Torr when gases are not flowing. With a typical gas load, the pressure in the detection region rises to ~5×10^{-9} Torr. To reduce external magnetic fields, the VMI spectrometer is enclosed by four cylindrical layers of μ-metal. The electrostatic lens has an additional μ-metal cup around the focusing lens. Holes are cut into the μ-metal to allow the ion and laser beams to pass through the interaction region.

2.3 Laser Setups

In both the spectroscopic and dynamics investigations, the laser propagation, mass-separated anion beam, and extracted photoelectron directions are mutually perpendicular with the

laser light polarized parallel to the detector plane. The laser radiation is softly focused into the anion-laser interaction region and kept at low power density to minimize two-photon excitation within one laser pulse and space-charge effects; thus the photodetachment volume is roughly 2x2x2 mm. The polarization (horizontal) of the laser light needs to be parallel to the detector face for symmetry reasons that allow the reconstruction of the measured image, which will be discussed in more detail later. If the polarization of the laser beam is vertical and needs to be rotated, then a periscope setup rotates the polarization by having two mirrors positioned such that the axes normal to the mirror surfaces are perpendicular. If the light does not need to be rotated then a periscope is used where the two mirror surfaces are parallel to each other. In either case, the periscope setup is essential for adjusting the laser beams to the correct height of the vacuum-chamber entrance.

2.3.1 Nanosecond Laser Setup

The tunable nanosecond laser system has been described in detail before and only an overview will be given here.[33,34] The nanosecond laser system, Fig. 2.3, is used for the spectroscopic investigations presented in Chapters III and V – VII. We use a commercial Nd:YAG (neodymium-doped yttrium aluminum garnet, Nd:$Y_3Al_5O_{12}$) Coherent Infinity laser. As Coherent discontinued this laser and support of it, Appendix A provides instructions for making new spatial filters and where to order the parts. The spatial filter is an important part of the laser system that "cleans up" the mode quality of the beam.

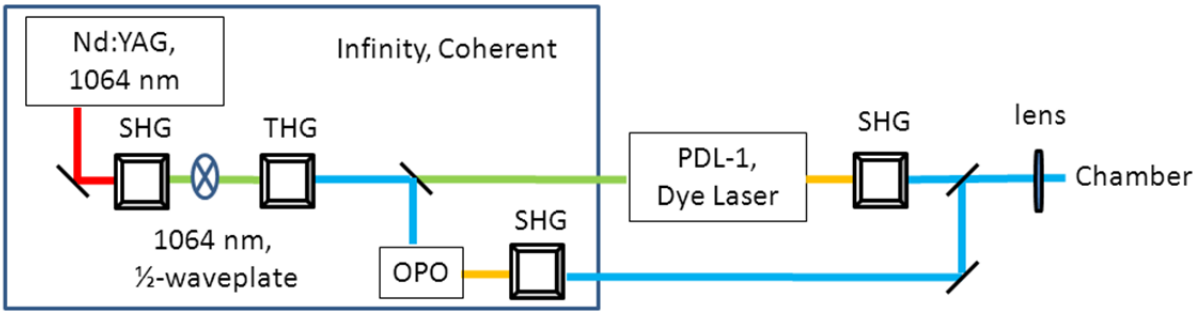

Figure 2.3 Schematic for the nanosecond laser system. Nd:YAG is the abbreviation for neodymium-doped yttrium aluminum garnet, Nd:$Y_3Al_5O_{12}$, laser. SHG, THG, and OPO are acronyms for second harmonic generation, third harmonic generation, and optical parametric oscillator, respectively. PDL-1 stands for pulsed dye laser version 1. Also, the radiation path is color coded to correspond to the energy of the radiation.

The fundamental output of the Infinity is 1064-nm radiation. The laser generates pulses that are ~3-ns wide in time and < 8-cm^{-1} wide in energy. The laser can be pulsed up to 100 Hz; however, all the experiments that use the nanosecond laser system are operated at 80 Hz. The laser is externally triggered by an internally triggered SRS (Stanford Research Systems, model DG535) four channel digital delay/pulse generator, which provides timing for the voltage pulses used by the spectrometer as well. Appendix B shows the SRS settings for the nanosecond experiments.

Within the Infinity housing, there are many component configurations that are utilized depending on the light that is needed. The 1064-nm radiation is doubled with a type I BBO (β-barium borate) crystal (SHG: second harmonic generation) to generate 532-nm light. The 1064- and 532-nm radiation is combined in a THG (third harmonic generation) crystal, which is also type I BBO material, to produce 355-nm light. Because the THG crystal is type I, the 1064- and 532-nm light must have the same polarization; therefore, a λ/2-waveplate is placed in the beam

path between the SHG and THG crystal to rotate the 1064-nm polarization. The 532-nm polarization could be rotated instead, but rotation of the 1064-nm polarization was chosen by Coherent. By detuning the THG crystal, 532-nm light can be directed out of the Infinity housing and used as the photodetachment radiation or to pump the dye laser. The 355 nm-light can also be directed out of the Infinity housing to use in the experiment or pump the optical parametric oscillator (OPO). The OPO consists of a buildup cavity and type I BBO crystal, where signal (410 – 680 nm) and idler (740 – 2200 nm) light is generated. The OPO light is directly used for the experiment or doubled with a Type I BBO crystal inside the Infinity housing. For doubling 410 – 470 nm radiation, we use a Type I BBO crystal that is external to the Infinity housing because the internal SHG housing is too restrictive and does not allow the crystal to be rotated to the necessary angle. This setup allows for great tunability in the UV – IR electromagnetic region except in the wavelength range of 710 nm (and 355 nm) where there is degeneracy in the signal and idler wavelengths of the OPO. The signal and idler light near the degeneracy has an increased bandwidth compared to the rest of the UV – IR region; therefore, we use the dye laser to access this region of the spectrum to obtain a narrower linewidth.

The PDL-1 (pulsed dye laser, version 1) is from Quanta-Ray. The dye laser has a very simple design, as can be seen in Fig. 2.4. This version contains three dye cells: an oscillator, preamplifier, and amplifier dye cell. The PDL-1 can be arranged for the amplifier cell to be side pumped (dotted box) or end pumped. The PDL-1 can also be configured to be pumped with 532- or 355-nm radiation. However, pumping with 532-nm radiation sufficiently covers the near-degeneracy region of the OPO and produces radiation that has a narrow bandwidth (< 8 cm^{-1}). For the experiments reported in this thesis, the ~710-nm radiation is not directly used, but tunable UV light (around 355-nm radiation) is used. Therefore, we employ various mixtures of

DCM, LDS 698, and LDS 722 dyes to produce narrow, tunable radiation that is doubled with an SHG crystal to cover the spectral range between 315 and 370 nm.

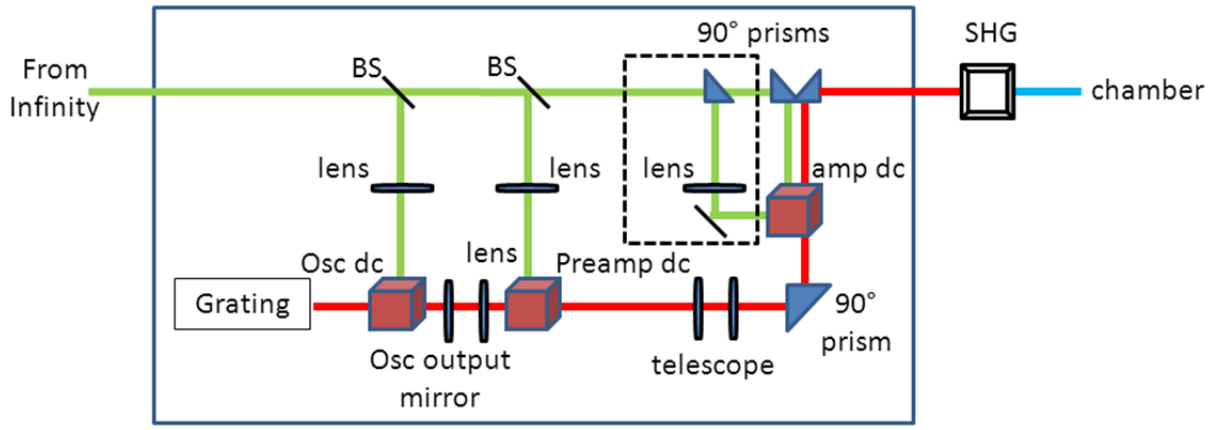

Figure 2.4 Schematic of the tunable dye laser, PDL-1. The PDL-1 is pumped by 532-nm radiation, which is outputted from the Infinity laser. BS, dc, SHG, osc, amp, and preamp are abbreviations for beam splitter, dye cell, second harmonic generation, oscillator, amplifier, and preamplifier, respectively. Also, the radiation path is color coded to correspond with the energy of the light. The dotted box can be used for side-pumping or can be removed to end pump the amplifier dye cell.

2.3.2 Femtosecond Laser Setup

The femtosecond laser system provides short pulses suitable for studies of dynamics that occur on the 200 fs – 100 ps time scale. Figure 2.5 shows a schematic layout of the femtosecond laser system and the respective radiation characteristics for each component. This section provides an overview and a more thorough description of the femtosecond laser system can be found in Todd Sanford's thesis.[33] Unlike the nanosecond studies, the femtosecond laser system must run on its own internal timing and triggers the rest of the experiment by externally triggering the SRS boxes at 100 Hz. In other words, the rest of the experiment is slaved to this master timing. The laser system pulses at 400 Hz, but the General Valve cannot be run at that

high of a repetition rate, so the rate of the valve is reduced to 100 Hz. Appendix C contains the timings and settings for the SRS boxes when a time-resolved experiment is being run.

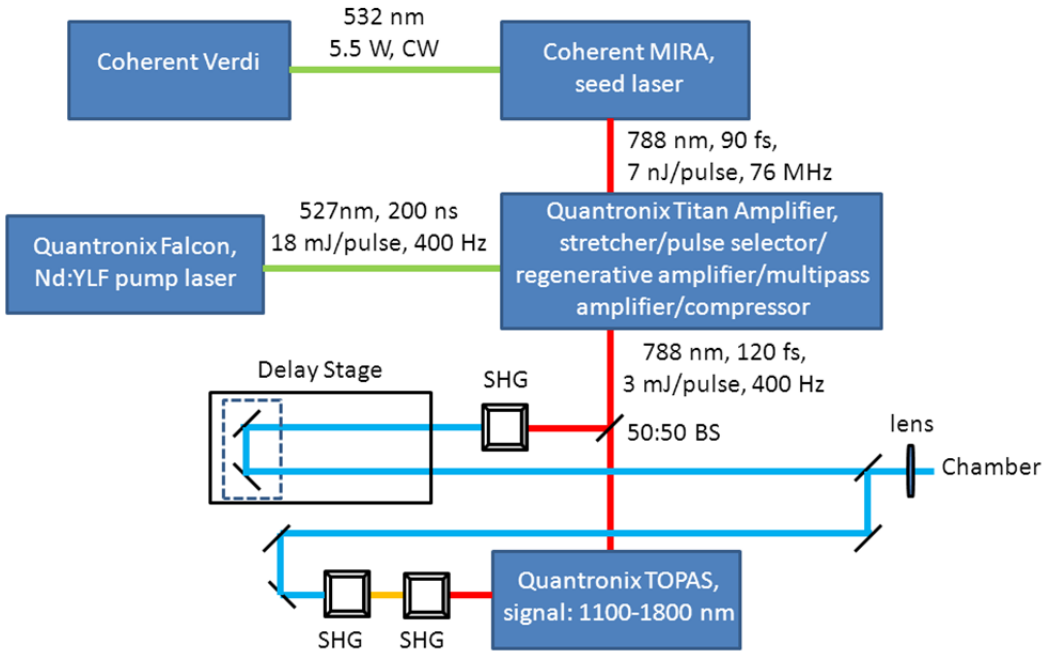

Figure 2.5 Schematic for femtosecond laser system. The SHG, BS, and CW stand for second harmonic generation, beam splitter, and continuous wave. The color coding of the beam path reflects the energy of the light.

The Verdi, which is a diode-pumped Nd:YVO_4 (neodymium-doped yttrium orthovanadate) laser, pumps the MIRA, a mode-locked Ti:sapphire oscillator, to generate the seed pulse. After the MIRA, a photodiode detects the leakage of the seed pulse from the first turning mirror, and this signal is used to trigger the Pockels cell within the Titan. The seed pulse is guided into the Titan, where it is stretched before amplification (~200 ps). The pump light for the Titan comes from the Falcon laser. This Q-switched laser sends the 527-nm pulse, which comes from doubling the fundamental output of a Nd:YLF (neodymium-doped yttrium lithium fluoride) laser, to pump the amplification medium in the Titan. The majority of the pump light is

used to pump the second amplification medium, and the residual light that is transmitted through a reflective mirror is used to pump the first amplification medium.

The amplification stage is a dual process: a regenerative amplifier and a multipass amplifier. The seed pulse passes through a Medox Pockels cell. The Pockels cell serves many purposes. It reduces the repetition rate of the seed pulse from 76 MHz to 400 Hz. It injects a selected seed pulse from the 76-MHz train into the regenerative amplifier at the 400-Hz repetition rate since it is located within the regenerative amplifier cavity. And, it provides the trigger for the Falcon Q-switch and the rest of the experiment (SRS boxes). The regenerative amplification cavity contains a Ti:sapphire crystal, which is pumped by a small amount of the Falcon output at 400 Hz. The seed pulse within the regenerative amplifier makes many round trips before being ejected by the Pockels cell. A photodiode monitors the leakage from an end mirror of the cavity, and the signal is read by an oscilloscope. Therefore, we can watch the buildup and decide the time when the pulse should begin building up and when it should be ejected. The built up pulse then enters a second amplification process: a multipass amplifier. This amplifier also contains a Ti:sapphire crystal, which is pumped by the majority of the Falcon output at 400 Hz. The seed pulse makes two passes through the amplification medium and then enters a grating compressor, which reduces the width of the pulses to ~120 fs. To compress the pulses of the Titan output, we adjust two gratings within the compression region to minimize the pulse width by using an autocorrelator (INRAD, model 5-14BX).

The 788-nm compressed pulse then exits the Titan and must be separated into the appropriate legs for the pump-probe experiments, which is done with a 50:50 beam splitter. For these experiments, the pump pulse is either the 788-nm light (1.5 mJ) or the doubled light from

the Titan, 394 nm (0.5 mJ). The doubled light is generated by passing the 788-nm light through a Type I BBO crystal. The pump pulse is put onto a computerized Parker delay stage (~1.3 fs per step), which is controlled by a LabView program, to adjust the pump-probe delay time (Δt). The pump light is then steered towards the chamber and recombines with the probe pulse prior to entering the chamber. For these experiments, the probe pulse must be UV radiation (~310 nm) that we generate by pumping the TOPAS (Light Conversion Ltd. by Quantronix) with the other half of the 788-nm light. The TOPAS contains a Type II BBO crystal, which requires three passes of the 788-nm radiation through the crystal. The first pass creates a continuum generation, which seeds the second pass. The second pass is the preamplifier pass, and the second pass outputs the fundamental, signal, and idler radiation. For the third pass, the signal radiation seeds the amplification medium while the 788-nm radiation pumps it, which outputs the fundamental, signal, and idler radiation. In order to generate the desired UV light (30 – 40 μJ), the signal of the TOPAS is quadrupled by two consecutive type I BBO crystals. The UV light is then directed towards the chamber, where it recombines with the pump pulse.

The recombined pump and probe pulses must be overlapped in space at a known Δt. To calibrate Δt, the temporal overlap ($\Delta t = 0$) at the anion-laser interaction region is determined by finding $\Delta t = 0$ outside the vacuum chamber, where a piece of glass identical to the vacuum chamber window is used. After the pump and probe pulses pass through the piece of glass, they combine in a Type I BBO crystal and pass onto a grating, which separates the different energies of the light. The delay stage is adjusted to generate UV light, which comes from sum frequency generation (SFG) of the pump and probe pulse. The SFG light is a clear signal of temporal overlap of the pump and probe pulses and is detected with a photodiode, which transfers the signal to a LabView program. The signal is mapped out to produce a Gaussian shape, and the

center of the Gaussian corresponds to $\Delta t = 0$. The cross-correlation of the two pulses gives a full width of half maximum of ~300 fs.

2.4 Data Analysis

Figure 2.2 shows an overview of how a photoelectron spectrum is generated from the raw VMI spectrometer image that is obtained by the CCD camera, which is also described in previous theses.[33,34] The raw image is directly related to the velocity distribution of the photoelectrons and is transferred from the CCD camera to the computer, where the raw images are handled by the DaVis software. Within the DaVis software, the raw images are summed, subtracted, and/or averaged. Since these raw images are 2D projections of the initial 3D photoelectron distributions, they need to be reconstructed into the original 3D distributions to yield the photoelectron spectra. The BASEX software does this reconstruction to give a spectrum as a function of pixel, which is directly related to speed. The spectra are then converted from speed space to energy space. Analyzing the spectra could be done in most data analysis programs and Igor is used for all of the data analysis presented in this thesis. Also, we choose to make the background corrections in Igor rather than in the DaVis software because of over-subtraction issues which will be discussed later.

2.4.1 DaVis

The DaVis software is interfaced with the CCD camera and controls the exposure time per image. The exposure time can range from 1 ms to 1×10^6 ms (16.67 min). There are two modes of camera operation: conventional (analog) or event counting (digital) mode. The event counting mode gives better experimental resolution and requires a longer time for data collection; however, this mode cannot handle a significant background of photoelectrons. Both

collection modes are described but the majority of the spectra that are shown in this thesis do not benefit from higher resolution or have too large of a background that event counting is no longer an effective collection mode; therefore, all of the spectra are taken with the conventional mode unless otherwise specified.

For the conventional mode, the number of counts per pixel per image is directly collected by the DaVis software. At long exposure times, the intensity per pixel can become saturated; at short exposure times, the collection process is no longer efficient because of the processing time per image and the amount of noise that is introduced. Therefore, we select an exposure time that is well below the saturation limit (~3000 counts can saturate a pixel). Setting the exposure time depends on the system being studied. For example, systems that require high-energy photons ($E_{photon} > 4.1$ eV) produce many background electrons from ionization of oil molecules, and the exposure time must be limited to avoid saturation. However, the DaVis software is equipped with a program (Sequencing/Summing) that will internally sum or average the images. Shorter exposure times can be consecutively taken and averaged internally; this saves time because it is not necessary to save and average the individual images. The conventional mode leads to a FWHM/KE (full width at half maximum/kinetic energy) of ~5%.

For better experimental resolution (FWHM/KE ~ 3 – 4%), the data can be obtained in the event counting mode. DaVis has a macro (Andre) that replaces a spot on the image, which is a few pixels by a few pixels, with a pixel in the middle of the spot with intensity “1” and the remainder of the pixels for that spot are assigned “0”. A threshold can be set in the macro which discriminates between signal and background spots, assigning the center of a spot with high enough intensity as “1” while all other spots are assigned “0”. The exposure time for the camera

should be set low so that two counts do not appear at the same place on the detector. This would lead to undercounting events because the event would only be assigned an intensity of "1" and not "2". Typically, the signal images are taken in event counting mode and the background images are taken in the conventional mode discussed earlier. Event counting is more time consuming; therefore, the macro is only used if the measurement is close to the experimental resolution and event counting would improve the resolution of the measured features. Also, if the photon energy is high ($E_{photon} > 4.1$ eV), it can become very difficult to acquire the data in the event counting mode because the counts are too high per exposure.

In either mode, it is often best to alternate between signal and background images. For a spectroscopic study, usually only the signal (anion and laser pulses overlapped in time) and background (anion and laser pulses mismatched in time) images need to be taken. The time-resolved studies require more background correction because both the pump and probe pulses can generate one-photon signal in addition to background electrons. Therefore, the background subtraction is more complicated and must be evaluated for each time-resolved study. Alternating between signal and background images accounts for long-term drifting in the ion signal and/or laser power. Typically every one to five minutes, we alternate between signal and background images. At the end of a data set, the signal images are averaged into one image and the same occurs with the background images. If we are smart in naming the individual image files, the Batch Processing program within the DaVis software will average all the files for us. By naming the signal (background) images as 'signalX' ('backgroundX'), where X = 1, 2, 3…, we can set the Batch Processing program to average as many of the 'signal' ('background') images as desired, as long as the file name is the same and the name is terminated by a number. If the background counts are low compared to the signal counts, then less averaging has to be

done for the background images compared to the signal images. Conversely, if the background counts are comparable to or larger than the signal counts, then both images must be averaged the same amount of time.

In order to perform the reconstruction of the image, the center of the image must be determined. BASEX has a built-in program that finds the center, but we have found this to give the wrong centers due to noisy images, an asymmetric gain profile across the detector, and the edge of the detector appearing in the image. To date, the most accurate way is manually choosing the center. In the DaVis software, we can place a circle on the image and center it. If the signal image has a strong background, then we will subtract the background image from the signal image prior to finding the center of the image. However, both the signal and background images are individually reconstructed by the BASEX program with the appropriate center.

2.4.2 BASEX Reconstruction

The measured image is the projection of the 3D photoelectron cloud collapsing onto the 2D detector, which is shown as the image on the bottom left of Fig. 2.2. Electrons that have a higher speed (v_2 in Fig. 2.2) move further away from the center then slower electrons (v_1 in Fig. 2.2). If the polarization of the laser radiation is parallel to the detector face, then the ejected electrons have a cylindrical symmetry about the polarization axis; the VMI spectrometer in Fig. 2.2 shows a pictorial representation of this cylindrical symmetry. There are many approaches for reconstructing the original 3D images.[39] If there is an axis of cylindrical symmetry, which photoelectron spectroscopy inherently has, the inverse Abel transform is typically used. One of the most common techniques for calculating the inverse Abel transform is the Fourier-Hankel technique;[40] however, this method does a point by point reconstruction and does not adequately

handle noisy images or sharp features.[29,39] Another technique for calculating the inverse Abel transform is BASEX (BAsis Set EXpansion), which fits the entire spectrum at once and is able to more effectively handle residual noise.[29,39] Due to the type of data that we collect, the BASEX software is used for all of the data presented in this thesis.

The BASEX software expands the 2D projection in a basis set of functions that are well-behaved, Gaussian-like functions.[29] The linear combination of these functions reconstructs the 3D image, where the coefficients are the same as those for the projected image. The center slice through the reconstructed 3D image is shown in Fig. 2.2. The intensity of the reconstructed 3D image is integrated over all angles for all values of v to obtain the photoelectron intensity as a function of the electrons' speed. As long as the symmetry of the photodetached electrons follows that depicted in Fig. 2.2, then the BASEX software can also generate the β values, related to the angular distribution of the photodetached electrons, as a function of the electrons' speed. For the studies presented in this thesis, the β values were always considered but did not play a part in the analysis because the measured β values were either too noisy or did not clearly differentiate between neutral electronic states to give useful conclusions.

2.4.3 Photoelectron Spectrum

The spectra generated from the BASEX software have the photoelectron intensity plotted as a function of pixel, which is directly related to the speed of the electrons. However, it is not common to plot the photoelectron spectra as a function of speed but rather as a function of energy. The kinetic energy, *KE*, is related to the speed, *v*, by

$$KE = \frac{1}{2}mv^2 \,, \qquad \text{Eqn. 2.1}$$

where *m* is the mass of the electron. The photoelectron intensity in speed and energy space are related by

$$I_{KE} = I_v \left(d\left(\frac{1}{2}mv^2\right)\right)/dv \,, \qquad \text{Eqn. 2.2}$$

where *I* is the photoelectron intensity in energy (I_{KE}) or speed (I_v) space. Upon solving and simplifying Eqn. 2.2, we obtain the Jacobian correction for the photoelectron intensity:

$$I_{KE} = I_v/mv \,, \qquad \text{Eqn. 2.3}$$

where the mass is constant making I_{KE} proportional to I_v/v. Therefore, the photoelectron intensity is divided by the pixel (which is directly related to *v*) to obtain the photoelectron spectra as a function of the electron kinetic energy, eKE. The eKE scale is calibrated with an atomic image, where the electron binding energy (eBE) and therefore eKE are known. The spectra are converted from *eKE* to *eBE*,

$$eBE = hv - eKE, \qquad \text{Eqn. 2.4}$$

making the spectra independent of the photon energy used. Most of the spectra will be reported as a function of eBE, except for Chapter VI where the spectra are plotted as a function of eKE.

The subtraction of the signal from the background is performed in Igor (or another data analysis program) and not within the DaVis software. The main reason to avoid subtraction within the DaVis software is that an over subtraction gives negative signal, and the BASEX program processes this negative signal as "zero". For the atomic calibration images, where the signal is significantly large compared to the background, then the subtraction is most efficient in the DaVis software; however, for all other situations it is best to do the subtraction in a data

analysis program. Another benefit to doing the subtraction after the reconstruction is that the background subtraction is not always one-to-one. This is especially true when there is a large background of electrons from photoionization of oil.

2.5 Conclusion

The experimental setup and data analysis must be adjusted slightly for each chemical system that we study, and the specifics for each chemical system are discussed in their respective chapters. The general layout for the spectrometer and laser systems is discussed, where the spectroscopic investigations use the nanosecond laser systems (Chapters III and V – VII) and the time-resolved studies use the femtosecond laser system (Chapter IV). The anions are generated and then mass separated in a WM-TOF spectrometer. The anions of interest and the laser pulse interact in the VMI spectrometer to photodetach electrons. The VMI spectrometer collects the projected-2D image, and the DaVis software processes the raw image. The raw image is reconstructed using the BASEX software to generate the photoelectron spectrum as a function of electron speed. This spectrum is then converted from speed to energy space to generate the photoelectron spectrum as a function of energy.

Chapter III: Photoelectron Spectroscopy of $IBr^-(CO_2)_n$, n = 0 – 3

3.1 Motivation

Many important processes occur in solution, such as solvation of electrolytes and acid-base chemistry.[14,41] However, these systems can be difficult to study on a microscopic scale because of the complexity introduced by the solvent. For example, is the solvent merely acting as a heat bath for a reaction, or is it itself a participant in the reaction? From a theoretical standpoint, it is also not trivial to model a process in the condensed phase. It is preferable for the modeled system to have a controlled number of components. If the system of interest is smaller, then theoretical calculations and modeling become a much more manageable feat.

One approach to simplify condensed phase processes is to study them in the gas phase. The number of solute and solvent molecules is drastically reduced to yield gas-phase clusters, which contain one solute molecule and varying number of solvent molecules.[15,42] For neutral clusters in the gas phase, this simplification still proves difficult because it is not trivial to separate the cluster sizes. However, in a charged cluster (anion or cation) in the gas phase, the cluster sizes can be separated by mass-to-charge in a time-of-flight experiment. In this setup, the effects of sequential solvation to the charged solute are studied, such as the binding strength of the solvent to the solute and the amount of perturbation that the solvent introduces to the solute. For example, if the solvent interacts strongly, then the electronic character of the solute will be greatly disrupted. Furthermore, the properties of smaller clusters are easier to calculate with quantum methods. For both theory and experiment, studying clusters is a good approach to understand the fundamental processes that occur in the condensed phase.

The solvation of IBr^- with CO_2 has been previously studied by our group.[25,30,43,44] These studies have shown that CO_2 solvation greatly affects the dissociation dynamics of IBr^-, and $IBr^-(CO_2)_n$ clusters may be a good model for studying solvation. Thompson *et al.* has performed calculations on IBr^-, where the dissociation energy (0.948 eV), vibrational frequency (118 cm^{-1}), and equilibrium bond (I–Br) length (3.05 Å) of the ground state of the anion as well as the electron affinity (2.494 eV) of IBr have been calculated.[43,45] In addition to these calculations on the bare anion, the calculations on the $IBr^-(CO_2)_n$ clusters reveal that the minimum energy configuration places the first three CO_2 molecules around the waist of the I–Br, and the CO_2 molecules are weakly bound to the anion, ~200 meV. The IBr–CO_2 binding energy has been estimated from photodissociation studies from our group and is consistent with calculations.[30,43,44] However, the spectroscopy of the anion ground state has not been studied, and the photodissociation experiments only give an average CO_2 binding energy. Photoelectron spectroscopy is one technique that could further confirm the theoretical values.

By studying the photoelectron spectroscopy of the anion cluster, we have all of the advantages of mass selection and can learn about both the anion and neutral cluster. Photoelectron spectroscopy of $IBr^-(CO_2)_n$ clusters measures the transitions between the anion and neutral molecules at the equilibrium geometry of the anion ground state. The geometry change between the ground states of the anion and neutral IBr are expected to be significant. Assuming that the CO_2 minimally perturbs the solute, the ground states of the anion and neutral $IBr(CO_2)_n$ clusters differ by a σ^* electron, which is strongly antibonding. This large geometry change between the ground states agrees with the current literature values, where the calculated anion bond length ($R_{I–Br}$ = 3.05 Å) is longer than the experimentally determined bond length for neutral IBr ($R_{I–Br}$ = 2.47 Å).[43,45-47] Therefore, we will rely on transitions to the first two excited

states of IBr ($R_{I-Br} \approx 2.85$ Å) to analyze the photoelectron spectrum of IBr^- because the excited states of IBr will have better $\upsilon'' = 0 \rightarrow \upsilon' = 0$ overlap with the ground vibrational state of IBr^-.

Patchkovskii has calculated the 23 lowest energy electronic states of IBr.[48] The three lowest energy states are bound: the ground electronic state ($\tilde{X}\,^1\Sigma^+$) and the first two excited states ($^3\Pi_2$ and $^3\Pi_1$). There is negligible Franck-Condon overlap between the $^1\Sigma^+$ ($\upsilon = 0$) and the $^3\Pi_2$ and $^3\Pi_1$ ($\upsilon = 0$) states due to the I–Br bond lengthening of the $^3\Pi$ states. Therefore, experimentalists used techniques other than ground-state absorption spectroscopy to investigate the first two excited states of IBr, such as observing emission from ion-pair states to the $^3\Pi$ states, absorption of the $^3\Pi$ states to higher lying states, high-resolution spectroscopy of the $\tilde{X}\,^1\Sigma^+$ to $^3\Pi_1$ state (where the $\upsilon'' = 0 \rightarrow \upsilon' = 6 - 29$ was probed).[46,49-52] These studies yield many of the $^3\Pi$ spectroscopic parameters of IBr, which will be used for interpretation of the IBr^- photoelectron spectrum.

We present the photoelectron spectrum of IBr^-, which contains transitions to the ground state ($\tilde{X}\,^1\Sigma^+$) and the first two excited states ($^3\Pi_2$ and $^3\Pi_1$) of IBr. There is a large equilibrium (I–Br) bond length change between the anion ground state and neutral ground state, which precludes the direct observation of the $\upsilon'' = 0 \rightarrow \upsilon' = 0$ transition. However, the vibrational resolution in the excited states leads to a much more accurate value for the EA(IBr), where a spread exists in the current EA values, 1.6 – 2.7 eV.[47,53,54] In addition, many spectroscopic parameters of the anion are determined by fitting the transitions of the $^3\Pi$ states in the photoelectron spectrum, such as the equilibrium bond length (R_e), the vibrational frequency (ω_e), and the anharmonicity ($\omega_e x_e$) of IBr^-. Using a thermochemical cycle, we determine the dissociation energy (D_0) of the anion ground state. In addition to the photoelectron spectra of

IBr^-, the $IBr^-(CO_2)_n$, n = 1 – 3, spectra are measured. The CO_2 solvation minimally perturbs the electronic character of the IBr^-, which is concluded from the consistent shift in the spectral features as n increases. However, the CO_2 congests the photoelectron spectrum, which arises from the additional degrees of freedom introduced by the solvent. From the solvated spectra, we conclude the EA of $IBr^-(CO_2)_n$, n = 1 – 3.

3.2 Experimental Methods

Most of the experimental methods and corresponding references can be found in Chapter II. A thorough description of the anion source, Wiley-McLaren–Time-of-Flight (WM-TOF) mass spectrometer, and photoelectron spectrometer is provided in section 2.2. The data analysis is detailed in section 2.4. Finally, section 2.3.1 presents the nanosecond laser system used in these studies. The remainder of this section includes details specific to this study that are not already addressed in Chapter II.[24]

We generate $IBr^-(CO_2)_n$, n = 0 – 3, by flowing 20 psig of CO_2 gas (99.8%, Scott Specialty Gases, Inc.) over a solid sample of IBr (98%, Sigma Aldrich). The gas expands into the source chamber through a heated (~45 °C), pulsed General Valve nozzle (0.8-mm orifice, series 9, Parker Hannifin) at 80 Hz. The 1-kV beam of electrons interacts with the gas pulse to produce secondary electrons. These electrons attach to the IBr to yield IBr^-, and CO_2 molecules collide and eventually bind to the cooled IBr^-. The anions are then extracted into the WM-TOF mass spectrometer, which spatially focuses the mass-selected $IBr^-(CO_2)_n$, n = 0 – 3, into the anion-laser interaction region. Most of the images are taken in the conventional (long exposure) camera operation mode. The images that measure transitions to the $^3\Pi$ states are taken in the event counting mode, which is described in section 2.4.1. This experimental setup produces

essentially a 50:50 distribution of $I^{79}Br^-$:$I^{81}Br^-$ in both the bare and clustered anions, which is expected from the natural abundance of bromine. All the data in this chapter were taken with $I^{79}Br^-(CO_2)_n$, n = 0 – 3, but we expect identical data with the ^{81}Br isotope.

In the anion-laser interaction region, the photodetachment radiation, 260 – 300 nm, arises from doubling the OPO signal, which is pumped by the third harmonic of a pulsed Nd:YAG laser. We use nanosecond laser pulses that have energies between 50 and 150 μJ/pulse to interact with the mass-selected anion, where the laser light is softly focused into the anion-laser interaction region. The photoelectron spectrometer is calibrated and focused with the photodetachment spectra of I^- and Br^-, where the EA and spin orbit splitting are well known for both neutral species, I and Br.[2,55] The production of I^- and Br^- anions coincides with the production of $IBr^-(CO_2)_n$, n = 0 – 3.

3.3 Photoelectron Spectroscopy of IBr^-

3.3.1 Results

Because IBr^- has a similar electronic configuration to that of I_2^-, the IBr^- and I_2^- photoelectron spectra should be similar.[17,56] The valence electronic configuration for ground state dihalides ($\tilde{X}\,^2\Sigma^+$) is $\sigma^2\pi^4\pi^{*4}\sigma^{*1}$, where the highest energy electron resides in a strongly antibonding orbital. The removal of this σ* electron yields the ground state dihalogen ($\tilde{X}\,^1\Sigma^+$) with a much shorter bond. With this large change in bond length, the greatest Franck-Condon overlap should be between the anion $^2\Sigma^+$ ground vibrational state, $\upsilon'' = 0$, and the vibrationally excited ground state IBr ($\tilde{X}\,^1\Sigma^+$), υ' = high. Thus, one anticipates negligible Franck-Condon intensity from the $\upsilon'' = 0 \rightarrow \upsilon' = 0$ transition.

The removal of the second highest energy electron from the π* orbital generates the excited $^3\Pi$ states. The geometry change between the anion ground state and the bound $^3\Pi$ states is less drastic since the π* orbital has less antibonding character than the σ* orbital. Consequently, one would expect better overlap between the anion $^2\Sigma^+$ ground vibrational state, $\upsilon'' = 0$, and the neutral $^3\Pi$ ground vibrational states, $\upsilon' = 0$. The inset of Fig. 3.1 shows the bond shortening of the neutral states relative to the anion ground state. Thompson *et al.* calculate the ground electronic state of IBr^-, and Patchkovskii calculates the potential energy curves for the neutral electronic states of IBr.[43,48] These potential energy curves of IBr and IBr^- along with the vertical arrow highlight the parts of the neutral electronic states that will be accessed by photoelectron spectroscopy of IBr^-. To a first approximation, transitions to the ground state ($\tilde{X}\ ^1\Sigma^+$) should yield a broad feature, while transitions to the $^3\Pi$ states should result in narrower features in the spectrum similar to the spectrum of I_2^-.[17,56]

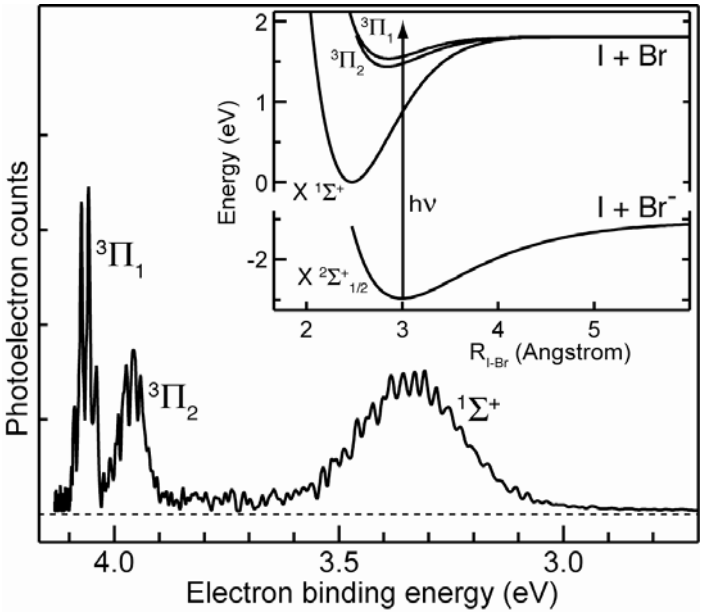

Figure 3.1 Photoelectron Spectrum of IBr^- ($\lambda = 300$ nm). The broad peak at 3.35 eV corresponds to high-lying vibrational levels of the ground electronic state, $\tilde{X}\ ^1\Sigma^+$. The ground-state origin is not observed and lies ~1 eV lower in binding energy. The next two sharp features are the first two excited states of IBr ($^3\Pi_2$ and $^3\Pi_1$). The inset shows the calculated potential energy curves of the anion ($\tilde{X}\ ^2\Sigma^+$) ground electronic state as well as the ground electronic state ($\tilde{X}\ ^1\Sigma^+$) and the first two excited electronic states of neutral IBr ($^3\Pi_2$ and $^3\Pi_1$).

The photoelectron spectrum ($\lambda = 300$ nm) of IBr^-, shown in Fig. 3.1, matches our expectations. The spectrum is plotted as a function of electron binding energy. There are three features in the spectrum. As expected, the broad, low-energy feature results from transitions to the ground state of IBr, and the sharper features at higher energy correspond to transitions to the first two excited states of IBr, $^3\Pi_2$ and $^3\Pi_1$. The broad peak at a vertical detachment energy (VDE) of 3.35 eV does not contain the $\upsilon'' = 0 \rightarrow \upsilon' = 0$ transition but, instead, is ~ 250 meV wide with some structure near the VDE. The two higher energy features at VDEs = 3.95 and 4.05 eV, which are transitions to the $^3\Pi_2$ and $^3\Pi_1$ states, respectively, have good vibrational resolution.

3.3.2 Discussion

Even though IBr has attracted considerable attention, there still remains some ambiguity in the EA of IBr.[47,53,54] The analyzed photoelectron spectrum of IBr^- yields a much more accurate value for the EA(IBr). In addition, the analysis determines the dissociation energy (D_0), vibrational frequency (ω_e), and anharmonicity ($\omega_e x_e$) of the anion as well as the change in geometry between the anion and neutral (ΔR_e). From the spectrum, the ground state feature appears to have some structure near the VDE. Analysis of the structure, however, would not be definitive since we are accessing very high-lying vibrational states of the ground electronic state. The VDE of the ground-state feature corresponds to ~ 30 quanta in the I–Br stretch, which is determined from the known vibrational frequency and anharmonicity of IBr.[46,50,52,57,58] Since an accurate identification of the individual vibrational states cannot be determined, we do not discuss the ground-state structure further.

Instead, the first two excited states of IBr are used to determine the spectroscopic constants because these states have prominent peaks owing to good vibrational resolution and we directly measure the $\upsilon'' = 0 \rightarrow \upsilon' = 0$ transitions. Figure 3.2 shows the vibrational progressions of the two excited electronic states, where the black trace is the experimental data. Transitions to the $^3\Pi_2$ state have spectral peaks that are spaced by 18 meV, which is consistent with the literature value for the $^3\Pi_2$ I–Br stretch frequency (18.30 meV).[49,51] Similarly, the vibrational spacing measured for transitions to the $^3\Pi_1$ state is 17 meV, matching nicely with the previously published values for the $^3\Pi_1$ state (16.7 meV).[46,50,52] In Fig. 3.2, the label 1_0^0 identifies the origin transition for each electronic state. (The number "1" denotes the vibrational normal mode, which for a diatomic molecule is uniquely the stretching mode. The superscript is the vibrational

quantum number of the neutral [υ'], and the subscript is the vibrational quantum number of the anion [υ'']). The spacing between the known energies of the ground vibrational states of the $^3\Pi_2$ and $^3\Pi_1$ states, 115 meV, concurs with the spacing between the two peaks marked with 1_0^0.[46,49,50,52] Also, the peaks that reside lower in binding energy than the $^3\Pi_2$ origin peak have a different spacing. As seen in the inset of Fig. 3.2, the dashed, blue trace results from a progression of Gaussian peaks spaced by 16.6 meV. This inset focuses on transitions to the $^3\Pi_2$ state that are from hot bands of the anion, $\upsilon'' = 1$, 2, or 3 → $\upsilon' = 0$; the spacing of the hot band features agrees with the calculated vibrational frequency of the anion, 118 cm^{-1}.[45]

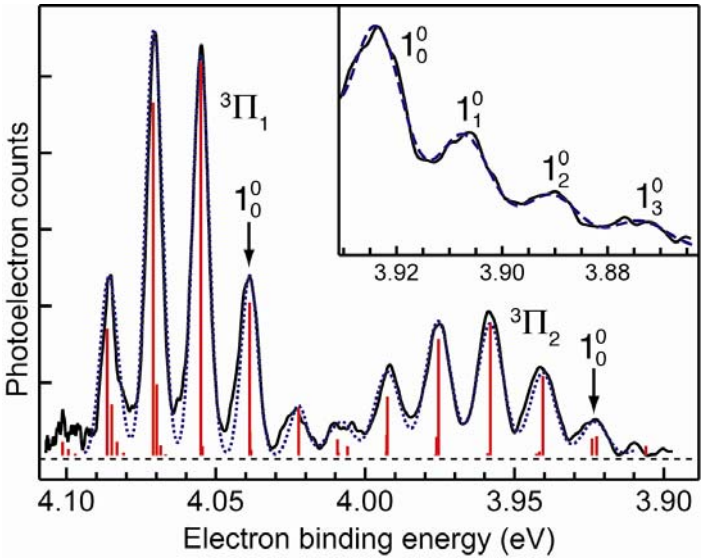

Figure 3.2 Photoelectron Spectrum of IBr^- showing transitions to the $^3\Pi_2$ and $^3\Pi_1$ states. The solid, black trace is the experimental data. The dotted, blue trace is the Franck-Condon simulation, and the red sticks are the corresponding Franck-Condon intensity for each transition. The origin bands of the $^3\Pi_2$ and $^3\Pi_1$ states are designated with 1_0^0. The inset contains the photoelectron spectrum showing hot bands, which are transitions from excited vibrational states of IBr^-. The solid, black trace is the experimental data, and the dashed, blue line is a fit with Gaussian peaks spaced by 16.6 meV.

To extract further data, we simulate the spectrum in Fig 3.2 using the PESCAL program.[13,59] The simulation uses Morse potentials for the ground state of the anion and the first two excited states of IBr.[43,48] Although the excited states do not fit perfectly to a Morse potential, it is sufficient for these simulations. Less is known about the anion ground state. However, there is a minimal geometry change between the anion and excited states; therefore, use of a Morse potential is reasonable. The spectroscopic constants for the neutral excited states are held constant at known literature values,[46,49,50,52] along with the ω_e and $\omega_e x_e$ values for the anion ground state. (The ω_e is determined from the fit to the data in the inset of Fig. 3.2, and the $\omega_e x_e$ for the anion will be discussed later in this section). The anion temperature, the bond length change between the anion ground state and IBr excited states, the origin position of the IBr excited states relative to the anion ground state, and the origin intensities are all varied to fit the experimental data. The anion temperature (T_{vib}) and geometry change (ΔR_e) establish the shape of the Franck-Condon envelopes; the origin position and intensity determine the position and intensity of the spectral envelopes. In Fig. 3.2, the Franck-Condon simulation is shown as a dotted, blue trace, and the Franck-Condon intensities for the various transitions are shown as red sticks.

The outputs of the simulation yield the vibrational temperature and the R_e(I–Br) value for the anion ground state as well as the EA(IBr). The simulation yields a $T_{vib} \sim 150$ K for the anion. The simulated ΔR_e for each spectral band leads to the anion equilibrium bond length (3.01 ± 0.01 Å) since the R_e(I–Br) values for the IBr $^3\Pi_2$ (2.841 ± 0.002 Å) and $^3\Pi_1$ (2.858 ± 0.001 Å) states are already known.[49,51,52] The difference between the two simulated ΔR_e values for the $^3\Pi_2$ and $^3\Pi_1$ bands, which is the simulated difference in the equilibrium I–Br bond lengths for the two excited states of IBr, is slightly different than the literature value,

0.017 ± 0.003 Å.[13,15,16] The small discrepancy most likely comes from the changing photodetachment cross section. The photodetachment cross section changes as a function of the electron kinetic energy, where the change is most significant near the laser-detachment threshold (at low kinetic energy).[60] It is not trivial to correct for the change in cross section in molecules. As mentioned earlier in the section, the bond length change determines the envelope shape. Therefore, the changing photodetachment cross section will affect the $^3\Pi_1$ envelope more than the $^3\Pi_2$ envelope, thus leading to the slight inconsistency in the simulated bond length change between the two excited states.

The EA determination is not as straightforward as the R_e determination for IBr^- since the rotational states are populated in the anion; the PESCAL simulation does not account for the rotational contribution to the experimental lineshapes. In general, a difference in rotational constants, B_e, between the initial and final states results in an asymmetric rotational contour that shifts the true vibronic band origin away from the lineshape maximum (VDE). The known B_e'' for the $^3\Pi_2$ and $^3\Pi_1$ states is 0.0424 ± 0.0005 cm^{-1} and 0.0429 ±0.0001 cm^{-1}, respectively.[46,49-52] However, the B_e' for the anion ground state is not known but is estimated to be 0.03825 ± 0.0003 cm^{-1} based on the anion R_e in the ground electronic state. Using an approximate formula for band shifts and a rotational temperature of 100 K, we determine that the rotational contour shifts the origin position by 8 ± 5 cm^{-1} lower in energy than the VDE.[9] Looking back to the simulation in Fig 3.2, seven of the spectral peaks are "clean" (consisting of a single vibrational transition) with two of these being the $^3\Pi_2$ and $^3\Pi_1$ origin peaks, where the origin positions determined from the simulation are 3.9225 and 4.0388 eV, respectively. These peaks are suitable for the determination of the EA(IBr), using the peak centers and the estimated

rotational shift of the peak maxima. We determine the EA(IBr) = 2.512 ± 0.003 eV, where the uncertainty comes from the energy calibration of the spectrum, fit to the spectrum, calculated rotational shift, and the previously determined term energies. As expected, the EA(IBr) is similar to other dihalogens: EA(I_2) = 2.524 eV and EA(Br_2) = 2.4 – 2.6 eV.[47,54,56,61-63] Table 3.1 contains a summary of the spectroscopic constants for IBr and IBr^-.

Table 3.1 Spectroscopic constants for IBr ($\tilde{X}\ ^1\Sigma^+$, $^3\Pi_2$, and $^3\Pi_1$) and IBr^- ($\tilde{X}\ ^2\Sigma^+$).

	T_0(eV)[d]	ω_e(cm^{-1})	$\omega_e x_e$(cm^{-1})	D_0(eV)	R_e(Å)
IBr ($^3\Pi_1$)[a]	1.5253(1)	135(2)	1.8(9)	0.2922(5)	2.858(1)
IBr ($^3\Pi_2$)[b]	1.4105(5)	147.631(1)	1.261(4)	0.407(1)	2.841(2)
IBr ($\tilde{X}\ ^1\Sigma^+$)	0	268.68(1)	0.81(1)	1.8181(1)	2.469
IBr^- ($\tilde{X}\ ^2\Sigma^+$)[c]	-2.512(3)[e]	134(10)	0.55	0.966(3)	3.01(1)

[a] Averaged spectroscopic constants for $^3\Pi_1$ taken from previous publications[46,50,52]
[b] Averaged spectroscopic constants for $^3\Pi_2$ taken from previous publications[49,51]
[c] Averaged spectroscopic constants for $^2\Sigma^+$ taken from previous publications[46,47,64]
[d] T_0 is the energy of the $\upsilon = 0$ level in each electronic state relative to the $\upsilon = 0$ of IBr($\tilde{X}\ ^1\Sigma^+$)
[e] Alternatively, EA(IBr) = 2.512 ± 0.003 eV

Finally, a thermochemical cycle is used to determine the dissociation energy for the anion ground state:

$$D_0(\tilde{X}^2\Sigma^+\ I–Br^-) = D_0(\tilde{X}^1\Sigma^+\ I–Br) + EA(IBr) – EA(Br). \qquad \text{Eqn. 3.1}$$

The $D_0(\tilde{X}\ ^1\Sigma^+$ I–Br) = 1.8181 eV and the EA(Br) = 3.3636 eV are known from literature values.[2,64] The EA(IBr) = 2.512 eV is determined from our simulation of the IBr^- photoelectron spectrum, previously discussed. This thermochemical cycle gives a $D_0(\tilde{X}\ ^2\Sigma^+$ I–Br^-) value of

0.966 ± 0.003 eV, which is close to the value calculated by Parson and coworkers (0.948 eV) and smaller than previous estimates.[30,43,47] Considering the zero-point energy (which is approximately half of the anion vibrational frequency, 67 ± 5 cm^{-1}), the $D_e(\tilde{X}\,^2\Sigma^+$ I–Br) equals 0.974 ± 0.0003 eV. The simulation in Fig 3.2 uses Morse potentials where the ω_e is held at 134 cm^{-1}, $\omega_e x_e$ is fixed at 0.55 cm^{-1}, and T_{vib} = 150 K. The anion vibrational temperature is low enough that the $\omega_e x_e$ value does not significantly affect the simulation. Therefore, we further confirm the anharmonicity by calculating the $\omega_e x_e$ using a Morse potential with a well depth of 0.974 eV, which results in a value consistent with the 0.55 cm^{-1} used in the simulation.

3.4 Photoelectron Spectroscopy of $IBr^-(CO_2)n$, n = 1 – 3

The bare IBr^- spectrum (taken with photodetachment radiation of λ = 300 nm) has three easily identifiable regions that originate from transitions to the three lowest energy electronic states of IBr. The bare anion spectrum (black trace) is compared to the photoelectron spectra of solvated IBr^-, $IBr^-(CO_2)_n$ (n = 1 – 3), in Fig. 3.3. The spectrum for $IBr^-(CO_2)$ is taken at λ = 285 nm (blue trace), the $IBr^-(CO_2)_2$ spectrum is taken at λ = 272 nm (green trace), and the $IBr^-(CO_2)_3$ spectrum is taken at λ = 260 nm (red trace). As more CO_2 molecules are added, the spectral features shift to higher binding energy. The spectra become more congested, but overall, the character of the spectra is preserved. The assignment of the spectral features follows from the bare anion spectrum. There are spectrally broad transitions to the ground electronic state of the clusters, $IBr(CO_2)_n$ ($\tilde{X}\,^1\Sigma^+$), which reside lower in binding energy, and transitions to the higher energy $^3\Pi$ states, which result in sharper features.

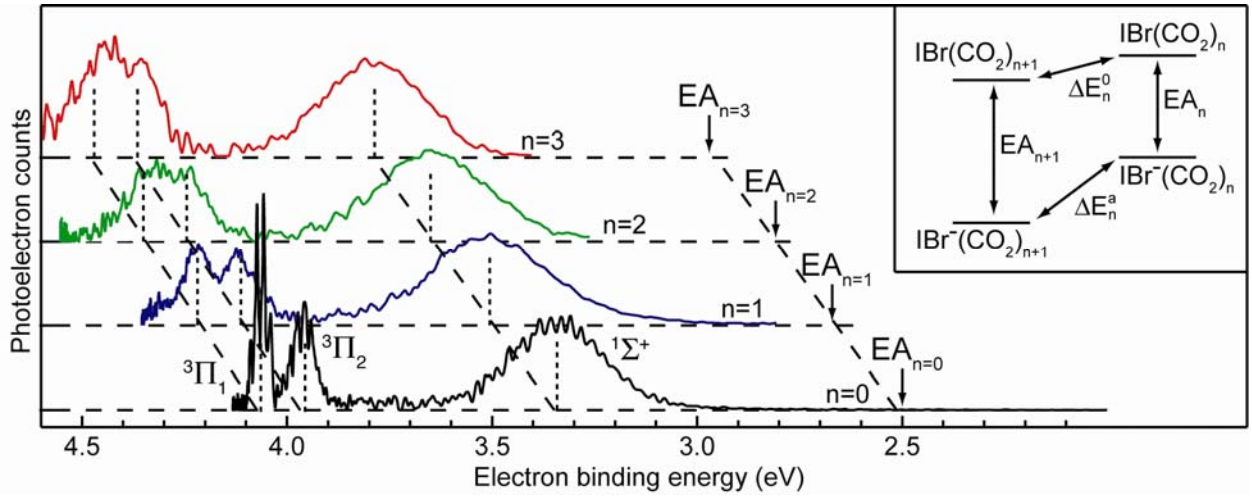

Figure 3.3 The photoelectron spectra of $IBr^-(CO_2)_n$, n = 0 – 3. The ground state and first two excited states are shown for IBr (black trace), $IBr^-(CO_2)$ (blue trace), $IBr^-(CO_2)_2$ (green trace), and $IBr^-(CO_2)_3$ (red trace). The electron affinity, EA, is not directly observed but identified for each spectrum. The vertical, dashed lines are the VDEs for each peak from a fit using three Gaussian lineshapes. The inset contains the energy diagram for the clusters, showing the relationship between cluster electron affinities and the solvent binding energies of the neutral and anion clusters.

The shift to higher binding energies is expected with solvation and leads to an EA estimate for the solvated $IBr(CO_2)_n$ clusters. The measured spectral shift is the difference in CO_2 binding energy between the anion and neutral species. As the inset to Fig. 3.3 shows, the shift is to higher binding energy because the anion (ΔE_n^a) has a stronger solvent binding energy than the neutral (ΔE_n^0). The IBr^-–CO_2 solvation is dominated by a charge-quadrupole interaction; whereas, the IBr–CO_2 solvation is dominated by a dipole moment-quadrupole interaction. Once the shift in binding energy is understood, the EA can be estimated for the solvated species, using the cycle illustrated in the inset of Fig 3.3:

$$EA_{n+1} = EA_n + \Delta E_n^a - \Delta E_n^0. \qquad \text{Eqn. 3.2}$$

For example, when n = 0, EA_{n+1} is the EA of $IBr(CO_2)$, EA_n is the EA of IBr, and $\Delta E_n^a - \Delta E_n^0$ is the measured shift in the spectral features. Before the EAs can be determined for $IBr(CO_2)_n$, the spectral shift must be quantified, $\Delta E_n^a - \Delta E_n^0$; however, this is not a straightforward task since the spectral features become congested and blurred upon solvation.

To quantify the spectral shifts, we fit each spectrum to a sum of three Gaussians. For $IBr^-(CO_2)_n$ n = 0 and 1, this is fairly straightforward because all three spectral bands are well separated. The situation becomes more complicated for n = 2 and 3; however, we use the analogy to n = 0 and 1 to fit the n = 2 and 3 spectra. In the n = 0 and 1 spectra, the spacing between the peak centers (or VDEs) of the $^3\Pi$ states is similar (105 meV on average), and therefore, we constrain the separation between the $^3\Pi_2$ and $^3\Pi_1$ peak centers to 105 meV in the n = 2 and 3 spectra. Also, the $^3\Pi_2$ and $^3\Pi_1$ states have approximately the same width in the n = 0 (width of 60 meV) or 1 (width of 90 meV) spectra; therefore, the width of the $^3\Pi_2$ and $^3\Pi_1$ peaks are kept the same for the n = 2 (width of 120 meV) and 3 (width of 150 meV) spectra. With these constraints the n = 2 and 3 spectra are fit to a sum of three Gaussians. Table 3.2 contains the VDEs and peak shifts for the bare and solvated spectra. The first CO_2 molecule shifts the peaks by ~155 meV. If we estimate that the binding energy of $IBr–CO_2$ is ~50 – 100 meV ($I–CO_2$ binding energy is 45 meV and $I_2–CO_2$ binding energy is 95 meV), then we arrive at the $IBr^-–CO_2$ binding energy being ~205 – 255 meV, which is consistent with previous calculations by Thompson *et al.*[43,45,65,66]

Table 3.2 Fits to the photoelectron spectra of $IBr^-(CO_2)_n$, n = 0 – 3 and electron affinities (EA) for $IBr^-(CO_2)_n$, n = 0 – 3.

		Parent anion			
Neutral electronic state		IBr^-	$IBr^-(CO_2)$	$IBr^-(CO_2)_2$	$IBr^-(CO_2)_3$
$^3\Pi_1$	VDE (eV)	4.063	4.219	4.348	4.468
	peak shift (eV)[a]		0.156	0.129	0.120
$^3\Pi_2$	VDE (eV)	3.960	4.109	4.243	4.363
	peak shift (eV)[a]		0.149	0.134	0.120
$\tilde{X}\ ^1\Sigma^+$	VDE (eV)	3.341	3.504	3.646	3.786
	peak shift (eV)[a]		0.163	0.142	0.140
	EA (eV)	2.512(3)	2.67(3)	2.80(6)	2.93(9)

[a] peak shifts are VDE differences between consecutive cluster anions, $VDE_{n+1} - VDE_n$

The EAs for $IBr(CO_2)_n$, n = 0 – 3, are included in Table 3.2, where the EAs for n = 1 – 3 are determined from Eqn. 3.2. As was discussed earlier, Eqn. 3.2 includes the $\Delta E_n^a - \Delta E_n^0$ term, which is related to the peak shifts in the spectrum. Within each solvated spectrum, the spectral bands are energetically shifted about the same amount relative to the bare IBr^- spectral features; this consistent shift strongly suggests that the transitions under each peak do not change with solvation, i.e., the origin transitions are contained in the $^3\Pi$ envelopes for all values of n. Therefore, the peak shifts (Table 3.2) equal the $\Delta E_n^a - \Delta E_n^0$ term. Since the spectral peaks become wider with increasing values of n, the uncertainty of the origin position within the peaks increases. Therefore, the uncertainties in the EAs for n = 1 – 3 are directly related to the increasing full width at half maximum (FWHM) of the $^3\Pi$ bands as n increases, where the FWHM is 60, 90, 120, and 150 meV for n = 0, 1, 2, and 3, respectively.

The relatively constant shift in the spectral features indicates that the CO_2 solvent molecules are minimally perturbing the electronic chromophore of IBr^- and IBr. However, the photoelectron spectra become more congested as n increases. For n = 1, transitions to the $^3\Pi$ states become blurred and the vibrational progressions are no longer observed; following the addition of the second CO_2 molecule, transitions to the two excited states can no longer be separated into two bands. The CO_2 molecule adds additional degrees of freedom and, therefore, congestion to the measured photoelectron spectra. Similarly, in a high-resolution photoelectron spectrum (zero electron kinetic energy, ZEKE, spectroscopy) of $I^-(CO_2)$, Neumark and coworkers found that vibrational motion along the I–CO_2 coordinate led to overtones and hot bands spaced by 30 and 60 cm^{-1}, respectively. They also identified the CO_2 low frequency bend, 667 cm^{-1}, in their spectrum.[67-69] We would also expect to have similar contributions from the CO_2 in the $IBr^-(CO_2)_n$ spectra, except the IBr–CO_2 stretching modes should be lower in frequency due to the heavier mass of IBr^-. Finally, the rotational contours will be broader because of the asymmetry brought about by the CO_2 geometry, which will further congest the spectra. Therefore, it is not surprising that the additional degrees of freedom introduced by the CO_2 congest the spectra even though it is minimally perturbing the electronic chromophore of IBr^- and IBr.

3.5 Conclusion

The photoelectron spectrum of IBr^- directly accesses the ground electronic state ($^1\Sigma^+$) and first two excited states ($^3\Pi_2$ and $^3\Pi_1$) of IBr. The two bands corresponding to transitions to the $^3\Pi_2$ and $^3\Pi_1$ states contain vibrational progressions and are fit to yield spectroscopic parameters of the anion and neutral IBr. The fit provides an accurate determination of the EA = 2.512(3) eV

of neutral IBr as well as the $R_e(I–Br^-) = 3.01(1)$ Å, the $\omega_e = 134(10)$ cm^{-1}, and the $\omega_e x_e =$ 0.55 cm^{-1} of the anion ground state. Using a thermochemical cycle, the dissociation energy of the anion is determined to be $D_0 = 0.966(3)$ eV. There is good agreement between these experimental values and the calculated values by Thompson *et al*. which gives confidence to the theoretical approach for these larger dihalide systems.

The photoelectron spectra of $IBr^-(CO_2)_n$, n = 1 – 3, retain similar spectral features as the bare IBr^- spectrum, but they become more congested with each additional CO_2 molecule. The congestion is due to the additional degrees of freedom introduced by the CO_2 solvent. The spectral features are systematically shifted as n increases, which strongly suggest that the CO_2 is minimally perturbing the electronic chromophore of the anion and neutral IBr. The spectral shift is directly related to determining the EA of the $IBr(CO_2)_n$ clusters. The photoelectron spectra of the sequential solvation will be important for interpreting the time-resolved studies of IBr^- and $IBr^-(CO_2)$, which will be the focus of the next chapter.

Chapter IV: Watching Charge Transfer within $IBr^-(CO_2)$

4.1 Motivation for time-resolved experiments

To a first approximation, electronic and nuclear motions are separable, and the electrons respond "instantaneously" to any change in the nuclear coordinates. This is known as the Born-Oppenheimer (B-O) approximation and is the basis for the adiabatic potential energy surfaces of molecules. These molecular adiabatic surfaces are often used to estimate pathways for photodissociation processes. However, not all processes follow the B-O approximation, such as relaxation of electronically excited molecules, charge-transfer reactions, and chemiluminescence.[70-72] The B-O approximation often breaks down when both the kinetic energy of the nuclear coordinates is significant and the evolving system is near a conical intersection or in a region where two different electronic states are close in energy.[70] Understanding the breakdown of the B-O approximation is important in many processes. Two examples are photoinduced DNA damage, where nonadiabatic transitions protect photoexcited DNA, and the photoisomerization of rhodopsin, which is responsible for vision.[73-75] These processes, and many others, take place in the condensed phase; thus, it is also important to understand how, if at all, the solution phase is promoting the nonadiabatic process.

As is discussed in the previous chapter and Chapter I, the dynamics in condensed phase are difficult to study on a microscopic level because the measured dynamics are usually averaged over the entire solution. Clusters in the gas phase, therefore, provide an avenue to isolate the solvation effects and study them on a microscopic level. Ionic clusters have an additional advantage in that they can be separated by mass-to -charge in a time-of-flight apparatus, and the

effect of consecutive addition of solvent molecules can be determined. By mass selecting different cluster sizes, the effect of the local environment around the ionic chromophore can be determined. In bulk solution, the local environment around a chromophore can be different than the bulk characteristics; therefore, it is important to know how the local environment responds to changes in the chromophore.[76,77]

Our group and the Parson group have a long, collaborative history of studying dihalide cluster anions,[16,78-82] and in particular $IBr^-(CO_2)_n$, n = 0 – 14.[30,43-45,83] The collaborative effort has focused on the photodissociation dynamics of these clusters, where the dynamics vary (geminate recombination, caging, solvated photoproducts, and charge transfer) depending on the cluster size. These $IBr^-(CO_2)_n$ cluster studies reveal that large cluster sizes are not necessary to change the dissociation dynamics; instead, one CO_2 molecule is sufficient to alter the photodissociation dynamics of IBr^-.[30,43,45] More specifically, photoexcited IBr^- anions can undergo nonadiabatic processes when solvated by a single CO_2 molecule.

The bare IBr^- anion has at least two absorption bands in the visible/near infrared region that correspond to the two low-lying electronic states ($A'\ ^2\Pi_{1/2}$ and $B\ ^2\Sigma^+$ states), which are optically allowed transitions from the ground electronic state of IBr^- ($\tilde{X}\ ^2\Sigma^+$).[33,43,45] Figure 4.1 shows the calculated potential energy curves for the six lowest energy electronic states of IBr^-; the calculation is discussed later in the text. The molecular orbital-based description of the electronic configuration of the ground state of IBr^- is $\sigma^2\pi^4\pi^{*4}\sigma^{*1}$. Excitation of the bare IBr^- $\tilde{X}\ ^2\Sigma^+$ anion to the $A'\ ^2\Pi_{1/2}$ state involves a π to σ^* transition and leads to a single photodissociation channel:[30,33]

$$IBr^-\ (\tilde{X}\ ^2\Sigma^+) + h\nu\ (E_{photon} = 1.57\ eV) \rightarrow IBr^-\ (A'\ ^2\Pi_{1/2}) \rightarrow I^- + Br \quad 100\%. \qquad \text{Eqn. 4.1}$$

Excitation to the second bright state, the B state, is a stronger transition ($\sigma \rightarrow \sigma^*$) and also leads to a single photodissociation channel:[30,33]

IBr^- $(^2\Sigma^+) + h\nu$ (E_{photon} = 3.14 eV) $\rightarrow IBr^-$ ($B\ ^2\Sigma^+$) $\rightarrow I^* + Br^-$ 100%. Eqn. 4.2

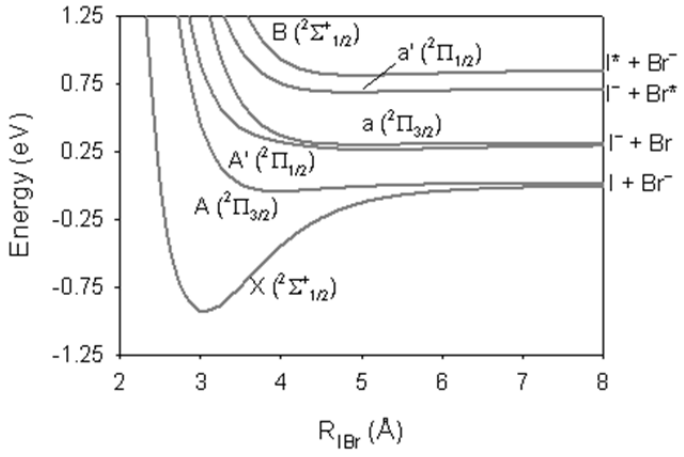

Figure 4.1 Calculated potential energy curves of IBr^-. The six lowest electronic states of IBr^- are plotted as a function of the I–Br bond length.

Yet, previous photofragment analysis studies of $IBr^-(CO_2)_n$ show that one CO_2 solvent molecule can profoundly influence the dissociation dynamics, resulting in the appearance of charge-transferred photoproducts. Although these studies lacked time resolution, they unambiguously show that the photodissociating $IBr^-(CO_2)$ cluster undergoes nonadiabatic transitions to one or more nearby electronic state(s) with charge transfer character:[33]

$IBr^-(CO_2)$ ($\tilde{X}\,^2\Sigma^+$) + hν (E_{photon} = 1.57 eV) → $IBr^-(CO_2)$ ($A'\,^2\Pi_{1/2}$)

→ $I^- + CO_2 + Br$ 36.3%, Eqn. 4.3a

→ $I^-(CO_2) + Br$ 60.5%, Eqn. 4.3b

→ $I + CO_2 + Br^-$ 3.2%, Eqn. 4.3c

where Eqn. 4.3c is the nonadiabatic transition to the $A\,^2\Pi_{3/2}$ or $\tilde{X}\,^2\Sigma^+$ electronic states, and

$IBr^-(CO_2)$ ($\tilde{X}\,^2\Sigma^+$) + hν (E_{photon} = 3.14 eV) → $IBr^-(CO_2)$ ($B\,^2\Sigma^+$)

→ $I^* + Br^- + CO_2$ 67.5%, Eqn. 4.4a

→ $I^- + Br^* + CO_2$ 32.5%, Eqn. 4.4b

where the nonadiabatic transition is from the $B\,^2\Sigma^+$ to the $a'\,^2\Pi_{1/2}$ in Eqn. 4.4b. In the B-state photodissociation studies of $IBr^-(CO_2)$ (Eqn. 4.4), the CO_2 solvent molecule does not solvate the photoproducts as it does in the A′-state photodissociation studies (Eqn. 4.3). The kinetic energy release following photoexcitation to the B state is 1.2 eV, which is four times greater than the A′-state studies. The much larger kinetic energy release in the B state converts into dissociation along the solvent-binding (I^-–CO_2 or Br^-–CO_2) coordinate.

Sanov and coworkers studied the photodissociation of IBr^- after excitation to the A′ state and also found that IBr^- cleanly dissociates to I^- + Br using time-resolved photoelectron spectroscopy (TRPES).[84] This technique involves a pump-probe experimental scheme, where the first (pump) laser pulse promotes the anion to an excited state and a time-delayed (Δt) probe laser pulse photodetaches the electron. By measuring the photoelectron spectrum at various

delay times, the evolution of the electronic character is followed in real time. With 300 fs experimental resolution, they find at early times (0 – 200 fs) that the photodetachment signal spreads out over a few hundred meV. During the first picosecond (ps), the signal narrows and shifts until it reaches its final spectral position, which corresponds to the I^- reference peak. After 1 ps, the photodetachment signal does not change in width or position, which suggests that the I^- fragment is no longer influenced by the Br counterpart.

The calculated TRPES results, performed by McCoy and coworkers, are in good agreement with the experimental TRPES.[85] In these calculations, the IBr^- is treated quantum mechanically, where the ground-state wave function of IBr^- is promoted and propagated on the A′ electronic state prior to photodetaching the electron. It is notable that the experimental results are successfully reproduced by a calculation that does not account for possible changes in the photodetachment cross section; because of this, the authors conclude that the photodetachment cross section is constant during the photodissociation of IBr^- following excitation to the A′ state.

In the remainder of this chapter, the solvent-mediated charge transfer dynamics are studied by TRPES, building upon the experiments of Sanov and coworkers. For the A′-state photodissociation studies, the $IBr^-(CO_2)$ evolving wave function is probed as the charge transfers from I to Br, and the time for charge transfer is determined (Eqn. 4.3). We also investigate the B-state photodissociation studies with TRPES. In these B-state studies, the adiabatic products correspond to $I^* + Br^-$ (Eqn. 4.2), which is characterized with TRPES. Again, one CO_2 molecule is sufficient to influence the dissociation dynamics on the B state, and $IBr^-(CO_2)$ dissociates to both $I^* + Br^- + CO_2$ (Eqn. 4.4a) and $I^- + Br^* + CO_2$ (Eqn. 4.4b). The TRPES of $IBr^-(CO_2)$ following excitation to the B state captures this charge hop from the B $^2\Sigma^+$ state to the

lower energy a′ $^2\Pi_{1/2}$ electronic state. High-level quantum mechanical calculations and molecular dynamics (MD) simulations assist in the interpretation of all the TRPES data and the mechanism for solvent-mediated charge transfer.

4.2 Experimental

A full description of the experimental apparatus, including the appropriate references, is detailed in Chapter II, specifically, the femtosecond (fs) laser setup in section 2.3.2. The production of the $I^{79}Br^-$ and $I^{79}Br^-(CO_2)$ is identical to the procedure outlined in Chapter III. This chapter involves two femtosecond laser setups for the A′- and B-electronic state photodissociation studies. The A′-state studies require a pump wavelength of 788 nm (1.5 mJ) and a probe wavelength of 313 nm (30 – 40 μJ). The 788-nm radiation is the fundamental output of the fs laser system and is divided into the pump and probe leg with a 50:50 beam splitter. For the probe leg, the 788-nm light pumps an optical parametric amplifier (OPA), and the OPA signal output is quadrupled to produce the 313-nm probe light. For the B-state studies, the pump light (394 nm, 500 μJ) is generated by doubling the fundamental radiation. The probe light is produced by quadrupling the OPA signal output to obtain tunable UV radiation, 30 – 40 μJ, (for IBr^- 313-nm radiation is used and for $IBr^-(CO_2)$ 305-nm radiation is used).

For each spectrum that is taken at a delay time, Δt, the background must be subtracted. The background consists of one-photon signals that come from pump or probe light alone. For example, Fig. 4.2 shows the transient signal for the $IBr^-(CO_2)$ A′-state studies at Δt = 50 ps (blue trace). This time-resolved signal is a result of the pump-only and probe-only spectra (both black traces) subtracted from the pump-probe spectrum (pulses delayed from each other by Δt = 50 ps, red trace). The same background subtraction scheme is used for all time delays, and we combine

all of the resulting transient spectra into a 3D contour plot to display the data. The same approach is taken with the B-state photodissociation studies.

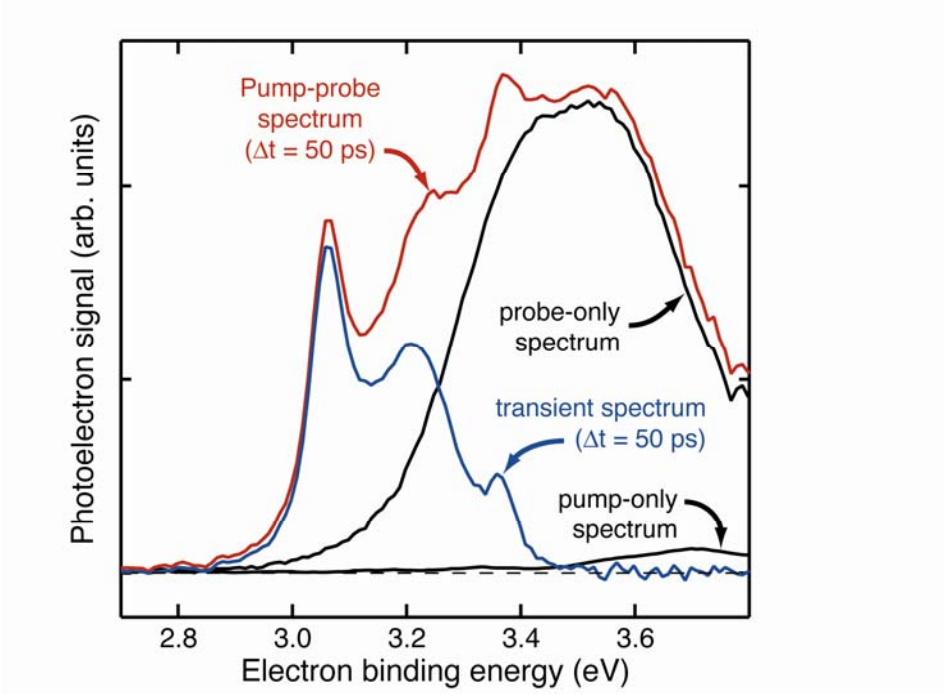

Figure 4.2 Determining the transient spectrum for $IBr^-(CO_2)$ A′ studies. The pump-probe spectrum taken at Δt = 50 ps (red trace) for the A′-state photodissociation studies contains signals from direct photodetachment by the individual pump and probe pulses. These one-photon signals from pump-only or probe-only spectra (black traces) are subtracted from the red trace. The difference spectrum for Δt = 50 ps (blue trace) is the transient time-resolved signal from consecutive pump-probe pulses. The transient spectrum is determined in this way for all time delays studied. Also, the same background correction is made for the B-state photodissociation studies.

4.3 TRPES of $IBr^-(CO_2)$ A'-state photodissociation

Dissociation of $IBr^-(CO_2)$ after excitation to the A′ $^2\Pi_{1/2}$ electronic state is followed in real time with photoelectron spectroscopy. Figure 4.3 depicts the experimental scheme for this dissociation. The $IBr^-(CO_2)$, in its ground electronic state, $\tilde{X}\ ^2\Sigma^+$, interacts with the pump pulse

(788 nm) and is promoted to the $A'\ ^2\Pi_{1/2}$ surface. On the excited-state surface, the $IBr^-(CO_2)$ dissociates to one of three channels, Eqn. 4.3a – c.[30] Strictly speaking, the electronic states of $IBr^-(CO_2)$ differ from those of bare IBr^- and should be described by a different set of state labels. Yet, the "average" electronic structure perturbation induced by a single CO_2 solvent molecule is quite small, and the electronic states of the cluster anion bear close resemblance to those of IBr^-. Similar to IBr^-, the A′ surface of $IBr^-(CO_2)$ has the excess charge localized on the I atom at increasing I–Br distance. Thus, the products of adiabatic dissociation (channels 1 and 2 in Fig. 4.3) are I^- and $I^-(CO_2)$, respectively, and the nonadiabatic product channel (3) is the charge-transfer channel that yields Br^-. The probe laser pulse photodetaches the excess electron at some delay time to follow the evolution of the dissociating complex, and the photoelectron spectrum is taken at each Δt. The right side of Fig. 4.3 depicts the calculated potential energy curves for $IBr^-\ \tilde{X}\ ^2\Sigma^+$ (solid, red trace) and $A'\ ^2\Pi_{1/2}$ (solid, black trace) electronic states, while the dashed traces are the same potential energy curves solvated by the CO_2 binding energy (~ 200 meV) and represent the minimum energy path for each of the multidimensional electronic surfaces.[43,65,67] Three of the four asymptotes correspond to the available dissociation channels, where channel 1 and 2 are a product of dissociation along the A′ state and the third channel occurs following a nonadiabatic transition to the ground electronic state.

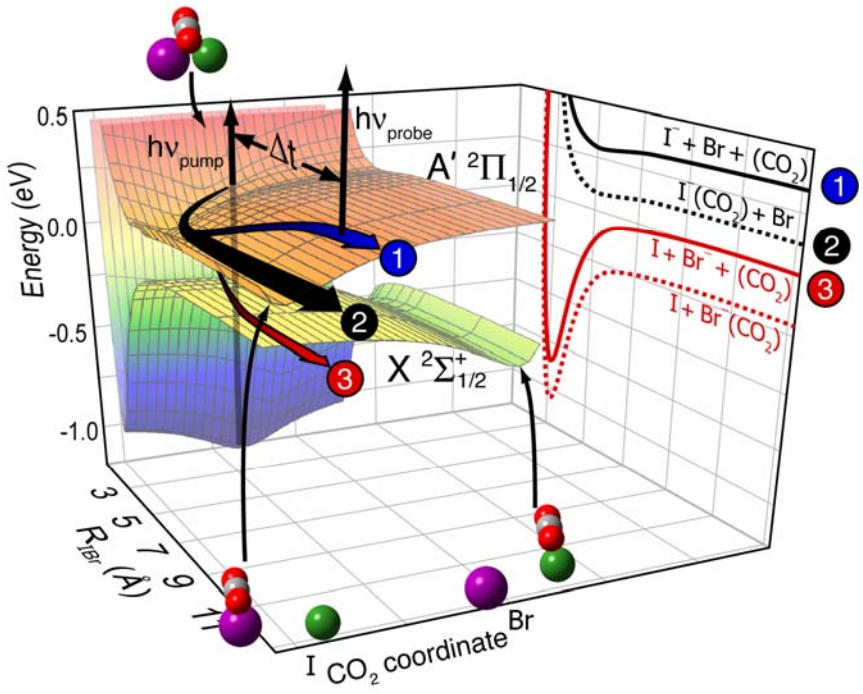

Figure 4.3 Schematic diagram for photodissociation of $IBr^{-}(CO_2)$ following excitation to the A′ $^2\Pi_{1/2}$ surface. The lower potential energy surface is the $\tilde{X}\ ^2\Sigma^+$ electronic state, and the higher energy surface is the A′ $^2\Pi_{1/2}$ electronic state. The surfaces are plotted as a function of the I–Br bond length and the CO_2 position, where the two extremes are the CO_2 residing on the I (purple sphere) or Br (green sphere) end. The pump-probe experimental scheme is shown with arrows. The three dissociation channels are depicted by numbers 1 – 3. The three dissociation channels are also shown on the right side that displays the potential energy curves for the $\tilde{X}$ (red traces) and A′ (black traces) electronic states. The solid curves are the calculated bare IBr^{-} potential energy curves, and the dotted curves represent the binding energy of CO_2, which is ~ 200 meV.

4.3.1 Experimental Results

By taking the time-resolved photoelectron spectrum of $IBr^{-}(CO_2)$, the electronic character of the dissociating species is tracked in real time, which directly yields the time that the charge localizes and elucidates the mechanism for charge transfer. Figure 4.4 plots the photoelectron spectra versus electron binding energy (eBE) at Δt in a 3D contour plot. The spectra are obtained from Δt = -200 fs (-0.2 ps) to +50 ps. At the earliest times, there is one

broad spectral feature that shifts from eBE = 3.05 eV to 3.15 eV. This single spectral feature begins to split into three distinct peaks around Δt = +200 ps. For the next 200 ps, the resulting three spectral features drastically shift in energy. Between Δt = 400 fs and 1ps, some minor energy shifting occurs, where the three peaks converge towards the known photodetachment energies of I^-, $I^-(CO_2)$, and Br^-. After Δt = 1 ps, the spectra remain constant for the duration of time delays measured, which strongly suggests that the dissociation is complete.

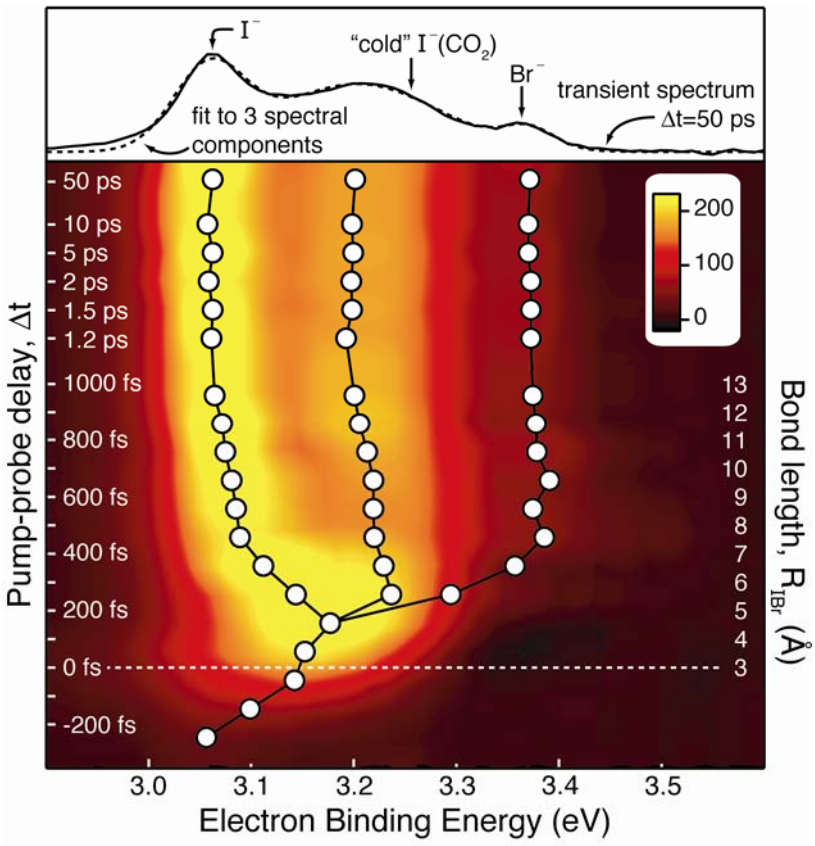

Figure 4.4 Time-resolved photoelectron spectra of dissociating $IBr^-(CO_2)$ following excitation to the A′ electronic state. The 3D contour plot shows the transient photoelectron spectra as a function of eBE and Δt, where Δt = -200 fs to +50 ps. The right axis shows the approximate corresponding I–Br bond length for various time delays. The white circles are the fitted, Gaussian peak centers at Δt. The top panel contains the transient spectrum (solid trace) for Δt = 50 ps and the corresponding fit with three independent Gaussian peaks (dotted trace). The three arrows above the spectral features indicate the measured transitions from I^-, $I^-(CO_2)$, and Br^-.

The Δt = 50 ps spectrum is representative of fully-separated photofragments and is shown in the top panel of Fig. 4.4. The three peaks in the transient spectrum (solid, black trace) correspond to transitions from I^-, $I^-(CO_2)$, and Br^-, which are known from independent calibration spectra to lie at eBE = 3.059, ~3.25, and 3.364 eV, respectively. The calibrated transitions are marked with arrows in the top panel of Fig. 4.4. The atomic fragment features in the transient spectrum coincide perfectly with the calibrated transitions; however, the $I^-(CO_2)$ transition lies ~ 50 meV lower in binding energy than the calibrated transition. The calibrated $I^-(CO_2)$ feature arises from photodetaching an electron from "cold" $I^-(CO_2)$ clusters that are easily generated in our anion source. The ~50 meV shift means that the $I^-(CO_2)$ produced in the photodissociation is vibrationally hot, and this shift is consistent with the "hot" $I^-(CO_2)$ occupying ¼ of the I^-–(CO_2) well depth.[65] The three spectral features at Δt = 50 ps are fit to a sum of three Gaussian peaks, which is the dotted line in the top panel. Assuming approximately equal photodetachment cross sections of the charged photoproducts, the fit results in a photodissociation product yield of 31% I^-, 64% $I^-(CO_2)$, and 5% Br^- following excitation to the A′ electronic state, which is consistent with earlier photofragmentation studies from our lab (Eqns. 4.3).[30,33,43] A similar fit is performed for all the spectra with three features (Δt > 200 fs). The Gaussian peak centers are marked with white circles on the contour plot. For Δt < 200 fs, there is only one spectral feature that is fit to a single Gaussian, and its center is also shown with a white circle.

The division of the single spectral feature into three components around Δt = 200 fs is indicative of the excess charge in the cluster beginning to localize onto the photofragments. Between the pump-probe delays of 200 and 400 fs there are drastic changes in the transient

spectra. This indicates a period of transition where the electronic structure of the cluster evolves from that of excited $IBr^-(CO_2)$ (the so-called "molecular" regime) to that of the isolated photofragments. After 400 fs, the transient spectral features are still evolving but to a lesser degree; this suggests that the excess charge stays localized but is influenced by the other departing photofragments. After 1 ps, the charged fragment no longer interacts with its counterpart, and the spectral features remain constant. Crucially, the transient peak attributed to the Br^- fragment appears during the transition from the "molecular" to the dissociated regime, which shows that the charge transfer from I to Br occurs by 400 fs. To determine a more accurate charge-transfer time, the photoelectron signal of the Br^- channel (slice of the spectra centered at 3.36 eV) is fit to an instrument-limited rise (200 fs) convoluted with a step function, which is centered at 350 ± 20 fs. The 350-fs time delay corresponds to the charge-transfer time and will be discussed later in more detail.

The experimental data directly yield the electron transfer time, which is a key quantity for unraveling the details of the nonadiabatic photodissociation dynamics of $IBr^-(CO_2)$ following excitation to the A′ electronic state. The transient photoelectron spectroscopy also sheds light on the evolution of the electronic structure during photodissociation and, importantly, on the role of the CO_2 solvent molecule. The transient spectra are quite complex and their interpretation requires high-level calculations and molecular dynamics modeling to elucidate the charge-transfer mechanism.

4.3.2 Calculations

The theoretical contribution to this work is significant and encompasses two research groups: Robert Parson at the University of Colorado, Boulder and Anne McCoy at The Ohio

State University with their respective graduate students Matthew Thompson and Samantha Horvath. This section provides a summary of the theoretical work but a more detailed explanation can be found in other references directly related to this chapter.[25,26,43,45,85,86]

The molecular dynamics (MD) simulations utilize an effective Hamiltonian approach developed by Parson and coworkers that calculates the potential energy surface of the $IBr^-(CO_2)$ "on the fly".[87,88] The IBr^- anion is treated quantum mechanically in a truncated basis set of isolated electronic states, while the CO_2 solvent is treated classically. The IBr^- basis set contains the ground and all the valence-excited states to yield six doubly degenerate electronic states, thus creating a 12 x 12 matrix. The isolated IBr^- electronic states have been calculated previously with MOLPRO 2002.6 at the multi-reference configuration interaction level with singles and doubles level of theory and including spin-orbit coupling (MR-SO-CISD).[89] The matrix represents the effective Hamiltonian where the isolated IBr^- is part of the diagonal terms and the solute-solvent interactions contribute to both the diagonal and off-diagonal terms. The eigenvalues of this effective Hamiltonian define the solvated IBr^- curves. This method accounts for the solvent-induced charge flow within the solute but cannot account for charge flow from the IBr^- solute to the CO_2 solvent, since the CO_2 is treated classically. By diagonalizing the effective Hamiltonian at each time step in the simulation, the energies and forces are determined, which propagates the trajectories using Anderson's "velocity Verlet" algorithm.[90] The nonadiabatic transitions are simulated using a variation of the nonphysical surface-hopping algorithm of Tully and Hammes-Schiffer.[91,92] In this algorithm, the solvent polarizes the solute charge distribution but remains rigid and cannot acquire any of the excess charge.

The MD simulations are performed at various total internal energies for $IBr^-(CO_2)$, 200 – 1400 cm^{-1}, which translates to T_{vib} = 80 – 250 K. For these simulations, five ensembles are run, where each ensemble is at a particular starting temperature (80, 120, 160, 200, or 250 K) and contains 1000 trajectories. To create the initial ensemble, each trajectory roams on the ground electronic state surface at a certain internal energy for 5 ns, and the geometry of the cluster is sampled every 5 ps. The sampled geometry of $IBr^-(CO_2)$ is promoted to the A′ surface where the internal motion of the cluster is preserved from the ground state. To keep the simulation consistent with the experiment, the I–Br bond length is adjusted so that the $\tilde{X}\ ^2\Sigma^+ - A'\ ^2\Pi_{1/2}$ energy gap is consistent with the experimental excitation energy (E_{photon} = 1.57 eV). The trajectory continues to propagate on the upper surface until the I–Br separation reaches 20 Å, where the simulation is stopped.

The photodissociation products within the simulations vary depending on internal temperature, T_{vib}. In general, the $I^-(CO_2)$ products decrease as the temperature increases, while the I^- products increase with temperature. Also, channel 3 (Br^-) opens slightly (<1% yield) at the higher internal temperature. In the simulations, the cluster temperature is strongly correlated with the geometry of the CO_2 around the solute prior to dissociation (Fig. 4.5(a)). As temperature increases, the CO_2 samples a larger geometry range in the ground electronic state, which in turn is directly related to the product yield. As can be seen in Fig. 4.5(b), the formation of $I^-(CO_2)$ occurs when the CO_2 is over the I–Br waist or closer to the I end (θ_{ClBr} = 180°) but does not form when the CO_2 is near the Br end (θ_{ClBr} = 0°).

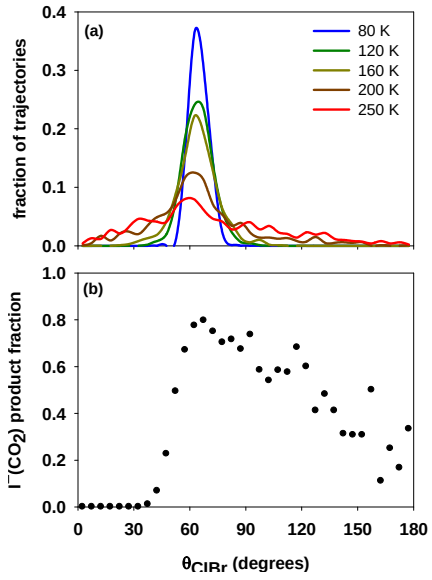

Figure 4.5 The geometry of CO_2 prior to photodissociation (a) At low internal temperatures, the CO_2 molecule sits near the waist of IBr^-. As the temperature increases, the CO_2 molecule samples a larger geometry around the solute and can be found on the Br ($\theta_{ClBr} = 0°$) or I ($\theta_{ClBr} = 180°$) end. (b) The formation of channel 2, $I^-(CO_2)$, occurs when the CO_2 molecule is around the waist of the solute or near the I end.

To gain insight into the role of intra-cluster vibrations on the charge-transfer mechanism, additional high-level *ab initio* calculations are performed at various points along the MD trajectories. These additional calculations utilize newer potential energy curves for the IBr^- and $IBr^-(CO_2)$ that did not exist at the time of the MD simulations The new potentials are calculated at the same level of theory (MR-SO-CISD) except with the electronic structure package of MOLPRO 2008.1 and more recent pseudopotentials, aug-cc-pVTZ-PP, that were not available when the MD simulations were originally run.[93-95] These newer potential energy curves do not vary much from the older curves used for the MD simulations. Figure 4.1 plots these newer potentials for the six lowest energy electronic states of IBr^-. The results of these calculations also yield the 36 lowest energy electronic states for neutral IBr, which are shown later in the

chapter. The high-level *ab initio* calculations focus on the effect of the CO_2 bending motion on the cluster dissociation by computing the electronic energies at different OCO bend angles. In addition, the dipole moments of the clusters are calculated in order to estimate the degree of charge redistribution at each point in the MD trajectory.

4.3.3 Discussion

The charge hop mechanism is solvent mediated by a single CO_2 molecule. Following excitation to the A′ state, the charge on IBr^- quickly localizes onto the I atom that causes the CO_2 to be attracted to the excess charge. As the CO_2 molecule approaches the I atom, it becomes more bent and acquires more of the excess charge. The proximity of the CO_2 influences the energies of the electronic states, such that as the I–C distance decreases the energy gap between the A′ and A/$\tilde{X}$ states decrease. Once the gap is small enough, the charge hops from the I to the Br, and in the absence of the excess charge, the initially bent CO_2 is left vibrationally excited, which helps to bridge the energy gap for charge transfer. The perturbation of the electronic state energies from CO_2 and the ability of the CO_2 to remove excess energy are critical for the nonadiabatic process. Figure 4.6 summarizes the experimental data and important theoretical findings, which ultimately lead to this mechanism for charge transfer.

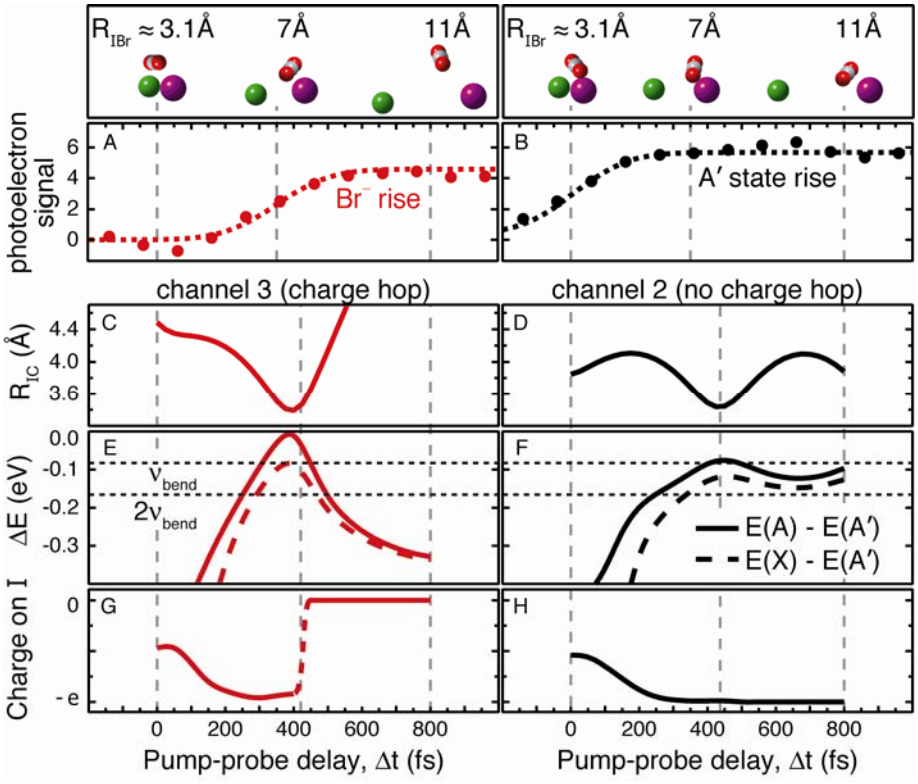

Figure 4.6 MD simulations of $IBr^-(CO_2)$ following photoexcitation to the A′ electronic state. The left-hand panels (red) represent channel 3 dynamics, while the right-hand panels (black) represent the dynamics of channel 1 and 2, (B), or just channel 2, (D), (F), and (H). (A) and (B) plot the growth of the experimentally measured photoelectron signals for the Br^- and I^-/I^-CO_2 (A′ state) spectral features, respectively. (C) and (D) graph the calculated I–C distances as a function of Δt. The calculated energy differences between the $\tilde{X}\ ^2\Sigma^+$ and A′ $^2\Pi_{1/2}$ (dashed line) or the A $^2\Pi_{3/2}$ and A′ $^2\Pi_{1/2}$ (solid line) electronic states are plotted as a function of Δt in (E) and (F). (E) contains the calculated energy gap for an $IBr^-(CO_2)$ cluster with an OCO angle of 180°, while (F) for an OCO angle of 175°. The horizontal dashed lines in (E) and (F) correspond to 1 or 2 quanta in the CO_2 bend. (G) and (H) show the calculated evolution of the excess charge on the I atom. The experimental Δt corresponds to an I–Br bond distance, which is shown above the panels as snapshots of the dissociating $IBr^-(CO_2)$ for a trajectory that leads to channel 3 (left) or channel 2 (right).

Fig. 4.6(A) and (B) contain the photoelectron signal for the Br^- and the $I^-/I^-(CO_2)$ (A′) channels, respectively. These signals are fit to an instrument-limited rise that is convoluted with a step function. Both the I^- and $I^-(CO_2)$ dissociation channels occur on the A′ electronic surface,

and thus are labeled together as the A′ state rise. The fit to the A′-state signal in Fig. 4.6(B) is centered at 0 fs, showing that we detect the excited clusters immediately following the absorption of a pump photon. This early photodetachment signal is reminiscent of the results from Sanov and coworkers on bare IBr^- and previous photodissociation studies on neutral Br_2 where the signal rapidly localizes onto a dissociating fragment.[84,96] In contrast, the fit for the Br^- channel, Fig. 4.6(A), has an instrument-limited rise that is delayed by 350 ± 20 fs, suggesting that at this time the charge is transferred from the I or $I(CO_2)$ to the Br fragment. Therefore, the nonadiabatic charge transfer occurs 350 fs following excitation to the A′ state.

Snapshots of the MD simulations at various time delays are shown above panels A and B for Fig. 4.6. The left-hand side shows the snapshots for an MD simulation that yields the Br^- charge-transfer channel, while the right-hand side pictures the snapshots from a simulation that results in the $I^-(CO_2)$ channel. The snapshots capture the geometry for Δt = 0, 350, and 800 fs and correspond to an I–Br separation of ~3.1, ~7, and ~11 Å, where the I and Br are the purple and green spheres, respectively. Thus, the MD simulations show that the charge transfer to Br occurs at an I–Br distance of ~ 7 Å with the CO_2 molecule positioned relatively close to the I atom.

The results of the calculations are shown in Fig. 4.6(C) – (H), where the left panels represent a trajectory that yields a charge hop and the right panels show a trajectory that yields $I^-(CO_2)$. For the charge hop trajectory (left panels), the CO_2 solvent is initially attracted to the I atom following photoexcitation of $IBr^-(CO_2)$ to the A′ state, which is shown by the decrease in the I–C distance (Fig. 4.6(C)). As the CO_2 molecule approaches the I atom, the electronic energy gaps between the A′ excited state and the lower energy A and $\tilde{X}$ states decreases (E), where

electronic state energies are calculated for an OCO angle of 180°. At the same time, the charge becomes localized onto the I atom (G), which increases the attraction of the CO_2 molecule to I. When the energies of the A′ state and lower electronic energy states are degenerate, then the charge hops from I to Br, which occurs at $\Delta t = 400$ fs and at an I–Br distance ($R_{I–Br}$) ≈ 7 Å. Following the charge hop, the CO_2 molecule is no longer attracted to the I atom and the I–C distance increases. Simultaneously, the energy gap between the A′ state and lower energy electronic states increases, and the charge remains localized on Br. For the charge hop channel, the proximity of the CO_2 molecule to the charged I atom influences the energy gap between the excited and lower energy electronic states; therefore, the nonadiabatic event is solvent mediated by the CO_2.

If the CO_2 molecule does not perturb the electronic states enough, then the charge does not transfer, as is shown in the right panels. The initial 400 fs of this trajectory is very similar to the left panels. However, in this trajectory, the electronic energy gap between the excited A′ state and the lower energy electronic states, where the energies for the electronic states are calculated for an OCO angle of 175°, is too large for a charge transfer. Following the initial "bounce" of CO_2, the energy of the electronic states varies slightly and the charge stays localized on the I atom, thus the CO_2 molecule continues to "bounce" against the I atom to yield vibrationally hot anion clusters.

The MD simulations capture the essence of the charge-transfer mechanism that is as the CO_2 distance to the I atom decreases there is a corresponding decrease in the energy gaps between the A′ and A/$\tilde{X}$ electronic states, which allows the charge to be transferred. However, the simulations underestimate the yield of the Br^- channel (< 1%). To make the simulations

more realistic and increase the yield for the Br^- channel, the CO_2 molecule should not be treated classically by allowing for CO_2 to bend and acquire partial charge during the photodissociation.

Experiments by Neumark and coworkers measured the photoelectron spectrum of $I^-(CO_2)$ and determined the OCO angle to be 175° in the equilibrium geometry.[68,69] This is a result of partial delocalization of the charge into the lowest unoccupied molecular orbital (LUMO) of CO_2. The results of our high-level *ab initio* calculations on $IBr^-(CO_2)$ are consistent with the experimental results of Neumark and coworkers, and we have found that as the I–C distance decreases the OCO angle becomes smaller (< 175°), which means more charge is delocalized into the LUMO of the CO_2 molecule. In photodissociating $IBr^-(CO_2)$, the I–C distance and OCO angle should become even smaller than the equilibrium $I^-(CO_2)$ distance and OCO angle determined by Neumark and coworkers; therefore, more of the partial charge is being removed from the I atom and delocalized to the CO_2 molecule, which will aid in the charge transfer mechanism. In addition, a bent CO_2 molecule in the presence of an anion would map onto a vibrationally excited CO_2 state after the electron has been removed, thus the CO_2 molecule would leave with a few quanta of vibrational energy (1 and 2 quanta of bend excitation are marked as dashed lines in Fig. 4.6(E) and (F)). The removal of excess energy by CO_2 vibrations allows the charge transfer to occur at larger energy gaps between the electronic states. Therefore, our additional calculations and the results of Neumark and coworkers strongly suggest that the yield of the charge transfer channel in the simulations would increase if the CO_2 molecule could have vibrational excitation and acquire partial charge throughout the dissociation.

In Fig. 4.6(G) and (H), the calculated charge on I does not include partial charge on the CO_2 molecule and, therefore, does not give an accurate description of how CO_2 influences the charge distribution. Since we did not have a good method for calculating the charge distribution within $IBr^-(CO_2)$ as it dissociates, we use the change in the dipole moment as a proxy for the charge distribution. Figure 4.7 plots the change in the dipole moment along the I–Br bond axis ($\Delta\mu_z$). The solid curve with circles and the red curve with triangles compare differences in the dipole moments of $IBr^-(CO_2) - [IBr^- + CO_2]$ or $IBr^-(CO_2) - [I^-(CO_2) + Br]$, respectively. In both traces, the $\Delta\mu_z$ favors the excess charge on the Br end between 200 and 400 fs. This shows that the presence of CO_2 influences the dynamics by shifting the charge towards Br in a time frame that is consistent with the observed charge transfer. The $\Delta\mu_z$ provides further evidence that the simulations underestimate the CO_2 contributions and, therefore, the charge-transfer channel.

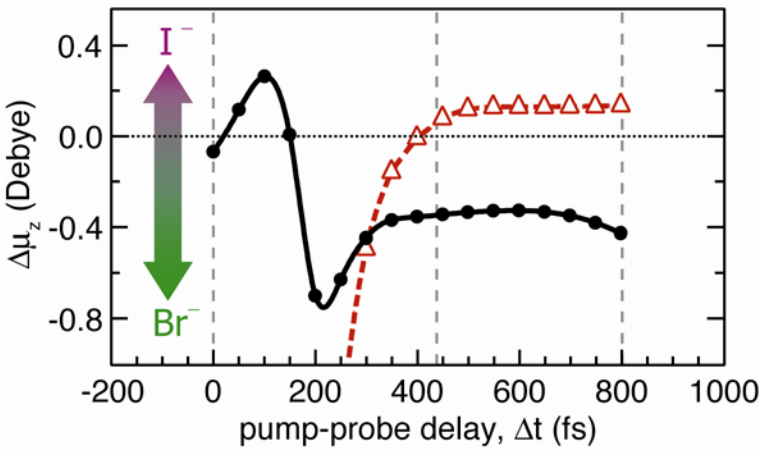

Figure 4.7 The calculated change in the dipole moment ($\Delta\mu_z$) along the I–Br bond axis. The black circles and trace represent the difference between the dipole moments of $IBr^-(CO_2)$ and $[IBr^- + CO_2]$. The red triangles and trace represent the difference between the dipole moments of $IBr^-(CO_2)$ and $[I^-(CO_2) + Br]$. The double-sided arrow indicates when the excess charge favors I^- or Br^-.

4.4 TRPES of IBr^- B-state photodissociation

When bare IBr^- ($\tilde{X}\,^2\Sigma^+$) is excited to the second optically bright state ($B\,^2\Sigma^+$), the IBr^- anion dissociates completely into I* + Br^-, Eqn. 4.2.[30,33,43] The time scale for IBr^- dissociation is determined with TRPES, and the schematic diagram is shown in Fig. 4.8. The experimental scheme is shown on top of the calculated potential energy curves of IBr^- and IBr, which have been described in section 4.3.2. Fig. 4.8 shows the anion, prepared in its ground electronic state ($\tilde{X}\,^2\Sigma^+$, thick black curve), interacting with the pump laser pulse. Absorption of a pump photon promotes the IBr^- anion to the $B\,^2\Sigma^+$ state (thick blue curve) at t = 0. As IBr^- dissociates into I* (purple sphere) + Br^- (green sphere), the probe laser pulse photodetaches an electron from the dissociating anion at Δt. The neutral curve that is bolded has the correct asymptote (I* + Br) for photodetachment from the B electronic state. This bolded curve is used for the calculated TRPES because it is the neutral state that is expected to be accessed by loss of one electron from the B state near the IBr^- geometry at t = 0. As the IBr^- anion evolves along the B state, more neutral states could become available for photodetachment transitions. However at longer bond lengths, these states become energetically degenerate with the bolded, neutral state, and since the photodetachment cross sections for these states are not known, we do not include the other neutral states in the calculated TRPES at longer I–Br bond lengths.

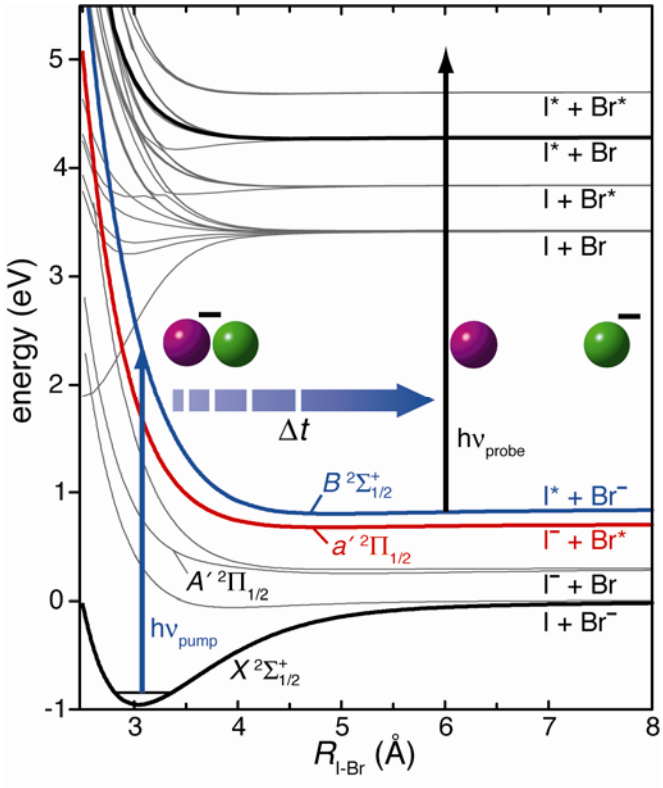

Figure 4.8 The schematic diagram for TRPES of dissociating IBr^- following excitation to the B state. The calculated potential energy curves for IBr^- and IBr are shown with the relevant states bolded. The IBr^- in its ground electronic state is promoted to the B $^2\Sigma^+$ state with the pump pulse at t = 0. At some time later, Δt, the probe pulse interacts with the dissociating fragments to remove an electron. The I and Br atoms are depicted by the purple and green spheres, respectively.

4.4.1 Results

The TRPES for IBr^- following excitation to the B $^2\Sigma^+$ electronic state reveals photodetachment signal from only Br^-. The TRPES data are shown in Fig 4.9(a) for various time delays, Δt = -0.2 – 1.2 ps. Since our probe laser pulse has sufficient energy, the photodetachment of Br^- yields both the ground state of Br (feature at 3.36) and the spin-obit excited state, Br* (3.82 eV), which is shown in the reference spectrum (b). These features

exhibit minimal spectral shifting as the Br and Br* peaks grow in intensity ($\Delta t = 0.2 – 0.5$ ps), and the peaks remain constant at the reference position after 0.5 ps. The abrupt formation of Br^- is consistent with previous photodissociation studies and the A′ state photodissociation studies for IBr^- and $IBr^-(CO_2)$.[84,96] In Fig. 4.9(c), the integrated signal for both Br (black circles) and Br* (white circles) is plotted at each Δt, and fit to an instrument-limited rise convoluted with a step function. The fit is centered at $\Delta t = 200 \pm 20$ fs (0.2 ps) for both Br and Br*. As in the A′-state studies, one would expect to observe photodetachment signal from a B-state complex at $\Delta t \sim 0$ fs, which quickly yields the Br^- product since this is the adiabatic channel. We turn to theoretical calculations to aid in an explanation for the lack of photodetachment signal in the "molecular" regime.

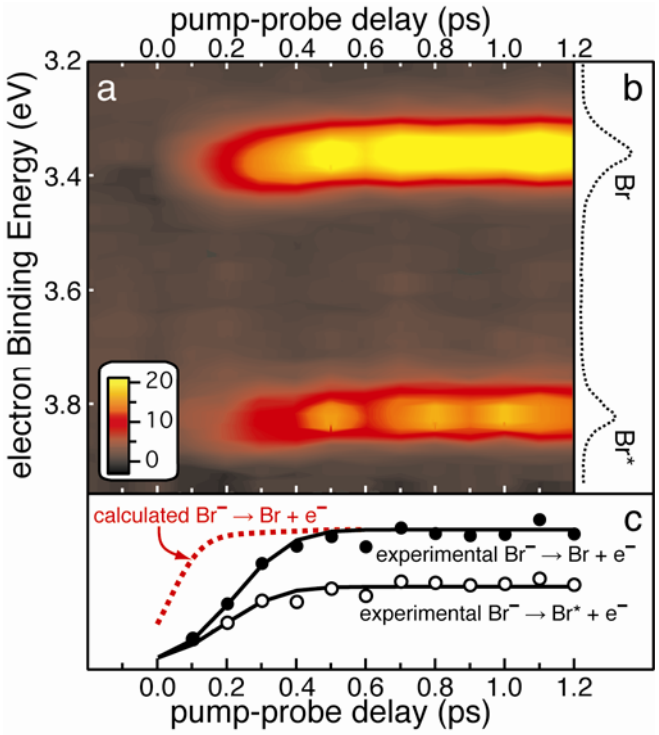

Figure 4.9 Time-resolved photoelectron spectra of IBr^- photodissociating along the B-electronic state. (a) The 3D contour plots the spectra as a function of delay time, Δt, and electron binding energy. (b) The reference spectrum shows transitions to Br and Br* and is taken under the same experimental conditions. (c) The integrated signal for the Br (filled, black circles) and Br* (unfilled, black circles) channels along with the fits for each channel are shown. The integrated photoelectron intensity from the calculated TRPES for the Br channel is shown as the dashed, red trace.

4.4.2 Calculations

The quantum dynamics calculations performed on IBr^- photodissociation along the B state have been previously described; therefore, only a brief summary is provided here. [25,26,85] These calculations use the previously generated potential energy curves and sinc-discrete variable representation to evaluate the nuclear states that correspond to the IBr^- and IBr electronic states that are involved in the dynamics (solid, black and blue curves in Fig. 4.8).[97,98]

The theoretical model used to calculate the IBr^- B-state TRPES is almost identical to that used for the IBr^- A′ state, and the model has been previously applied to the photodissociation of I_2^- by Miller and coworkers.[85,86,99] Only the final equations are given. For these calculations, the vibrational temperature of IBr^- is 200 K. The wave packet for each thermally populated vibrational state of the anion ground state is placed on the B state and propagated in time. The overlap between the wave packet on the B state of IBr^- and eigenstates of the accessible neutral surface (solid, black neutral curve in Fig. 4.8) are evaluated. As mentioned earlier, the bolded, neutral curve represents the only neutral state that can be accessed by loss of one electron from the B state near t = 0. The signal for the time-resolved photoelectron spectra as a function of the electron kinetic energy, ε, and pump-probe delay time, Δt, is calculated by evaluating Eqn. 4.5.

$$P(\varepsilon,\Delta t) = \hbar^{-4} \sum_n [\int_{-\infty}^{\infty} dt\, F_2(t-\Delta t) e^{[i/\hbar(E_n+\varepsilon-E_{probe})t]} \times \left\{\sum_m c_m \langle\chi_n|\phi_m\rangle\, e^{[-i/\hbar(E_m)t]} \times \int_{-\infty}^{t} dt' F_1(t') e^{[i/\hbar(E_m-E_g-E_{pump})t']}\right\}]^2. \quad \text{Eqn. 4.5}$$

The $F_1(t')$ and $F_2(t-\Delta t)$ are the functional forms for the pump and probe pulses with energies of E_{pump} (3.128 eV) and E_{probe} (3.967 eV), respectively. The functional forms for the pump and probe pulses are

$$F_j(t) = sech^2(\frac{t}{f\delta_j}), \quad \text{Eqn. 4.6}$$

where δ_j is the full width at half maximum for the pump (200 fs) and probe (140 fs) pulses and $cosh[1/(2f)] = \sqrt{2}$. The coefficients *n*, *m*, and *g* are the nuclear eigenstates of the solid, black electronic state of neutral IBr, the B electronic state of IBr^-, and the $\tilde{X}\,^2\Sigma^+$ electronic state of IBr^-, respectively. The term c_m equals $\langle\phi_m|\psi_g\rangle$.

To understand how the wave packet on the B state is dressed by the pump pulse (i.e., how the wave packet has been prepared following interaction between the ground state wave function and the pump pulse with a defined width), Eqn. 4.7 is evaluated. This calculation gives the time-dependent probability amplitude for the wave packet as a function of $R_{I–Br}$ and delay time, Δt.

$$\Xi_d(R,\Delta t) = [\sum_m c_m e^{[-i/\hbar(E_m)\Delta t]}\phi_m(R)\ \int_{-\infty}^{\Delta t} dt' F_1(t') e^{[i/\hbar(E_m - E_g - E_{pump})t']}\ ]^2. \quad \text{Eqn. 4.7}$$

Equation 4.7 is the expression for P(ε, Δt) when $F_2(t - \Delta t) = \delta(t - \Delta t)$ and is projected onto the $R_{I–Br}$ coordinate.

4.4.2 Discussion

The delayed rise in the photodetachment signal is surprising since direct, adiabatic dissociation is typically a prompt process. As can be seen by the dotted, red trace in Fig 4.9(c), the calculated TRPES (Eqn. 4.5) predicts that photodetachment signal from photoexcited IBr^- should appear well before the measured 200 fs. However, this is not the case. One likely explanation is that there is a poor photodetachment cross section from the B state of IBr^- to the neutral eigenstates in the "molecular" (i.e., not fully dissociated) regime. These particular calculations of the TRPES signal do not explicitly incorporate the photodetachment cross section, and its quantitative determination is difficult. Therefore, we turn to a qualitative description of the electronic states of IBr^- and IBr in order to get a sense of the photodetachment efficiency during IBr^- dissociation.

From the electronic structure calculations, the excess charge distribution for each of the electronic states is determined for the six lowest energy electronic states, Fig. 4.10(a). The rapidly changing charge distribution implies that the electronic character of all states of IBr^-

(including the B state) drastically shifts as the I–Br length is increased. Since the B state correlates to the asymptotic products, I* + Br^-, the charge has to be fully localized on the Br at large I–Br distances. However, the electronic character of the B state at 3.01 Å has more charge on the I atom. It is not until 6 Å that the charge becomes localized on the Br. The changing electronic character of the B state could lead to delayed photodetachment signal from Br^-. In other words, the photodetachment cross section to the neutral state might not be large enough to detect until the charge distribution has shifted to Br.

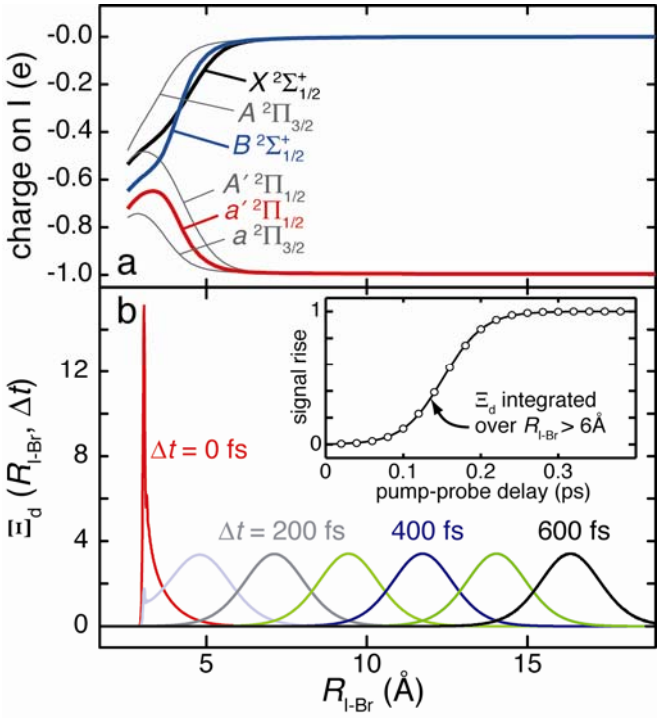

Figure 4.10 The calculated charge and quantum wave packet propagations for IBr^-. (a) The charge on the I atom for each electronic state of IBr^- as a function of $R_{I–Br}$. (b) The Ξ_d is plotted as a function of $R_{I–Br}$ at various time delays, Δt. The inset contains the integrated Ξ_d after charge has localized on Br ($R_{I–Br} > 6$ Å) as a function of Δt. The inset is a good approximation to the experimental TRPES signal if the cross section for photodetachment is dependent on charge localization.

To take this one step further, we look at the time-dependent probability amplitude for the dressed wave packet on the B state, Ξ(R, Δt), Eqn. 4.7. The Ξ(R, Δt) is plotted as a function of $R_{I–Br}$ at various delay times, Δt, in Fig. 4.10(b), where the propagating wave packet is a result of promoting only the $\upsilon = 0$ wave function of the ground electronic state. The inset of Fig. 4.10(b) contains the integrated Ξ(R, Δt) for $R_{I–Br} > 6$ Å. This integration assumes that the photodetachment cross section is negligible until the charge has become localized on the Br atom ($R_{I–Br} = 6$ Å). The rise is delayed by ~160 fs and is reminiscent of the measured photoelectron signal. This approach proved useful in a previous study of Cu–HOH.[100,101] The integration of Ξ(R, Δt) strongly suggests that the cross section for photodetachment is poor at small I–Br distances and it isn't until the charge becomes localized that the photodetachment signal can be measured.

4.5 TRPES of $IBr^-(CO_2)$ B-state photodissociation

Like the A′ $^2\Pi_{1/2}$ state studies, the addition of one CO_2 solvent alters the photodissociation dynamics following excitation to the B $^2\Sigma^+$ state. From previous B-state photodissociation studies of $IBr^-(CO_2)$, we know that the I* + Br^- channel is still available but the lower energy channel, I^- + Br*, opens with the addition of one CO_2 molecule, Eqn. 4.4a and b, respectively.[30,33,43] Unlike the A′-state studies where the typical CO_2 binding energy (~200 meV) is not enough to bridge the energy gap between electronic states (~300 meV), the B state lies close to the lower energy a′ $^2\Pi_{1/2}$ electronic state (~130 meV), which leads to abundant charge transfer. The experimental setup is identical to that shown in Fig. 4.8 for bare IBr^- with the exception that the nearby a′ $^2\Pi_{1/2}$ electronic state (red curve) needs to be considered.

4.5.1 Results

The TRPES results for $IBr^-(CO_2)$ following excitation to the B state are shown in Fig. 4.11(a) for various delay times, Δt = -0.2 – 1.2 ps. The spectra have four peaks that are a result of photodetachment from Br^- (3.36 and 3.82 eV) and I^- (3.06 and 4.00 eV) to yield the ground and spin-orbit excited states of Br and I, respectively. The four spectral peaks appear with a time delay and at a position that is close to the reference peak positions, Fig. 4.11(b). As before, the integrated photoelectron signals for the Br (black circles) and I (white circles) features are fit to an instrument response function convoluted with a step function. For the Br^- channel, the rise is instantaneous and delayed by 250 ± 20 fs. As these Br peaks are growing in (Δt = 0.2 – 0.6 ps), they shift slightly (~50 meV) to lower binding energies until their peak positions are at the reference peak positions, where there is no additional shifting for the remaining time delays. The delay in the photodetachment signal is consistent with the bare IBr^- B-state results, where the experiment does not show photodetachment to Br^- in the "molecular regime" at early time delays. Photodetachment signals from I^- appear much faster than the Br^- photodetachment signals and has an instantaneous rise with a 50 ± 20 fs delay. The relative intensities of the I^- and Br^- photodetachment signals at Δt = 1.2 ps are 40% and 60%, respectively. Assuming equal photodetachment cross sections for the I^- and Br^- photoproducts, the relative yield for the charge hop channel is 40%. This yield is consistent with previous photodissociation studies, Eqn. 4.4.[30,43]

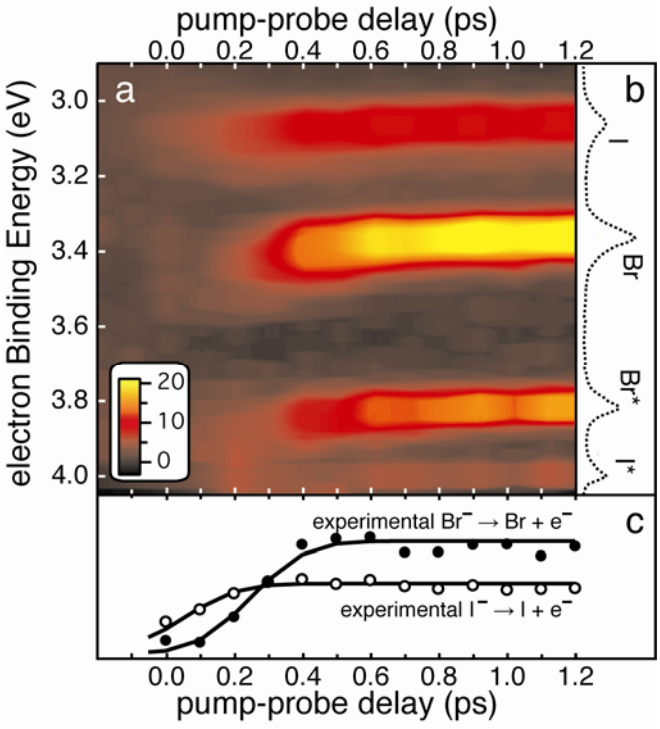

Figure 4.11 Time-resolved photoelectron spectra of $IBr^-(CO_2)$ photodissociation following excitation to the B electronic state. (a) The 3D contour plots the spectra as a function of delay time, Δt, and electron binding energy. (b) The reference spectrum shows transitions to Br, Br*, I, and I*, which are taken under the same experimental conditions. (c) The integrated signal for transitions to Br (black circles) and I (white circles) along with the fits for each transition.

4.5.2 Discussion

The photodissociation of $IBr^-(CO_2)$ following excitation to the B state results in the formation of two channels: the adiabatic channel $I^* + Br^- + CO_2$ and the charge hop channel $I^- + Br^* + CO_2$. A full interpretation of the results, which is similar to the charge-transfer model developed earlier, again requires MD simulations of the photodissociation of $IBr^-(CO_2)$. The MD simulations are almost identical to the procedure described in Section 4.3.2 with the main difference being that the anion at $\Delta t = 0$ is promoted from the ground electronic state to the B state and not the A′ state. Also, these simulations are run for two ensembles at 200 and 250 K

internal energy with each ensemble containing 1000 trajectories. As before, the outcome of the dissociation trajectory depends critically on the position of the solvent molecule in the $IBr^-(CO_2)$ cluster prior to photoexcitation, which in turn depends on the internal energy content of the cluster. Figure 4.5(a) shows the distribution of CO_2 positions about the I–Br bond axis for both the 200 and 250 K ensemble.

Results of two of the MD trajectories at 200 K are shown in Fig. 4.12. The red arrows mark the delay time for solvent-induced charge localization on the I atom and the grey boxes highlight the delay time (~ 160 fs) prior to the calculated full charge localization on Br^- in the bare IBr^- B-state studies. The left-hand plots, (a) – (c), are from a trajectory that stayed on the B-state surface to yield $I^* + Br^- + CO_2$ and did not undergo a charge hop. The right-hand plots, (d) – (e), are the result of a trajectory that did undergo a state change from the B to a′ state, which produces $I^- + Br^* + CO_2$. In both trajectories (panels (a) and (d)), the CO_2 molecule is attracted to the Br atom for the first 100 fs before dissociating away from the Br atom. The motion of the CO_2 molecule decreases the energy gap between the B and a′ electronic states (panels (b) and (e)) and drastically alters the transient charge distribution (panels (c) and (f)) compared to bare IBr^- (Fig. 10(a)). In both of the MD simulations shown in Fig. 4.12, a thick blue line is used to highlight the electronic state on which the trajectory is evolving. The solvent-induced charge redistribution and electronic energy modulation induces an electron transfer in the right-hand MD trajectory. In panel (e), the trajectory hops electronic states roughly at $\Delta t = 150$ fs, where the two states are very close in energy. However, the left-hand trajectory remains on the B state even though the energy gap becomes very small.

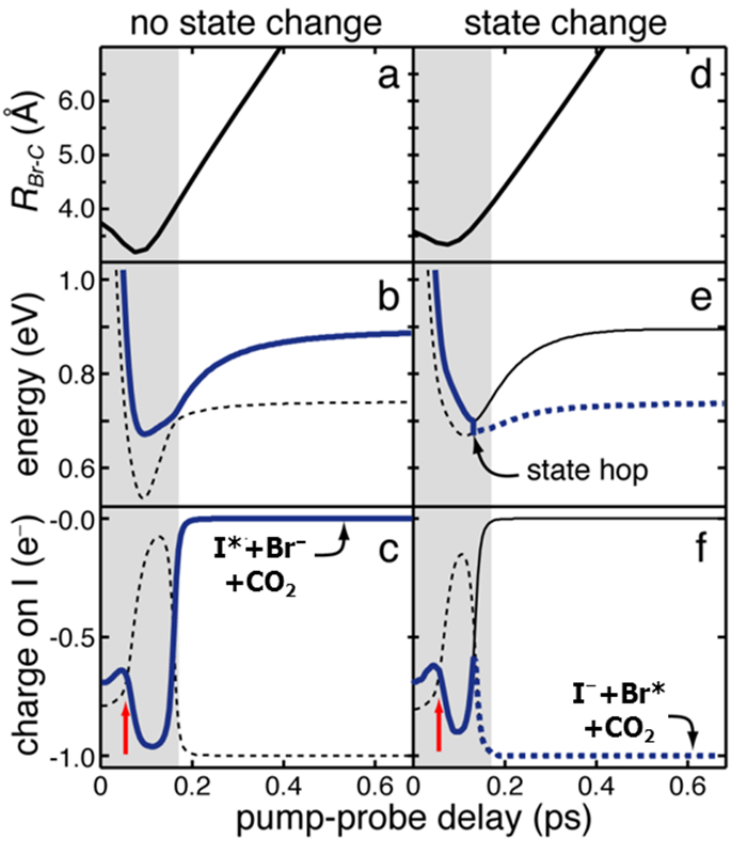

Figure 4.12 MD simulations of $IBr^-(CO_2)$ following photoexcitation to the B electronic state at 200 K. (a) – (c) represent a trajectory that yields the adiabatic products: I* + Br^- + CO_2, while (d) – (e) represent a trajectory that changes electronic states to yield I^- + Br* + CO_2. Panels (a) and (d) plot the calculated Br–C distances as a function of Δt. The calculated electronic energies, (b) and (e), and charge on the I, (c) and (f), for the B (solid trace) and a′ (dotted trace) electronic states are shown, where the thick traces follow the electronic state of the trajectory. The red arrow highlights the time the charge starts localizing on the I atom and the grey box indicates the time prior to the calculated charge localization in bare IBr^-.

The MD simulations effectively capture the mechanism for the charge hop channel, where the influence of the CO_2 molecule on both the energy gap between the B and a′ electronic states and the charge redistribution is critical for the charge transfer to occur. In both trajectories, the charge is on the I atom for at least the first 160 fs, which would lead to the early onset of the I^- photodetachment signal. According to the simulations for the adiabatic channel,

the charge localizes on I at early delay times before drastically switching to Br^- around Δt = 160 fs, which poses the question: why isn't a larger spectral shift seen in the photodetachment signal as the electronic character shifts from being preferentially I^- (red arrow) to Br^- within the B state?

To answer this question, the CO_2 position in the IBr cluster prior to photodissociation is highly correlated with the initial charge distribution and, because of it, is also correlated with the trajectory outcome, shown in Fig. 4.13. For trajectories that undergo a state hop (white circles), the CO_2 molecule is initially near the Br end. For comparison, the two trajectories shown in Fig. 4.12 are for small C–I–Br angles; however, the no-state hop trajectory shown in this figure does not represent the majority of no-state hop trajectories. Instead, it represents the extreme example of solvent-induced perturbation. The majority of the trajectories that remain on the adiabatic surface (no state change) have the CO_2 molecule positioned around the IBr waist or towards the I atom. These trajectories would have different dynamics and experience less of a perturbation to the chromophore; thus, the mechanism would be similar to that observed in bare IBr^- on the B state. Therefore, there is minimal spectral shifting in the photodetachment signal in Fig. 4.11.

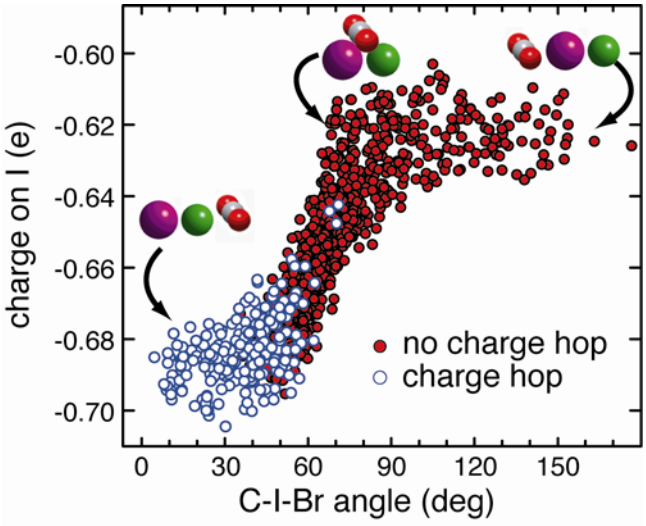

Figure 4.13 Geometries and charge distributions that favor a charge hop. The charge on the I atom at Δt = 10 fs plotted as a function of the CO_2 geometry relative to the I–Br bond axis. The small angles correspond to the CO_2 molecule being closer to the Br end (green ball), whereas the larger angles have CO_2 near the I end (purple ball). The white circles are trajectories that hop electronic states (I^- product), and the red circles are trajectories that do not hop electronic states (Br^- product).

The MD simulations suggest that a subset of trajectories that start from a favorable initial geometry undergo a transient period of charge localization on the I atom. Figure 4.14 contains a histogram of the number of trajectories that exhibit this charge localization on I. The histogram is sharply peaked around Δt = 60 fs, and the inset reinforces this point by showing the integrated total number of trajectories that show this behavior. The calculated time for charge to become localized on the I atom agrees with the experimentally observed rise in signal associated with the I^- channel and is shown as the red arrow in Fig. 4.12.

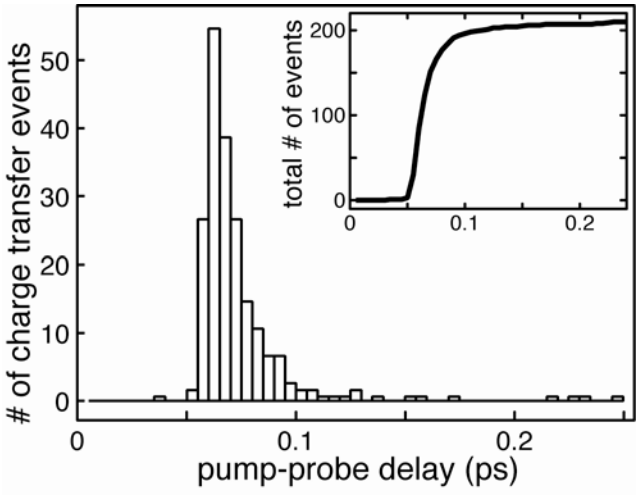

Figure 4.14 Delay times for charge localization on the I atom. The number of trajectories that result in localization of the charge on I for various delay times, Δt, are shown in the main graph. The inset contains the integrated number of trajectories as a function of pump-probe delay time. The time at which the charge becomes localized on I is similar to the pump-probe delay of the experimentally observed I^- photodetachment signal rise, Δt = 60 fs.

Even though the MD simulations capture the mechanism for charge transfer in the $IBr^-(CO_2)$ B-state studies, they do not correctly yield the distribution of the two channels by underestimating the charge hop channel. For simulations at 200 and 250 K, 22% and 28% of the trajectories, respectively, undergo a charge transfer compared to 40% in the experiment. The dependence of the trajectory outcome on the cluster position around the chromophore highlights the influence that the CO_2 solvent has on the dissociation dynamics. The discrepancy between the MD simulations and the experimental results is most likely attributed to the classical treatment of the CO_2 solvent molecule. In the simulations, the CO_2 molecule is kept linear and can only influence the charge distribution on the solute without any of the charge transferring to CO_2. As was the case in the A′-state studies, the additional bending of CO_2 as it approaches the solute would help to delocalize the charge. If the CO_2 molecule could leave with some of the

vibrational energy, then even more excess energy would be removed during the charge transfer, which would allow the state hop to occur at larger energy gaps. By treating CO_2 more realistically in the MD simulations, the number of trajectories that hop states would increase.

4.6 Conclusion

The influence of the CO_2 molecule on the solute is observed throughout these time-resolved studies. When $IBr^-(CO_2)$ dissociates following excitation to the A′ electronic state, around 95% of the photoproducts come from dissociation along the A′ electronic state to yield I^- or $I^-(CO_2)$. About 5% of the products are from nonadiabatic charge transfer to the lower electronic states ($\tilde{X}\ ^2\Sigma^+$ or $A\ ^2\Pi_{3/2}$). The charge transfer to Br occurs around 350 fs, when the I–Br separation is ~7 Å, and is a solvent-mediated process. At early times in the dissociation, the CO_2 molecule approaches the I atom where the charge has already localized. As the I–C distance decreases, the CO_2 molecule becomes more bent and acquires more of the partial charge. In 5% of the trajectories, CO_2 sufficiently influences the solute that the energy gap between the A′ and lower states is small enough that a charge transfer occurs and the excess energy is removed with 0 – 2 quanta in the CO_2 bend.

After excitation to the B state, bare IBr^- cleanly dissociates to $I^* + Br^-$, which are the adiabatic products, and the charge localizes onto Br in 200 fs. The lack of photodetachment signal at early delay times is attributed to a poor photodetachment cross section in the "molecular" regime. With the addition of one CO_2 solvent, a lower energy channel becomes available, which yields $I^- + Br^* + CO_2$. The state hop channel appears much sooner (Δt = 50 fs) than the adiabatic channel (Δt = 250 fs). The geometry of the cluster dictates the resulting dynamics following excitation to the B state.

As in the A′-state studies, TRPES experiments reveal a solvent-mediated charge transfer following excitation of $IBr^-(CO_2)$ to the B state using the same charge-transfer model that was used in the A′-state studies. If the CO_2 molecule is near the Br end, then the CO_2 solvent sufficiently influences the electronic state energies and electronic character of the excited IBr^- chromophore that the excess charge transfers to the I atom. When the CO_2 molecule resides over the waist of the I–Br bond axis or near the I end, then the solvent-induced perturbation is minimal and the dissociation dynamics are similar to those of bare IBr^-. In both the A′- and B-state dissociation dynamics, the MD simulations capture the essence of the charge-transfer mechanism but underestimate the number of trajectories that undergo a state hop. By representing CO_2 more realistically (charge delocalization and bending), the yield for trajectories that hop electronic states would increase. Together, experiment and theory point to a coherent picture for solvent-driven electron transfer by CO_2 in both dissociations.

Chapter V: Photoelectron Spectroscopy of ICN^-

5.1 Motivation for Photoelectron Spectroscopy of ICN^-

Photoelectron spectroscopy is a highly successful technique for measuring intrinsic molecular properties, both thermochemical (such as ionization energies and bond strengths) and spectroscopic (such as electronic-state energies and vibrational frequencies).[8] In addition, negative-ion photoelectron spectroscopy frequently offers a unique advantage: the ability to investigate neutral species in a different molecular geometry than that accessed by conventional absorption spectroscopy.[6,7] In this chapter, we use photoelectron spectroscopy of ICN^- to investigate the ground state and the first five excited electronic states of ICN. Here, too, negative-ion photoelectron spectroscopy yields rich spectroscopic data that were inaccessible to previous studies of neutral ICN.

The primary focus of this work is the ICN A continuum, which appears in direct photoabsorption studies as a broad, unstructured peak extending from 210 nm to ~350 nm,[102] composed of several unresolved excited states with differing dissociation dynamics. The ICN A continuum has been the subject of many investigations, and we direct the reader to an excellent review of the early work on gas-phase ICN by Zare and coworkers.[103] Briefly, exciting the high-energy side of the A continuum (210 – 300 nm) results in two photofragmentation channels, and many state-selective techniques have been used to characterize the dissociation products:[102-108]

$$ICN(^1\Sigma^+) + h\nu\ (4.66\ eV) \rightarrow ICN^* \rightarrow I(^2P_{3/2}) + CN(^2\Sigma^+, \langle E_{rot}\rangle = 0.41\ eV), \qquad \text{Eqn. 5.1}$$

$$ICN(^1\Sigma^+) + h\nu\ (4.66\ eV) \rightarrow ICN^* \rightarrow I^*(^2P_{1/2}) + CN(^2\Sigma^+, \langle E_{rot}\rangle = 0.04\ eV). \qquad \text{Eqn. 5.2}$$

Equation 5.1 is the lower energy dissociation channel and results in ground state I and rotationally excited CN; in contrast, Eqn. 5.2 is higher in energy and yields spin-orbit excited I* and rotationally cold CN. This complex photolytic product distribution suggested non-adiabatic dynamics and stimulated intense interest in the electronic structure of ICN in the energy range of the A continuum and, more specifically, in the evolution of its electronic structure during I–CN dissociation.

The theoretical work of Morokuma and coworkers made a significant contribution to the interpretation of the experimental data on ICN dissociation in the A continuum.[109,110] They performed high-level *ab initio* calculations of the ICN potential energy surfaces and molecular dynamics simulations of A-continuum dissociation. The calculations showed that the A continuum consists of three optically accessible excited states: $^3\Pi_1$, $^3\Pi_{0+}$, and $^1\Pi_1$; two other states ($^3\Pi_2$ and $^3\Pi_{0-}$) are spectroscopically strongly forbidden. Notably, the authors provided high-level calculations of the conical intersection between the $^3\Pi_{0+}$ and $^1\Pi_1$ electronic states.

Despite many dynamics studies that qualitatively substantiate the calculations of Morokuma and coworkers,[102-108,111-120] direct spectroscopic information on the excited electronic states of ICN is still lacking. The spectral congestion and selection rules of ICN absorption spectroscopy preclude isolating the five excited electronic states in this energy region. The only experimental evidence of accessing the dark $^3\Pi_2$ state is from Helbing et al., who studied ICN photodissociation through the A continuum in a matrix.[116] The authors observed emission following ICN dissociation and argued that this emission comes from ICN recombination on the $^3\Pi_2$ state. The $^3\Pi_{0-}$ state has not yet been observed.

Photoelectron spectroscopy of ICN^- provides a different set of selection rules than absorption spectroscopy of ICN; therefore, this technique allows us to characterize the ground state as well as the five excited electronic states that make up the ICN A continuum. Like dihalides, in forming ICN^- the excess electron adds to the antibonding lowest unoccupied molecular orbital (LUMO) of ground state ICN, which weakens and lengthens the I–CN bond. Therefore, by starting at the anion equilibrium geometry, we interrogate the neutral electronic state manifold at an elongated I–C bond length (2.65 Å), compared to that of the ICN ground state (1.99 Å).[121] The bond elongation places the anion in a configuration such that the first three excited states of ICN are resolvable in the anion photoelectron spectrum. Also, this molecular geometry gives the most intense Franck-Condon overlap in the conical intersection region, which comprises the $^3\Pi_{0^+}$ and $^1\Pi_1$ states.

We report the photoelectron spectrum of ICN^- and $ICN^-(Ar)$ in the spectral region of the ICN A continuum. Well-separated peaks yield vertical detachment energies (VDE) for the first three electronic states ($^3\Pi_2$, $^3\Pi_1$, and $^3\Pi_{0^-}$) and the conical intersection region between the $^3\Pi_{0^+}$ and $^1\Pi_1$ states. Recent calculations of the anion and neutral ground- and excited-state potential curves assist in the assignment of the photoelectron spectrum.[122] Additionally, we employ thermochemical cycles to obtain the adiabatic electron affinity, EA(ICN), and the dissociation energy of the anion ground state, $D_0(\tilde{X}\ ^2\Sigma^+\ I–CN^-)$.

5.2 Experimental Methods

A brief summary of our experiment follows and a more thorough description can be found in Chapter II. In order to generate ICN^- or $ICN^-(Ar)$, 15 psig of CO_2 (99.8%, Scott Specialty Gases, Inc.) or 40 psig of Ar (compressed, United States Welding, Inc.) gas passes over

a solid sample of ICN (synthesized according to the procedure of Bak and Hillebert[123]). The ICN^- and $ICN^-(Ar)$ are created and extracted into the anion-laser interaction region with a Wiley-McLaren–Time-of-Flight mass spectrometer. Slightly decreasing both the flux of electrons directed towards the gas expansion and the pulse width of the gas expansion increases the $ICN^-(Ar)$ signal. When optimizing for the Ar-solvated ion, we obtain a 2:1 ratio of ICN^-:$ICN^-(Ar)$. There is no observable difference in the ICN^- photoelectron spectrum for expansion in CO_2 or Ar.

The present experiment requires several different photodetachment wavelengths ranging from 223 to 500 nm. Using the signal output of the OPO directly or doubling the signal frequency in a BBO crystal, we generate the required photodetachment radiation, all with energies of 0.1 – 1 mJ/pulse, and mildly focus it into the anion-laser interaction region. We calibrate and focus the photoelectron spectrometer with the known EA and spin-orbit splitting of the iodine atom by using I^-,[2,55] which is produced in our anion source concurrently with ICN^-. Because of the changing energy resolution, we measure discrete regions of the photoelectron spectrum at varying laser wavelengths and then combine these sections into an overall spectrum.

5.3 ICN and ICN^- Electronic Structure Calculations

To support the assignments of the photoelectron spectrum, we perform a series of ICN and ICN^- electronic structure calculations at the MR-SO-CISD level of theory, using augmented triple-zeta basis sets. The approach is based on earlier work of Morokuma and co-workers;[109,110] the details of the electronic structure calculations as well as the resulting potential energy surfaces for the anion and neutral ground states are presented elsewhere.[122] Two-dimensional surfaces have been calculated for the ground states of ICN and ICN^-, and 1D cuts through the

ICN excited-state potentials in the ICN and INC geometries were obtained at a fixed CN distance of 1.16 Å. The first set of 1D cuts, Fig. 5.1(a), is plotted as a function of the distance between the I and the center of mass of CN, $R(I–CN_{COM})$, and the second set of cuts, Fig. 5.1(b), is a function of the angle between the vector $R(I–CN_{COM})$ and the CN bond, θ, with $R(I–CN_{COM})$ = 3.2 Å. This angle is defined such that the ICN and INC geometries correspond to $\theta = 0°$ and 180°, respectively. The anion ground state curves in Fig. 5.1(a) and 5.1(b) are shifted from the neutral curves by -0.4 eV to obtain better agreement with the measured VDE of the $^3\Pi_2$ and $^3\Pi_1$ transitions.

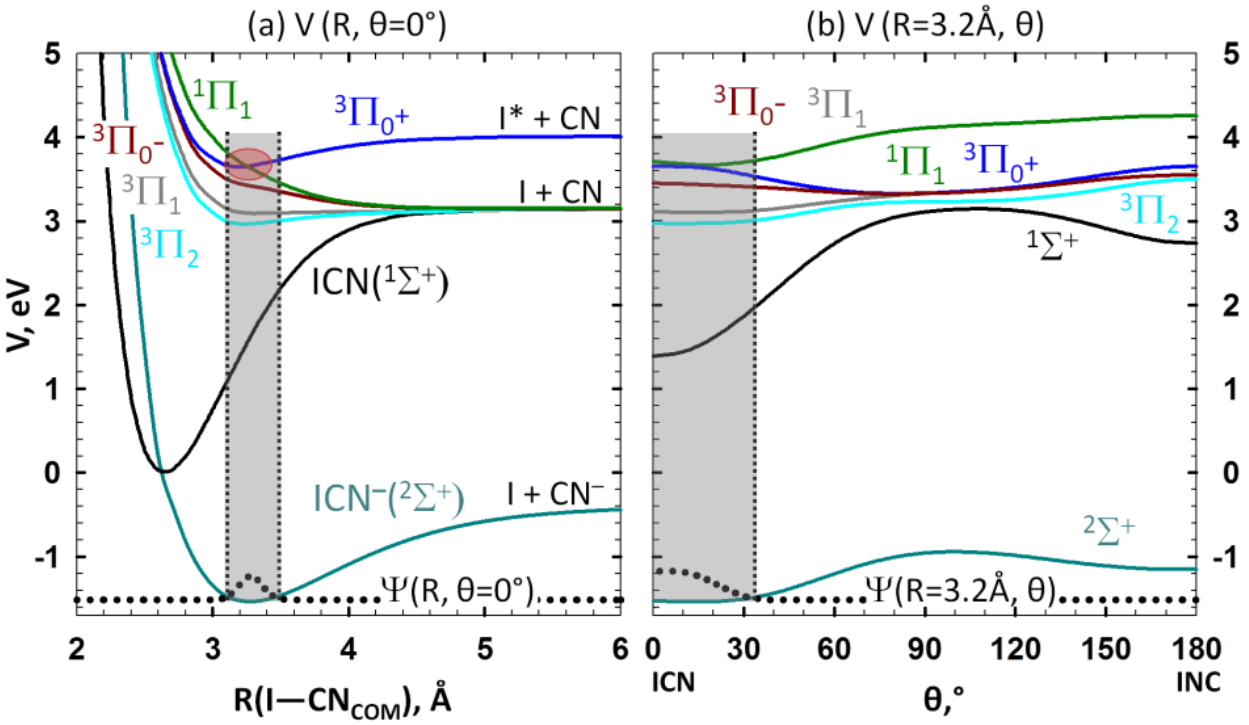

Figure 5.1 (a) Potential energy (V) is plotted as a function of the I to CN center of mass (COM) distance, R(I–CN$_{COM}$), in the linear (θ = 0°) geometry. The red circle highlights the conical intersection region between the $^1\Pi_1$ and $^3\Pi_{0+}$ states. (b) V is plotted as a function of the angle between the R vector and CN axis, θ, for R(I–CN$_{COM}$) = 3.2 Å. In both panels, the ground-state wave function for the anion, Ψ(R, θ), is shown (dotted trace), and the grey box represents the Franck-Condon region. Also, the electronic ground state of the anion has been shifted by -0.4 eV to have better agreement with the measured transitions to the $^3\Pi_2$ and $^3\Pi_1$ states.

As noted in Fig. 5.1(b), the equilibrium structures of both ICN and ICN$^-$ are linear; and as is shown in Fig. 5.1(a), the equilibrium bond distance in the ground electronic state of ICN$^-$ is $R_{e,ICN}$-(I–CN$_{COM}$) = 3.27 Å or, equivalently, an I–C bond distance of 2.65 Å. This is roughly 0.7 Å longer than the corresponding distance in neutral ICN and shows that the photoelectron spectra provide information on portions of the ICN potentials that are not accessible by simple photoabsorption from the ground state of ICN. Based on these surfaces, the I–CN stretch and ICN bend frequencies are 235.2 cm^{-1} and 70.3 cm^{-1}, respectively, and $D_e(\tilde{X}\ ^2\Sigma^+$ I–CN$^-$) is

1.01 eV. Correcting for the zero-point energy, the calculated $D_0(\tilde{X}\ ^2\Sigma^+\ I–CN^–)$ becomes 0.99 eV. Table 5.1 summarizes the calculated equilibrium geometries, dissociation energies, and vibrational frequencies for the ground state of the anion and neutral ICN, along with the first two excited states of ICN, $^3\Pi_2$ and $^3\Pi_1$. This table also provides a comparison between the calculated values and previously measured values for the neutral ground state.

Table 5.1 Calculated spectroscopic properties of $ICN^–$ ($\tilde{X}\ ^2\Sigma^+$) and ICN ($\tilde{X}\ ^1\Sigma^+$, $^3\Pi_2$, and $^3\Pi_1$) from this work, along with previously measured values for ICN ($\tilde{X}\ ^1\Sigma^+$).

		R_e(I–C), Å	D_0(I–CN), eV	$\nu_{I–CNstretch}$, cm^{-1}	ν_{bend}, cm^{-1}
ICN ($^3\Pi_1$)	calc	2.74	0.05	70.5	–
ICN ($^3\Pi_2$)	calc	2.62	0.17	157	–
ICN ($\tilde{X}\ ^1\Sigma^+$)	calc	2.03	3.08	487.6	302
	expt	1.99[a]	3.345[b]	485.8[c]	304.5[c]
$ICN^–$ ($\tilde{X}\ ^2\Sigma^+$)	calc	2.65	0.99	235.2	70.3

a. infrared and microwave spectroscopy[121]

b. high-resolution transient frequency modulated absorption spectroscopy [119]

c. infrared spectroscopy[124,125]

For the present study, we must consider the vibrational properties of the excited states of ICN. This is done by evaluation of the vibrational energies and wave functions based on the 1D cuts that are plotted in Fig. 5.1. In particular, the potential energy curves in Fig. 5.1(a) are interpolated using a cubic spline and stretch states are evaluated in a discrete variable representation.[97] For these calculations, an evenly spaced grid of points is used, which span from 0.3 to 8.0 Å with at least 500 grid points. The wave functions obtained from these 1D cuts are then used to evaluate the 1D Franck-Condon factors for the I–CN stretch between the $\upsilon'' = 0$

electronic ground state and the three lowest-energy bound states of ICN. According to the analysis for the $\tilde{X}\ ^1\Sigma^+$ state, the Franck-Condon factor for the $\upsilon'' = 0 \rightarrow \upsilon' = 0$ transition is essentially zero; instead, there is maximum overlap with the $\upsilon'' = 0 \rightarrow \upsilon' = 29$ transition. For the two excited states, the geometry change compared to the anion electronic ground state is minor; therefore, the 1D Franck-Condon analysis for the $^3\Pi_2$ and $^3\Pi_1$ states results in the $\upsilon'' = 0 \rightarrow \upsilon' =$ 0 transitions being the strongest.

5.4 Results of Photoelectron Spectroscopy of ICN^-

In anion-photoelectron spectroscopy, the photodetachment radiation promptly removes an electron from the initially prepared anion; thus, in the spectra, "vertical" transitions to neutral electronic states dominate without significant changes in the molecular geometry. Therefore, the calculated potential energy curves of ICN^- and ICN provide an initial prediction of the photoelectron spectrum. Figure 5.1(a) and 5.1(b) show the wave function for the anion $\upsilon'' = 0$ ground state, $\Psi(R, \theta)$; in addition, the dotted, vertical lines and grey box highlight the Franck-Condon region, which overlaps spatially with the $^3\Pi_{0^+}$ and $^1\Pi_1$ conical intersection region. Thus, photodetachment of ICN^- will access and provide spectral information on the conical intersection and the lower energy electronic states of ICN near the anion equilibrium geometry.

The portion of the photoelectron spectrum corresponding to the ICN ground electronic state should be a broad envelope, comprising of a long unresolved progression of I–CN vibrational states; the intensity of the vibrational origin transition is likely to be negligible. Conversely, transitions to the first two excited electronic states of ICN, $^3\Pi_2$ and $^3\Pi_1$, should be spectrally narrow with maximum intensity near the origin. The dissociative $^3\Pi_{0^-}$ state should

also be spectrally narrow because the potential energy curve is relatively flat in the Franck-Condon region. Finally, transitions to the states making up the conical intersection should result in a convolution of the spectral feature involving the bound ($^3\Pi_{0^+}$) and dissociative ($^1\Pi_1$) state.

The experimental photoelectron spectrum of ICN^- agrees well with these expectations, as shown in Fig. 5.2. The spectrum is comprised of three segments taken with different photodetachment laser wavelengths (λ = 223, 257, and 259 nm) and over different binding energy ranges. The three spectral regions are scaled relative to each other by using the area under the $^3\Pi_2$ and $^3\Pi_1$ peaks since these transitions yield sharp, well-defined features. The energy ordering of the neutral ICN calculated potential energy curves at $R_{e,ICN}$-(I–CN_{COM}) = 3.27 Å aids in the assignment of the peaks. The very broad envelope with a VDE ≈ 3.2 eV is comprised of multiple, unresolved transitions to vibrational levels of the electronic ground state of neutral ICN ($\tilde{X}\ ^1\Sigma^+$). The other four well-separated peaks are in complete accord with the expectations above and represent the first time that all states within the ICN A continuum have been observed directly. Transitions to the first three excited states of ICN are at a VDE = 4.513 ± 0.003 eV for the $^3\Pi_2$ state, VDE = 4.641 ± 0.003 eV for the $^3\Pi_1$ state, and VDE = 5.025 ± 0.005 eV for the $^3\Pi_{0^-}$ state. The transition to the dissociative $^3\Pi_{0^-}$ state partially overlaps spectrally with the asymmetric peak at a VDE ≈ 5.25 eV, which contains transitions to the $^3\Pi_{0^+}$ and $^1\Pi_1$ electronic states. A comparison with the photoelectron spectra of the dihalides I_2^- and IBr^- further corroborates our photoelectron peak assignments,[17,24,56] and this comparison is shown with the photoelectron spectrum of IBr^- (Fig. 5.2 inset taken from Chapter III).

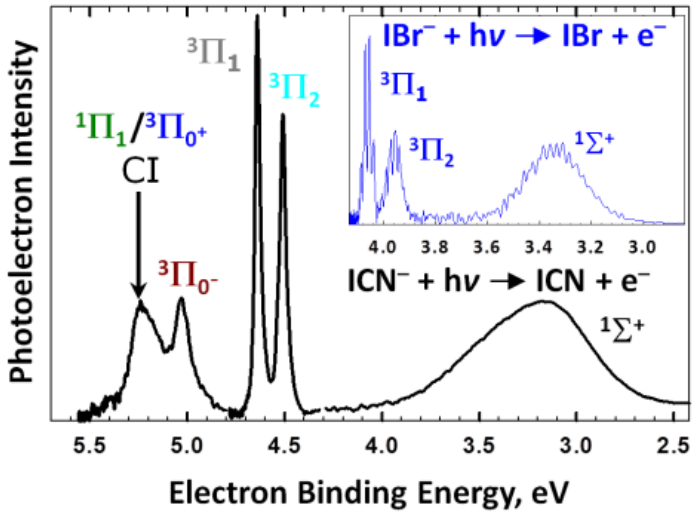

Figure 5.2 Composite photoelectron spectrum of ICN^-. The broad peak at ~ 3.2 eV corresponds to high-lying vibrational levels of the ground electronic state of ICN, $\tilde{X}\ ^1\Sigma^+$. The ground-state origin lies more than 1 eV lower in binding energy and is not observed. The next three sharp features are the first three excited states of ICN ($^3\Pi_2$, $^3\Pi_1$, and $^3\Pi_{0^-}$). The broad asymmetric peak at ~5.25 eV consists of transitions to the conical intersection (CI) region ($^1\Pi_1$ and $^3\Pi_{0^+}$) and has some overlap with the dissociative $^3\Pi_{0^-}$ electronic state. For comparison, the inset shows the photoelectron spectrum of IBr^-.

In the I_2^- and IBr^- photoelectron spectra, bands corresponding to the $^3\Pi_2$ and $^3\Pi_1$ states contain resolved vibrational transitions.[17,24,56] However, the $^3\Pi_2$ and $^3\Pi_1$ transitions in the ICN^- spectrum do not exhibit resolved vibrational structure (black trace in Fig. 5.3). The peaks resulting from transitions to the ICN $^3\Pi_2$ and $^3\Pi_1$ states are significantly wider (42 and 33 meV, respectively) than the experimental resolution (10 meV), indicating unresolved structure. There is a slight shoulder on the higher binding energy side of the $^3\Pi_2$ peak. To reduce possible spectral congestion and resolve vibrational structure within these weakly bound electronic states, we measure the photoelectron spectrum of ICN^-(Ar), which yields a vibrationally colder ICN^-. The ICN^-(Ar) spectrum of the $^3\Pi_2$ and $^3\Pi_1$ region is shown in red in Fig. 5.3: VDE ($^3\Pi_2$) =

4.540 ± 0.005 eV and VDE ($^3\Pi_1$) = 4.672 ± 0.005 eV. The solvated spectrum shifts to higher binding energy by about 30 meV and the peak widths narrow by almost a factor of two. The peak widths of the $^3\Pi_2$ and $^3\Pi_1$ transitions are still somewhat greater (17 and 18 meV, respectively) than the experimental resolution (10 meV); however, the shoulder on the $^3\Pi_2$ peak becomes more prominent in the $ICN^-(Ar)$ spectrum and reinforces our analysis.

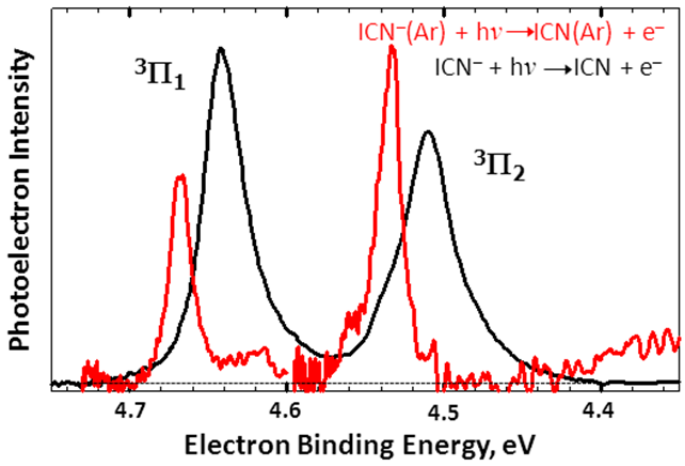

Figure 5.3 Composite photoelectron spectra of ICN^- (black) and $ICN^-(Ar)$ (red) showing transitions to the $^3\Pi_2$ and $^3\Pi_1$ states. Solvation by Ar results in a 30 meV shift to higher binding energy and a sharpening of the peaks for both electronic states. The shoulder on the higher binding energy side of the $^3\Pi_2$ feature becomes more prominent in the $ICN^-(Ar)$ spectrum and lies ~20 meV above the main peak, which is consistent with the calculated I–CN stretch frequency of the $^3\Pi_2$ state.

5.5 Discussion

5.5.1 Photoelectron Spectrum of ICN^-

We further interpret the five peaks in the ICN^- photoelectron spectrum by considering the Franck-Condon overlap between the anion ground state and the neutral states as well as by drawing parallels with the spectra of dihalides.[17,24,56] The shape of the ICN ($^1\Sigma^+$) peak resembles

that of the ground states in the I_2^- and IBr^- spectra, where the peaks are broad and the ground-state origins are not observed. In the spectra of the dihalides, the breadth of the ground state envelope results from a significant change in the I–X, X = I or Br, equilibrium bond distance between the anion and neutral. The large bond elongation occurs because the highest-occupied molecular orbital (HOMO) of the IX^- ground-state electronic configuration is antibonding (σ*). Removing this electron produces the ground electronic state of neutral IX with more bonding character and a shorter I–X bond than in the corresponding anion. When this HOMO electron is detached from the anion, there is minimal Franck-Condon overlap with the origin ($\upsilon' = 0$) and significant overlap with high vibrational levels of the neutral IX ground state. In the I_2^- and IBr^- spectra, the maximum intensity from the ground-state envelope corresponds to ~ 30 quanta in the I–I or I–Br stretch.[24,56] Similarly for ICN, there is a large I–CN bond elongation upon anion formation; therefore, the origin peak is not observable. Based on the 1D cuts through the ICN ground state potential (black curve in Fig. 5.1(a)), the calculated maximum in the Franck-Condon envelope corresponds to the vibrational level with 29 quanta in the I–CN stretch.

The next two higher binding energy peaks in the ICN^- photoelectron spectrum correspond to transitions to the ICN $^3\Pi_2$ and $^3\Pi_1$ electronic states (black trace in Fig. 5.3). For these weakly bound states (our calculations give $D_0(^3\Pi_2$ I–CN) = 170 meV and $D_0(^3\Pi_1$ I–CN) = 50 meV), the flatness of the potential energy curves in the Franck-Condon region and the small change in the I–CN equilibrium bond distance relative to the anion indicates that narrow transitions are expected. Analysis of the Franck-Condon factors for the 1D I–CN stretch for both of these excited states shows that the $\upsilon'' = 0 \rightarrow \upsilon' = 0$ transitions are the strongest; therefore, we equate the difference in the VDE to the term energy splitting between the $^3\Pi_2$ and $^3\Pi_1$ states, ΔT_0

= 0.128 ± 0.008 eV. Combining the measured VDEs with the EA(ICN) yields the term energies of the $^3\Pi_2$ and $^3\Pi_1$ excited states, $T_0(^3\Pi_2\ ICN)$ = 3.16 (+.04/-.02) eV and $T_0(^3\Pi_1\ ICN)$ = 3.29 (+.04/-.02) eV (Table 5.2). The large error bars arise from the uncertainty in the EA(ICN); both the EA(ICN) and corresponding error bars are developed in a later section. The next highest binding energy peak (VDE = 5.025 ± 0.005 eV) in the spectrum is the transition to the dissociative ICN ($^3\Pi_{0-}$) electronic state. As expected, photodetachment of ground state ICN^- to ICN ($^3\Pi_{0-}$) results in a narrow peak.

Table 5.2 Summary of experimentally determined values: dissociation energy (D_0), adiabatic electron affinity (EA), and term energies (T_0).

$D_0(\tilde{X}\ ^2\Sigma^+\ I–CN^-)$	0.83 (+.04/-.02) eV
$EA(\tilde{X}\ ^1\Sigma^+\ ICN)$	1.34_5 (+.04/-.02) eV
$T_0(^3\Pi_2\ ICN)$	3.16 (+.04/-.02) eV
$T_0(^3\Pi_1\ ICN)$	3.29 (+.04/-.02) eV

Finally, the highest binding energy peak occurs at a VDE ≈ 5.25 eV and is composed of transitions to the bound $^3\Pi_{0+}$ and dissociative $^1\Pi_1$ electronic states that form the conical intersection mentioned earlier. This asymmetric peak is the first direct observation of the ICN $^3\Pi_{0+}$ and $^1\Pi_1$ conical intersection region, which is the major determining factor in the product distributions following excitation to the dissociative A continuum. (Note that the feature that results from accessing the conical intersection region also overlaps with transitions to the nearby $^3\Pi_{0-}$ state, which is not a contributor to the conical intersection.) The peak is too broad to determine how each electronic state contributes to the shape. However, the measured VDE agrees very well with the calculated energy of the conical intersection and corroborates the

earlier theoretical work. In addition, our results suggest a potentially useful strategy for future studies of ICN dissociation. By starting from the anion-ground electronic state and using a photodetachment energy of 5.25 eV, it may be possible to prepare a starting ensemble of ICN molecules with a thermal distribution of internal energy close to the conical intersection. Such studies would further test the theoretical framework and give new insights into ICN photodissociation dynamics.

None of the peaks in the photoelectron spectrum of ICN^- contain resolved vibrational structure, which is somewhat surprising considering the analogous spectra of dihalides.[17,24,56] The calculations show little to no change in either the C–N bond length or the ICN angle, θ, between the anion and the three bound electronic states of ICN that we surveyed. Therefore, the I–CN stretch is expected to be the strongest active vibrational mode in the photoelectron spectrum of ICN^-. In a separable model, transitions corresponding to $\Delta\upsilon_{bend} = 0, 2, 4,\ldots$ of the bending mode are also totally symmetric and, therefore, allowed. However, based on a 2D treatment of the vibrations of electronic ground-state ICN, we find more than 100 totally symmetric vibrational levels within a 0.2 eV window centered at the maximum in the Franck-Condon overlap.[122] The >100 vibrational levels resulting from the 2D calculations are in sharp contrast with the five vibrational levels in the same energy range in the 1D calculations, reflecting the large stretch-bend coupling at this high level of vibrational excitation. As a result, the states in this energy region are highly mixed in character. Specifically, of the >100 states in this energy region, roughly half have Franck-Condon intensity that is at least 3% of the most intense transition, and half of these have intensity that is at least one third that of the most intense transition. If hot bands were included in this calculation, the number of transitions that would

contribute to the spectrum would be much larger. It is for this reason that individual vibrations are not spectrally resolved in transitions to the ground state of ICN.

In contrast, the separable model should hold true for the low vibrational levels populated in the $^3\Pi_2$ and $^3\Pi_1$ excited states. Additionally, the calculated I–CN stretch frequencies of the $^3\Pi_2$ and $^3\Pi_1$ states are 19 and 9 meV, respectively. Since, these vibrational frequencies are greater than or comparable to our experimental resolution, we expect to resolve these vibrations. In the photoelectron spectrum of IBr^-, where the I–Br stretch is the only vibrational mode, the $^3\Pi_2$ (18 meV) and $^3\Pi_1$ (17 meV) vibrational progressions of neutral IBr are easily resolved (Fig. 5.2 inset).[24,46,49] Yet, such progressions are not resolved in either of the ICN peaks, suggesting that other contributions are congesting the spectrum.

The potential energy curves shown in Fig. 5.1(b) suggest that the spectral congestion arises from population of the bending modes in the anion. The minimum energy geometry of the anion ground state is linear, but the potential energy does not significantly increase until the bend angle exceeds 30°. This "softness" of the ICN^- bending potential is responsible for the low frequency of the bend vibration, 70.3 cm^{-1} (9 meV), in the anion-electronic ground state (see Table 5.1). In contrast, the I–CN stretching frequency is much higher, 235.2 cm^{-1} (29 meV). The vibrational temperature of the anion source is approximately 150 K, which corresponds to ~ 97% of the ICN^- population being in the first seven quanta of the bend with roughly equal amounts of population in $\upsilon''_{bend} = 0$ and 1 (32% in each). This temperature also results in < 3% of the population in the first excited I–CN stretch state and ~ 0% of the population being in the C–N stretch. In addition, the potential wells in both the $^3\Pi_2$ and $^3\Pi_1$ states are shallow, and the bending potentials are quite loose, which suggests very low frequencies for the excited-state

bends. Therefore, photodetachment from thermally bend-excited anions results in a congested photoelectron spectrum with the bend, stretch, and combination modes active, which yields vibrationally unresolved transitions to the ICN $^3\Pi_2$ and $^3\Pi_1$ states. All of these speculations suggest that additional cooling of the anion, *via* Ar tagging, should be advantageous.

5.5.2 Photoelectron Spectrum of $ICN^-(Ar)$

To reduce the spectral congestion in the photoelectron spectrum of ICN^-, we employ a common technique for ion cooling: argon tagging. Argon typically binds very weakly to anions and thus cools them efficiently by collisions and by evaporation from hot cluster anions.[20,21] The photoelectron spectrum of $ICN^-(Ar)$, shown as the red trace in Fig. 5.3, is similar to the bare ICN^- spectrum except for a shift in the peak position and a reduction in peak width, thus providing evidence that Ar minimally perturbs the anion. The peak shift to slightly higher binding energy, 30 meV, is the difference in solvation energy between the anion and neutral ICN, with the anion being more strongly solvated than the neutral. Assuming that the ICN(Ar) solvation energy is between the binding energy of HCN(Ar) (10 meV) and I_2(Ar) (30 meV), we deduce the $ICN^-(Ar)$ binding energy to be 40 – 60 meV.[126,127] This estimate is consistent with that of $I_2^-(Ar)$ (53 meV) and $I^-(Ar)$ (44 meV).[17,18]

Because of the reduced internal energy of the Ar-solvated anion, the photoelectron spectrum of $ICN^-(Ar)$ is less congested than the bare ICN^- spectrum. The photoelectron peaks corresponding to transitions to the $^3\Pi_2$ and $^3\Pi_1$ states are substantially more narrow (see the red spectrum in Fig. 5.3). The shoulder on the $^3\Pi_2$ transition becomes more prominent, and its position relative to the peak maximum (20 meV) is consistent with the calculated I–CN stretch frequency of the $^3\Pi_2$ state (19 meV). Both the narrowing of the peaks and the prominence of the

shoulder on the $^3\Pi_2$ peak in the Ar-tagged spectrum strongly support our argument that the VDE of the $^3\Pi_2$ and $^3\Pi_1$ states correspond to their origin transitions. Thus, the VDE is directly related to the term energies of the excited states, as given in the previous section. However, the $^3\Pi_2$ and $^3\Pi_1$ transitions are still broader than the experimental resolution. The breadth in the excited state transitions indicates that even though the ICN^- within the Ar cluster is vibrationally colder than the bare species, its population is still not restricted to the $\upsilon'' = 0$ ground state. Also, we cannot discount the additional intermolecular vibrations introduced by the Ar atom, which may broaden the spectrum slightly.

Similarly, the Ar-tagging technique could simplify the spectrum in the conical intersection region. Without Ar tagging, the photoelectron peak corresponding to the conical intersection region is too broad to separate the contributions from transitions to the $^3\Pi_{0^+}$ and $^1\Pi_1$ states and to avoid overlap with the nearby $^3\Pi_{0^-}$ peak. Unfortunately, the high-photon energy required to access the conical intersection region results in too many background photoelectrons, making the signal-to-noise ratio in the Ar-tagged experiments prohibitively low at present.

5.5.3 EA(ICN) and $D_0(\tilde{X}\ ^2\Sigma^+\ I–CN^-)$ Thermochemical Cycles

The large bond length change between the ground electronic states of ICN^- and ICN precludes the observation of the ICN ground-state origin in the photoelectron spectrum and, thus, a direct determination of the electron affinity of ICN. Instead, thermochemical cycles yield both the *EA(ICN)* and the $D_0(\tilde{X}^2\Sigma^+\ I–CN^-)$, shown in Fig. 5.4 and below:

EA(ICN) = 1.34₅ (+.04/-.02) eV =

$$VDE(^3\Pi_1\ ICN) + D_0(^3\Pi_1\ I–CN) - D_0(\tilde{X}^1\Sigma^+\ I–CN)^{119}, \qquad \text{Eqn. 5.3}$$

$D_0(\tilde{X}\,^2\Sigma^+\ I\text{–}CN^-) = 0.83\ (+.04/-.02)\ eV$ =

$$VDE(^3\Pi_1\ ICN\ ) + D_0(^3\Pi_1\ I\text{–}CN) - EA(CN)^{128}. \qquad \text{Eqn. 5.4}$$

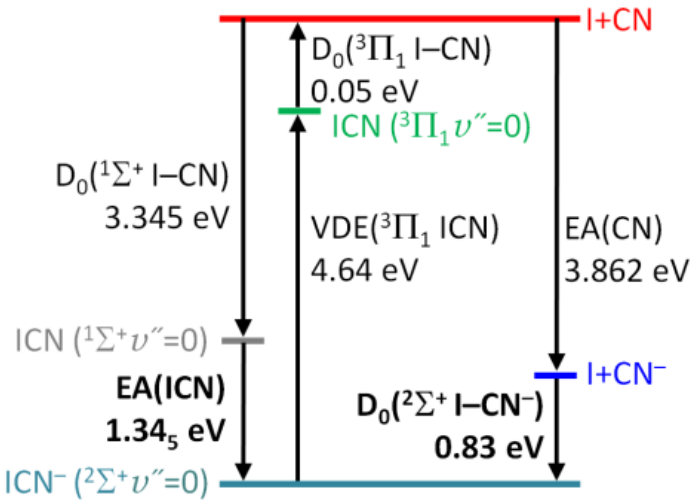

Figure 5.4 Thermochemical cycles used to determine the EA(ICN) and $D_0(\tilde{X}\,^2\Sigma^+\ I\text{–}CN^-)$. The two thermochemical cycles involve either EA(CN)[128] or $D_0(\tilde{X}\,^1\Sigma^+\ I\text{–}CN)$[119] values from previous measurements, along with the measured $VDE(^3\Pi_1\ ICN)$ and calculated $D_0(^3\Pi_1\ I\text{–}CN)$ values from this work.

These cycles include values from literature, $D_0(\tilde{X}\,^1\Sigma^+\ I\text{–}CN) = 3.345$ eV and EA(CN) = 3.862 eV,[119,128] as well as the experimentally measured $VDE(^3\Pi_1\ ICN) = 4.64$ eV and the calculated $D_0(^3\Pi_1\ I\text{–}CN) = 0.05$ eV values. The uncertainty in the calculated well depth propagates through to the EA(ICN) and $D_0(\tilde{X}\,^2\Sigma^+\ I\text{–}CN^-)$ values. As can be seen in Fig. 5.3, the $^3\Pi_1$ well depth must be greater than or equal to the difference between the measured $^3\Pi_1$ origin (center of the $^3\Pi_1$ transitions) and the high-binding energy edge of the $^3\Pi_1$ transitions. This difference conservatively places the lower bound of the well depth at 20 meV. The upper bound

compensates for our uncertainty in the calculated $^3\Pi_1$ well depth, thus, giving an uncertainty of +0.04 eV/-0.02 eV.

This work provides the first determination of the EA(ICN) and $D_0(\tilde{X}\ ^2\Sigma^+ I–CN^-)$, summarized in Table 5.2. The $D_0(\tilde{X}\ ^2\Sigma^+ I–CN^-)$ value is consistent with, but more accurate than, the calculated value of 0.99 eV reported in Table 5.1. A particularly interesting observation is the dramatic I–CN bond weakening that occurs upon electron addition to neutral ICN. This addition changes the I–CN dissociation energy by a factor of four: anion $D_0(\tilde{X}\ ^2\Sigma^+ I–CN^-)$ = 0.83 eV and neutral $D_0(\tilde{X}\ ^1\Sigma^+ I–CN)$ = 3.345 eV.[119] This substantial bond weakening, brought about by the addition of a single antibonding electron, can be rationalized by the strong interaction of the iodine p orbital with the CN σ bonding orbital, which forms a high-energy σ* antibonding LUMO in ICN.[122] This destabilization of the bond caused by the addition of an antibonding electron holds true for both ICN and dihalides, permitting the many comparisons employed in this work. However, the qualitative comparison does not transfer quantitatively to the EA and D_0 due to the σ_{CN} orbital, which is not present in the dihalides, strongly interacting with the p_I orbital.

5.6 Conclusion

We report the photoelectron spectra of ICN^- (and $ICN^-(Ar)$), which provide a characterization of the electronic structure of ICN at an extended I–CN bond length that is not accessible by direct ICN photoabsorption. One advantage of this technique is that the electronic states contained within the well-studied A continuum of ICN are largely resolved, specifically the first three excited electronic states of ICN and the conical intersection region between the

$^3\Pi_{0^+}$ and $^1\Pi_1$ states. In addition, MR-SO-CISD calculations of the potential energy surface of the ICN^- ground state provide benchmark spectroscopic parameters for the anion. Together, the photoelectron spectrum of ICN^- and the results of the calculations allow us to determine the electron affinity of ICN, EA(ICN) = 1.34_5 (+.04/-.02) eV, and the dissociation energy of the anion, $D_0(\tilde{X}^2\Sigma^+ I–CN^-)$ = 0.83 (+.04/-.02) eV. In addition to the reported photoelectron spectrum of ICN^-, we observe low-kinetic energy electrons that do not vary with photon energy over the range from 2.5 to 4.2 eV; the basis for these indirect photodetachment products is discussed in Chapter VI.[27]

Chapter VI: CN Rotation as an Efficient Energy Sink

6.1 Motivation for CN Rotation

The photoelectron spectrum of ICN^- is reported in the previous chapter and demonstrates observed transitions that are anticipated and easily identified. In addition to these direct features, we observe unexpected autodetachment features at low kinetic energy. These features are structured and occur at ~0, ~45, ~70, and ~150 – 200 meV of kinetic energy. When the photon energy is varied from 2.5 – 4.2 eV, the positions of the features do not shift, which is not characteristic of direct detachment. We gain insight into these low-kinetic energy features through additional investigations of the ICN^- excited state ($^2\Pi_{1/2}$) that is isoenergetic with the ICN ground state. More specifically, we turn to publications from our group and collaborators on the photodissociation dynamics and electronic state energies of ICN^-.[27,122,129]

Experimental findings of the ICN^- photodissociation dynamics (λ = 500 nm) on the mostly dissociative $^2\Pi_{1/2}$ state result in primarily I^- + CN. However, photodissociation of ICN^-(Ar) on the $^2\Pi_{1/2}$-like state yields not only I^- but recombined ICN^- as well as I^-(Ar).[27,129] With just one Ar atom solvating the chromophore, one anticipates the results to mimic the bare anion because Ar is such a weakly bound solvent (~40 – 60 meV as discussed in Chapter V). The Ar atom is expected to "boil" off since the photoexcited ICN^-(Ar) has energy in excess of the corresponding I^- + CN + Ar asymptote. Instead, as more Ar atoms are added to the ICN^- chromophore, the recombined and highly solvated I^--based products continue to be observed. These results do not agree with previous studies on small dihalide clusters since we would have expected an evaporative ensemble mechanism to leave the photoproducts bare and the

dissociative nature of the $^2\Pi_{1/2}$ state would only yield photodissociated fragments.[30,43,130] The major difference between the previous dihalide studies and these ICN^- studies is the addition of an extra atom; we now have a triatomic molecule. The extra degrees of freedom in a triatomic molecule provide additional pathways for energy flow. The ICN^- photodissociation results along with calculations determine that the energy sink is CN rotation.

In order to conclude that CN rotation is the major sink for excess energy, we have characterized the $^2\Pi_{1/2}$ surface and propagated the ground-vibrational wave function of ICN^- ($\tilde{X}$) on this first optically active surface ($^2\Pi_{1/2}$).[27,122] The dissociative $^2\Pi_{1/2}$ surface for ICN^- is calculated to have a metastable well depth of ~270 meV at an ICN angle of 24°, where linear ICN corresponds to an angle of 0° and INC corresponds to an angle of 180°. Thus, the preferential geometry is not linear for the $^2\Pi_{1/2}$ state as it is for the ICN^- ground state ($^2\Sigma^+$). Therefore, as linear ICN^- is promoted from the ground electronic state of ICN^- to the $^2\Pi_{1/2}$ state, the excited anion resides on a surface that is preferentially bent and dissociative in nature. At t = 0, the wave function has amplitude that covers ~50° of the ICN bend coordinate, as seen in Fig. 6.1.[27] Within 180 fs, the wave function has not only propagated along the I–CN coordinate but has also quickly spread along the entire ICN bend coordinate, thus making the [I–CN^-] complex, effectively, a free rotor by an I–CN separation of 7 Å. The quantum dynamics calculations result in an abundant amount of energy transfer into CN rotation as ICN^- dissociates.

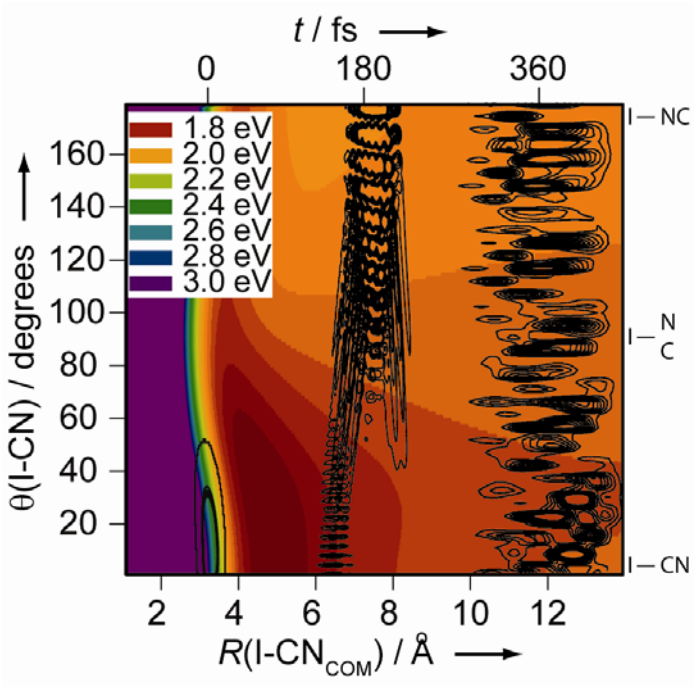

Figure 6.1 The propagated wave function on the $^2\Pi_{1/2}$ surface.[27] The ground-vibrational wave function of $ICN^- \, ^2\Sigma^+$ is promoted to the $^2\Pi_{1/2}$ surface, where the wave function begins to propagate at t = 0. The contour plot shows the wave function at t = 0, 180, and 360 fs. The ICN and INC linear geometries are θ = 0° and 180°, respectively.

This efficient energy transfer explains why the highly solvated I^--based products exist when the $ICN^-(Ar)_n$, n = 1 – 5, dissociates on the $^2\Pi_{1/2}$-like surface and supports one atom caging in the photodissociation of $ICN^-(Ar)$. Since excess energy is being removed by CN rotation, the Ar atom remains bound to the I^- fragment as the ICN^- moiety dissociates. A similar rotational argument holds true for the one atom caging mechanism; however in this case, the Ar atom must be positioned on the CN end of the $ICN^-(Ar)$, thus allowing a collision to occur with the dissociating CN. This collision reverses the direction of the dissociating CN and allows for recombination on the $^2\Pi_{1/2}$ state, where the metastable anion is "trapped" sufficiently long for a radiative transition to the ground state of ICN^-. Without CN rotation, there is too much energy

for the ICN^- to remain in the shallow (~270 meV) well of the $^2\Pi_{1/2}$ state and the "recombined" fragment would just dissociate. A high degree of CN rotation is strongly supported by the bare dissociation quantum dynamics calculations and offers an explanation for the photodissociation dynamics observed.

These photodissociation results show that anisotropy of the $^2\Pi_{1/2}$ surface allows for excess energy to be efficiently coupled into CN rotation. The autodetachment features, which are observed along with the direct detachment signal, appear because ICN^- can store large amounts of energy as CN rotation. In addition to the bare anion exhibiting these autodetachment features, the mechanism for autodetachment is not destroyed by solvation with one Ar atom or CO_2 molecule. As the rest of the chapter will show, these low-kinetic energy features only occur when the photodetachment energy is equivalent to an energy that has Franck-Condon overlap between the ICN^- $^2\Pi_{1/2}$ state and the ICN $^1\Sigma^+$ state.

6.2 Experimental Methods

This experimental section follows almost exactly from the 5.2 Experimental Methods section. Only the additional procedures to those described earlier are mentioned here. To produce the $ICN^-(CO_2)$ anions, 15 psig of CO_2 gas flows over a solid sample of ICN. The ions are created in a similar manner to ICN^- and $ICN^-(Ar)$. To obtain the $ICN^-(CO_2)$ spectra, the $ICN^-(CO_2)$ ion is overlapped with the laser pulse in the anion-laser interaction region. The spectra of low-kinetic energy features are taken over a broad wavelength range: 295 – 500 nm (2.5 – 4.2 eV). These studies require both the 355-nm pumped OPO and the 532-nm pumped dye laser.

To obtain a cross-section measurement of the low-kinetic energy features for ICN^-, it is critical to normalize all of the ICN^- spectra over this broad energy range. Both fluctuations in the laser power and ion intensity need to be considered. The spectra are scaled for the average of the laser power before and after each image and background. To correct for the ion instability, the reported spectra are alternatively taken with a spectrum at 266 nm under the same ion conditions. The 266-nm ICN^- spectrum is similar to the "normal" photoelectron spectrum and contains sharp $^3\Pi_2$ and $^3\Pi_1$ transitions and serves as our reference spectrum. The area under these sharp features is used to correct for ion fluctuations. We correct for short-term ion instability by alternating at least two times between the 266-nm spectrum and the low-kinetic energy spectrum. To highlight the low-kinetic energy features, all the spectra in this chapter are plotted as a function of electron kinetic energy and not the usual electron binding energy.

6.3 Results of Autodetachment from ICN^-, $ICN^-(Ar)$, and $ICN^-(CO_2)$

When ICN^- is photodetached using a 3.7 eV photon, we observe discrete, low-kinetic energy electrons in addition to direct detachment. The low energy peaks do not correspond to any known excited states of ICN and, moreover, do not shift in their kinetic energy as the photon energy is changed. The measured spectrum is shown in Fig. 6.2. The blue box highlights the portion of the spectrum dominated by low-kinetic energy electrons. At higher kinetic energy, the broad ICN ($^1\Sigma^+$) peak dominates the spectrum, which is a result of direct detachment.

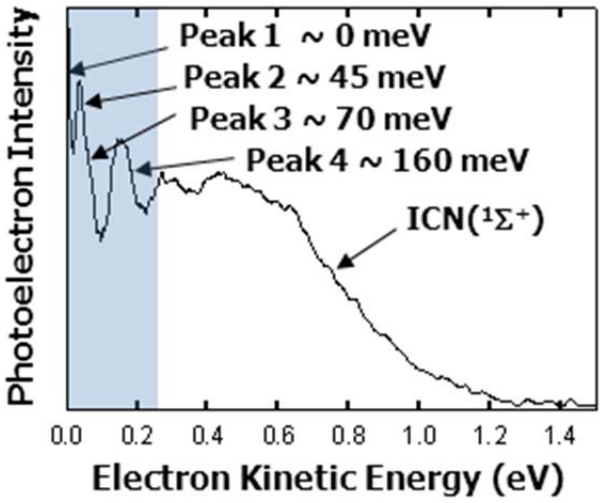

Figure 6.2 Photoelectron spectrum of ICN^- plotted as a function of electron kinetic energy. The spectrum (λ = 335 nm, 3.7 eV) shows low-kinetic energy features on top of a broad background. This background corresponds to the direct photodetachment of ICN^- to the ground state of ICN.

As the photon-energy is varied from 2.5 to 4.2 eV, similar autodetachment features persist, shown in Fig. 6.3. The electron kinetic energy shown in Fig. 6.3(a) is identical to that highlighted by the blue box in Fig. 6.2. The 3.7-eV spectrum shown in Fig. 6.3(a) is the cut identified by the horizontal dashed line in Fig. 6.3(b). The contour plot, Figure 6.3(b), shows the low-kinetic energy features over the first 250 meV of kinetic energy for photon energies ranging from 2.5 to 4.2 eV. In the contour plot, the photodetachment from I^- appears in two of the spectra. This is a result of photofragmentation and is discussed later. As can be seen in Fig. 6.3(c), the low-kinetic energy features have a bimodal distribution peaking at photon energies of 3.7 and 3.25 eV. For these energies, where the cross section is the largest, the structured-electron features extend for approximately 500 meV. However, higher autodetachment features lose intensity when the laser energy varies significantly from 3.7 or 3.25 eV. Therefore we focus on the first four peaks: ~0, ~45, ~70, and ~150 – 200 meV. While the fourth peak (~150 – 200

meV) does have a 50 meV shift in peak position, this shift is rather insignificant given that the laser photon energy is shifted 1.7 eV.

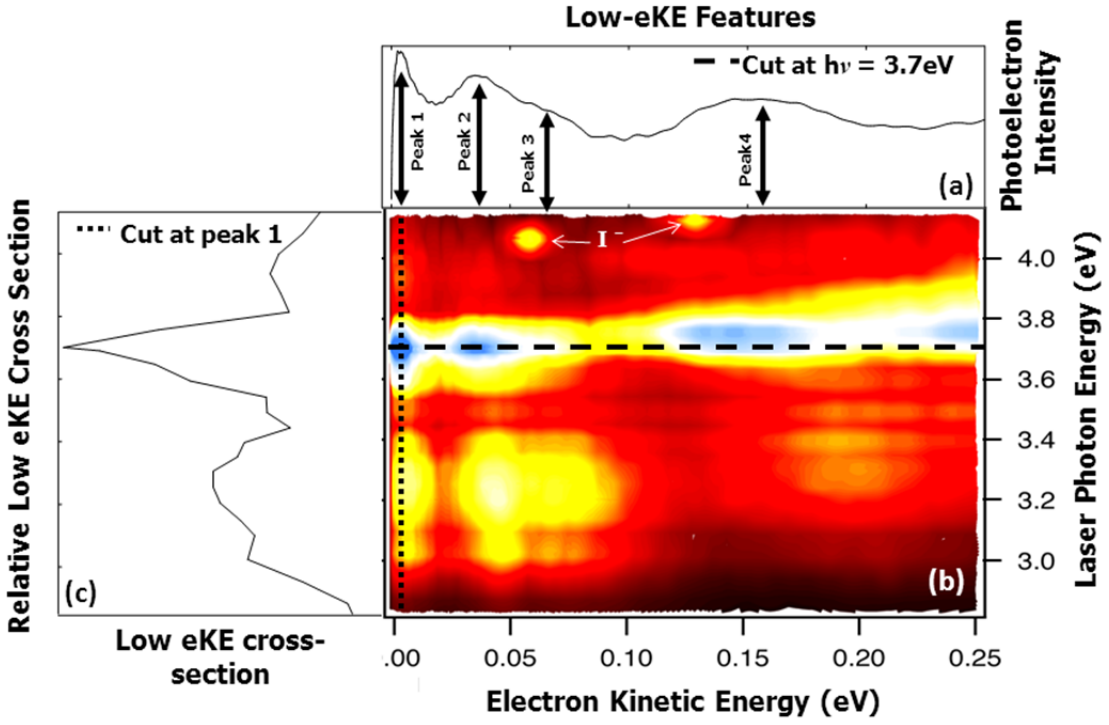

Figure 6.3 Relative cross section of low-kinetic energy features from autodetachment of ICN^-. (a) Photoelectron spectrum of ICN^- (λ = 335 nm, 3.7 eV) as a function of electron kinetic energy. (b) The 3D contour plot of the photoelectron spectrum of ICN^- (λ = 2.6 – 4.1 eV) as a function of electron kinetic energy. The two I^- peaks are a result of ICN^- photofragmentation. (c) Relative cross-section for peak 1 showing at least two maxima at 3.25 and 3.7 eV.

The structured autodetachment features are a result of a one-photon process, which is determined from a power-dependence study. Furthermore, the ejected electrons are isotropic in the image, strongly suggesting that the electrons are the result of an indirect-detachment process.[131] At these laser energies, the ejection of low-kinetic energy electrons is not only in direct competition with direct detachment, but also with photofragmentation:

Autodetachment: $ICN^- + h\nu(2.5 – 4.2\ eV) \rightarrow ICN^{-*} \rightarrow ICN(^1\Sigma^+)^{**} + e^-$ (low-kinetic energy),

Photofragmentation: $ICN^- + h\nu(2.5 – 4.2\ eV) \rightarrow ICN^{-*} \rightarrow I^- + CN$ or $I + CN^-$,

Direct Detachment: $ICN^- + h\nu(2.5 – 4.2\ eV) \rightarrow ICN(^1\Sigma^+)^* + e^-$.

All three processes coexist in our spectra. The autodetachment channel leaves the ICN very hot with internal energies in the range of 1.15 – 2.85 eV; we represent the resulting neutral as ICN**. The excitation energy (2.5 – 4.2 eV) is below the ICN ground state dissociation threshold. As a result, the autodetachment channel must yield ground state ICN in addition to low-kinetic energy electrons. The photofragmentation process can be detected when the photon energy and flux are great enough to both photodissociate ICN^- and photodetach the electron from one of the photofragments, I^- (3.06 eV) or CN^- (3.86 eV).[55,128] The photodetachment from I^- is observed in Fig. 6.3 and is identified. The I^- peak indicates how the spectral features should shift with photon energy if the features are photon-energy dependent. Finally, the direct detachment channel results in the broad feature lying at higher kinetic energies, as is shown in Fig. 6.2.

The ICN^- autodetachment features observed in Fig. 6.2 and 6.3 are also present when Ar or CO_2 solvates ICN^-. As is shown in Fig. 6.4, there is remarkable similarity between the autodetachment peaks in the bare and solvated spectra. At high electron kinetic energies, there is a broad background, which is the ground state of ICN, ICN(Ar), or ICN(CO_2). In addition to the broad background, the sharp features in the solvated spectra and the bump in the bare spectrum around 0.7 eV result from I^- photodetachment. At low electron kinetic energies, the first three peaks in the ICN^-(Ar) and ICN^-(CO_2) do not shift compared to the bare spectrum. However, the fourth peak does have some minimal shifting, which is most likely related to the shift that was

seen in Fig. 6.3(b). Overall, the presence of the Ar or CO_2 solvent minimally perturbs the chromophore and does not affect the mechanism by which ICN^- autodetachment occurs.

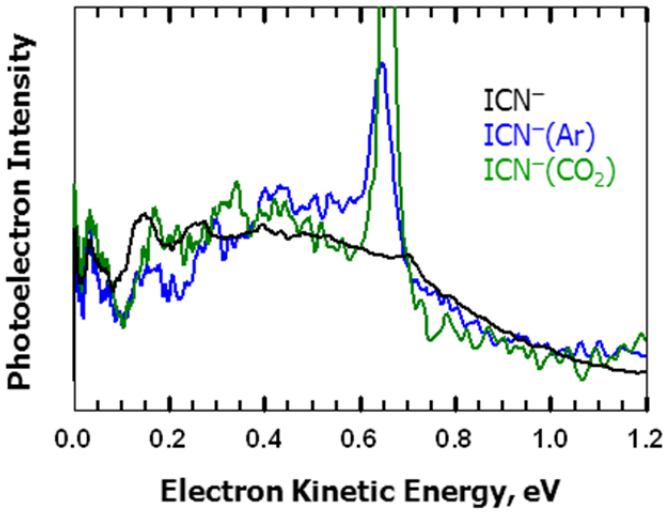

Figure 6.4 Photoelectron spectrum of ICN^- (black), $ICN^-(Ar)$ (blue trace), and $ICN^-(CO_2)$ (green trace) plotted as a function of electron kinetic energy. The spectrum (λ = 330 nm, 3.8 eV) shows low-kinetic energy features on top of a broad background. This background corresponds to the direct photodetachment of ICN^- to the ground state of ICN. The sharp feature (or bump) near 0.7 eV in the blue and green trace (or black trace) results from the photodetachment of I^-.

6.5 Discussion of Autodetachment Features

To better understand the low-kinetic energy features and bimodal cross-section, we look to previous studies of anionic autodetachment, where either a statistical model (thermionic emission) and/or a quantum model is used to explain the autodetachment features. In a statistical model, the density of states is sufficiently high to allow for a fast redistribution of energy before ejecting the electron, such as in C_{18}^- and $(OCS)_2^-$. [132-134] In these examples, the ejected electrons are statistically spread over a broad kinetic energy range and are fairly independent of the photon

energy used. A purely statistical model cannot be used to explain the ICN^- autodetachment mechanism because the low-kinetic energy features are structured.

Another type of autodetachment observed by Continetti and coworkers as well as Sanov and coworkers results in discrete, low-kinetic energy features.[131,135] Continetti and coworkers observed autodetachment features from O_{2n}^- clusters (n = 2 and 3) when using different excitation energies (λ = 532 and 355 nm).[135] In this work, dissociation to form O_2^- is energetically accessible. In some of the photodissociated clusters, the O_2^- is vibrationally hot ($\upsilon'' > 4$) and exceeds the energy of O_2 ($\upsilon' = 0$) + e^-, leading to autodetachment. These autodetachment features are at discrete energies that are consistent with the spacing of O_2^- ($\upsilon'' = 5, 6, 7$) → O_2 ($\upsilon' = 0$) + e^-, and the position of the features are independent of the cluster size or photon energy used. The O_{2n}^- cluster dissociates to vibrationally hot O_2^- ($\upsilon'' = 5, 6, 7$) and the excess energy is removed by the other fragments. Similarly, Sanov and coworkers measure autodetachment features from photoexcited (λ = 355nm) $O_{2n}^-(H_2O)_m$ clusters when the photodissociated O_2^- exceeds ($\upsilon'' > 3$).[131] In this study, the autodetachment features are the same as those measured by Continetti and coworkers, where again the features are at discrete energies and independent of the cluster size.

Another example of autodetachment leading to discrete, low-kinetic energy features was observed by Wang and coworkers following a photoelectron spectroscopy study of doubly charged anions, $^-O_2C(CH_2)_nCO_2^-$.[136] The photodetachment of an electron led to decarboxylation of the anion to yield $^\bullet(CH_2)_nCO_2^-$; this singly charged anion then underwent a dissociative autodetachment process [$(CH_2)_n + CO_2 + e^-$] or a hydrogen-transfer-induced electron detachment [$CH_2{=}CH(CH_2)_{n-2}CO_2H + e^-$] to produce the autodetachment features. The autodetachment

features do not shift in kinetic energy as the photon energy is changed. For n = 2, the authors argue that the dominant pathway is the dissociative autodetachment process and the excess energy is removed by the vibrational modes that are not relevant to the reaction coordinate. The quantum model used to explain the O_{2n}^- clusters and $^-O_2C(CH_2)_nCO_2^-$ autodetachment features cannot be exactly used to explain the ICN^- autodetachment mechanism because the neutral ICN molecule following electron photodetachment is energetically excited but below the I + CN + e^- dissociation energy. However, the concept of disposing of excess energy into other degrees of freedom can be used to explain the ICN^- autodetachment mechanism.

We use these previous autodetachment results along with the knowledge that CN has the capability of storing ample amounts of energy in CN rotation to propose a quasi-thermionic emission mechanism for autodetachment.[27] The ICN^- excitation energies that lead to autodetachment are similar to the energies used in the photodissociation of ICN^-, where the ICN^- dissociates on the $^2\Pi_{1/2}$ surface. As mentioned earlier, this $^2\Pi_{1/2}$ excited state is energetically close to the ground state of ICN at certain geometries. Figure 6.5 contains the calculated potential energy curves of ground state ICN ($\tilde{X}\,^1\Sigma^+$) (black trace) as well as the ground state ($\tilde{X}\,^2\Sigma^+$) (dark cyan trace) and first optically active state ($^2\Pi_{1/2}$) (green trace) of ICN^-. These curves are plotted as a function of the I to CN center of mass (COM) distance. The corresponding I–NC curves are plotted as a dashed curve. The red box highlights the range of photon energies that create the low kinetic energy electrons. Again, these energies are below the ICN asymptote but high enough to access the neutral ICN ground state. Additionally, most of the energies allow for the formation of both ICN and INC.

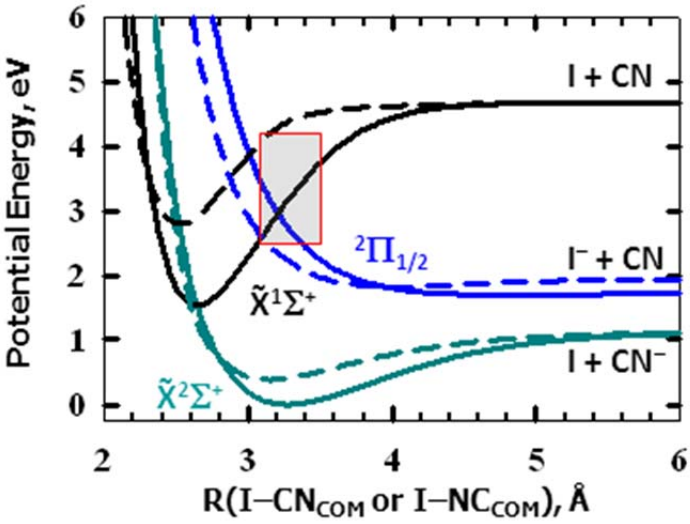

Figure 6.5 Some of the potential energy curves for ICN^- and ICN are plotted as a function of the I to CN center of mass (COM) distance, R(I–CN_{COM}), in the linear (θ = 0 and 180°) geometries. The solid curves indicate the I–CN_{COM} (θ = 0°) geometry, and the dashed curves indicate the I–NC_{COM} (θ = 180°). The red box highlights the region where autodetachment occurs.

Since the neutral molecule cannot dissociate, the triatomic must retain the excess energy, which is between 1.15 and 2.85 eV of internal energy. The autodetachment features along with the ICN^- photodissociation results strongly suggest that the ICN^- is being excited into the optically active (or "bright") $^2\Pi_{1/2}$ state where it then couples to a "dark" state. This "dark" state of the anion must have a high density of states, which allows it to act as its own heat bath. The only way to obtain a sufficient density of states is for the CN entity to be rotationally hot, where it can act as a hindered or free rotor interacting with I^-. It is from this bath-like molecule that the quasi-thermionic emission occurs to the ICN ground state, leaving the neutral molecule very hot. This proposed mechanism is reminiscent of the cluster and $^-O_2C(CH_2)_nCO_2^-$ studies because the extra energy is being deposited into the rotation of the CN, which is efficiently disposing of excess energy in discrete rotational energies. Since the potential energy surface of the "dark"

state is not known, coupling to the neutral ground state is not understood from a quantum view and the features cannot be assigned at this time.

This autodetachment process must occur with some time delay since it is an indirect process that allows for energy to be redistributed throughout the molecule.[137] This process violates the Born-Oppenheimer approximation to produce low-kinetic energy electrons with hot neutral counterparts. The bimodal cross section suggests that there are either two "bright" states or two "dark" states that couple with the "bright" state. In either explanation, the rotation of the CN is vital for disposing of excess energy and allowing coupling between the excited anionic state and the neutral ground state. With the addition of solvent, Ar or CO_2, the mechanism for the autodetachment features is not disrupted.

6.5 Conclusion

In additional to direct photodetachment of ICN^-, we observe autodetachment features at discrete energies (~0, ~45, ~70, and ~150 – 200 meV) over a 1.7 eV excitation range. These autodetachment features are due to the ability of CN rotation to sequester large amounts of internal energy in photoexcited ICN^-. The ICN^- acts as its own heat bath to eject quasi-thermal electrons to produce neutral ICN, in which the CN can behave as a hindered or free rotor. This quasi-thermionic emission of electrons is still present when an Ar atom or CO_2 molecule solvates the ICN^-. The role that CN rotation plays in both the quasi-thermionic emission mechanism and the ICN^- photodissociation is critical to explain the observed results.

Chapter VII: HO_3^- and Future Projects

7.1 Motivation for HO_3^-

The OH radical is the most common atmospheric oxidizer and plays a role in the distribution and concentration of greenhouse gases and other pollutants.[138,139] Therefore, there is a large effort by the scientific community to accurately measure the OH radical concentration. In addition to the pure OH radical concentration, it is essential to know if the OH radical can be temporarily trapped or form an intermediate species with other molecules, such as molecular oxygen (O_2), nitric acid ($HONO_2$), and nitrogen dioxide (NO_2).[140] The association reaction of OH radical with O_2 yields hydrogen trioxy radical (HO–OO). HO_3 has attracted considerable attention because of its potential role as an atmospheric sink of the OH radical and intermediate in atmospheric reactions. Depending on the HO–OO bond strength, the HO_3 radical may trap the OH radical, which would affect kinetic modeling of atmospheric processes.

To date, there is disagreement regarding the bond strength of HO–OO and the relevance that it has in the atmosphere. Recent experiments by Lester and coworkers have resulted in an upper bound to the dissociation energy of trans-HO–OO, D_0(trans-HO–OO) < 5.3 kcal/mol (0.23 eV).[140] This upper bound is inferred from infrared action spectroscopy using an IR-UV double resonance technique where laser induced fluorescence is detected from dissociated OH radicals. Because the D_0(HO–OO) estimate is determined by conservation of energy and the energy partitioned to the O_2 is argued to be small, they suggest that the dissociation energy is close to their upper bound. Using a D_0(trans-HO–OO) = 5.3 kcal/mol, Lester and coworkers argue that 25% of the OH radical is being trapped by O_2 near the tropopause.

Experimental results from Sims and coworkers conclude that the D_0(HO–OO) is below the upper bound determined by Lester and coworkers but not close to the upper bound as suggested by Lester and coworkers. Instead, the kinetics measurements by Sims and coworkers result in D_0(HO–OO) = 3 kcal/mol (0.13 eV); thus, the percentage of OH radical bound to the O_2 would be less than 0.1% at all altitudes in the atmosphere.[141] Their experiments measure the decay of the OH radical in the presence of O_2 by detecting laser induced fluorescence of the OH radical in a fast flow reactor. However, it is not clear from Sims and coworkers studies that the results are due to HO_3 but could be a result of the Van der Waals complex, OH---O_2, or the cis isomer. To add to the D_0 inconsistency, earlier calculations by Stanton and coworkers suggest a possible barrier to the OH + O_2 association reaction, which could complicate the interpretation of the Sims experimental results.[142] However, Stanton is not confident in the calculated barrier height and suggests that the calculated barrier is too large.[143] These experimental and theoretical results strongly suggest that other approaches are needed to determine the HO–OO dissociation energy, which is still an atmospherically important value and not yet resolved.

The photoelectron spectrum of HO_3^- could help settle the debate over the binding energy of the HO–OO molecule. The principal difference between the HO_3^- anion and the HO_3 neutral molecule is the significant lengthening of the central O–O bond in the anion compared to the neutral molecule; therefore, the photoelectron spectrum is expected to be dominated by the vibrational progression of the central O–O stretching mode.[143,144] If the HO–OO vibrational progression within neutral HO_3 can be resolved, then the vibrational levels can be mapped out and the dissociation energy determined.

In addition to requiring the vibrational resolution, there are at least three more difficulties that must be overcome before the dissociation energy of HO–OO can be determined from negative-ion photoelectron spectroscopy. First, the anion needs to be made in our anion-source chamber. Second, the anion that will most likely be made is the cis isomer because the trans isomer is not predicted to be stable.[143,144] For neutral HO_3, the trans isomer is calculated to be lower in energy than the cis form by ~70 cm^{-1} (0.2 kcal/mol).[145] Therefore, if the $D_0(cis\text{-}HO_3)$ can be determined with photoelectron spectroscopy of cis-HO_3^-, then the calculated change in energy ($\Delta E = 0.02$ *kcal/mol*) between the cis- and trans-HO_3 isomers can be used to determine the $D_0(trans\text{-}HO_3)$:

$$D_0(trans\text{-}HO_3) = D_0(cis\text{-}HO_3) + \Delta E. \qquad \text{Eqn. 7.1}$$

Third, other vibrational modes (e.g., stretching of the terminal bonds or bending motions) may be active, which could lead to further congestion of the spectrum, and a full simulation is needed to determine the extent of contributions from other vibrational modes.

In the remainder of this chapter, the cis-HO_3^- isomer is discussed along with its isomers. The current photoelectron spectrum is presented, which is most likely not from cis-HO_3^- but from another isomer. Our initial attempts for making HO_3^- continue to give the same photoelectron spectrum, which does not contain photodetachment signal from cis-HO_3^-. These attempts include a variety of mixtures and combinations of precursor gases where the gas pulse is ionized by a beam of electrons and/or a pulsed electrical discharge. The chapter then proceeds to discuss improvements and modifications made to the anion source, which are incorporated in an attempt to make the cis-HO_3^- anion. Even though these changes have yet to generate the cis-

HO_3^- anion successfully, the additions to the anion source capabilities will benefit future chemical syntheses.

7.2 Current Results and Experimental Difficulties in Making HO_3^-

7.2.1 Expected Photoelectron Spectrum of cis-HO_3^-

The expectations for the HO_3^- photoelectron spectrum are presented prior to showing the measured spectrum. The predicted spectrum is based upon changes in the equilibrium geometries between the anion HO_3^- and neutral HO_3. The calculated equilibrium structures (CCSD(T)/aug-pVTZ) of HO_3^- and HO_3 radical are shown for the cis and trans isomers in Fig. 7.1.[144] The specific energies for these isomers vary depending on the level of theory used, and these structures should only be used qualitatively.[144,146] According to the HO_3^- calculations, the trans isomer of the anion is a transition state and does not have a local minimum; therefore, we expect to make only the cis isomer of HO_3^-. The largest geometry difference between the anion and neutral cis isomer is the central O–O bond distance, $\Delta R(O–O) = 0.17$ Å. There are some minor changes in the terminal O–O bond length and HOO angle. Overall, the dominant peaks in the photoelectron spectrum of cis-HO_3^- should arise from the central O–O stretching progression.

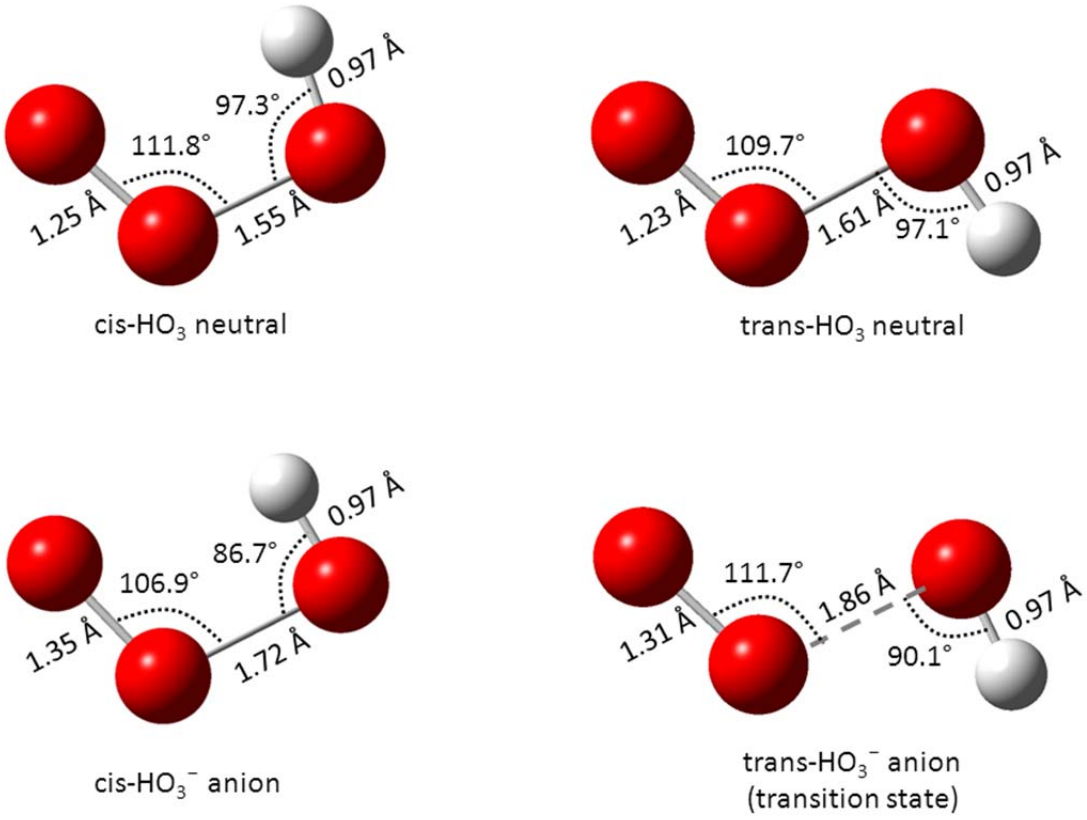

Figure 7.1 Calculated cis- and trans-HO_3 structures for the anion and radical species. These calculations are performed with CCSD(T)/aug-pVTZ level of theory.[144]

The cis-HO_3^- isomer is not the global minimum because OH^- solvated by O_2 ($^3\Sigma$) is lower in energy.[147] Figure 7.2 depicts the qualitative potential energy curves for HO_3^-, $OH^-(O_2)$, and neutral HO_3. These curves are based upon calculations and experimental values. The $OH^-(O_2)$ asymptote is 22.6 kcal/mol (0.98 eV) lower in energy than the cis-HO_3^- asymptote.[148] The $OH^-(O_2)$ cluster anion is calculated to have a $D_0(OH^- – O_2)$ of 2.7 kcal/mol (0.117 eV), and the cis-HO_3^- isomer is calculated to have a well depth of 15.4 kcal/mol (0.67 eV).[147] If the $OH^-(O_2)$ cluster anion is photodetached, it will have a photoelectron peak that resembles photodetachment from the ground state of OH^- ($^1\Sigma$) (1.83 eV) but shifted to a higher binding

energy, which is determined by the difference in the O_2 solvation energy between the anion and neutral species.[149,150] Based upon the energetics in Fig. 7.2, the electron affinity of cis-HO_3 is estimated to be between 1.0 and 1.5 eV. Therefore, to learn about the central O–O stretch and, consequently, the HO–OO dissociation energy, the photoelectron spectrum of cis-HO_3^- must be measured with a photon energy in the 1.5 – 2 eV range. The cis-HO_3^- photoelectron signal should be readily distinguishable from the $OH^-(O_2)$ photoelectron signal.

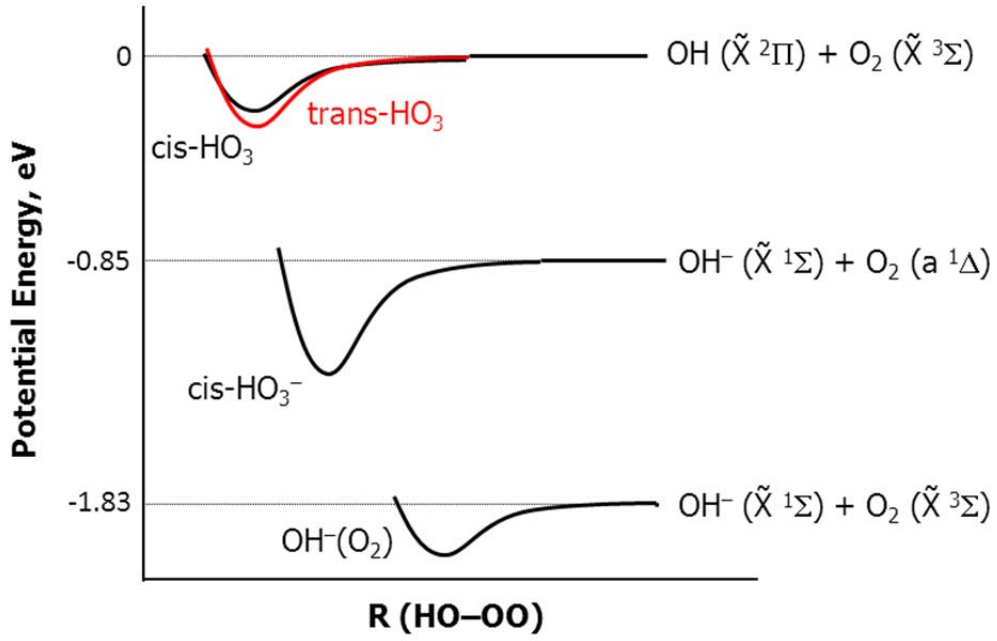

Figure 7.2 Qualitative potential energy curves for cis- and trans-HO_3, cis- HO_3^-, and $OH^-(O_2)$.

7.2.2 Current Results

Two photoelectron spectra of an ion of mass-to-charge ratio 49 are shown in Fig. 7.3 and are plotted as a function of electron binding energy (eBE). The figure shows two photoelectron spectra taken at different wavelengths of laser light, λ = 532 nm (red spectra) and 355 nm (blue

spectra). Both spectra show a dominant peak at an eBE of ~1.95 eV, which results from the $OH^-(O_2)$ complex; this peak is shifted by +120 meV from bare OH^-. The three other peaks, which are highlighted by arrows in Fig. 7.3, are only observed in the 532-nm spectrum and are reproducible when taking the spectrum with a laser wavelength of 532 nm. The assignments for these peaks are tentative and further studies must be performed to verify their origins. The peaks at an eBE of ~1.46 and ~1.83 eV are most likely from two-photon detachment of O^- and OH^-, respectively. The spectral peak at an eBE of ~2.25 eV could be due to O_3^- (mass 48) contaminant or from the branched-$[O–O(H)–O]^-$ isomer, where the H is bonded to the central oxygen. This branched structure is considered as a possibility because the branched anion is calculated to be stable, which will be discussed later. The photoelectron spectrum of pure O_3^- (mass 48) taken with $\lambda = 532$ nm does have intensity near 2.25 eV and two-photon detachment signal of O^- at an eBE of 1.46 eV. For the 532-nm spectrum of mass-to-charge ratio 49, the ~1.46 eV peak does change with laser power; however, it is not clear from the initial measurements how the ~1.83 and ~2.25 eV peaks depend on the laser power. The peak at an eBE of ~ 1.46 eV could not be positively identified as O^- photodetachment because of the resolution at eBE = 1.46 eV when using 532-nm radiation.

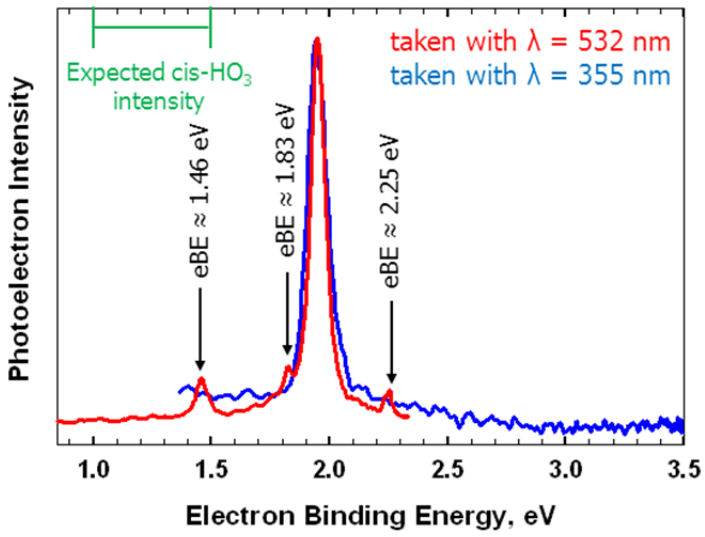

Figure 7.3 Photoelectron spectra for an anion of mass-to-charge ratio 49. Two spectra are taken with different photon wavelengths, where λ = 532 nm is shown in red and λ = 355 nm is shown in blue. The large peak at an eBE of ~1.95 eV is from $OH^-(O_2)$. The other spectral peaks in the 532-nm spectrum are not definitively assigned at this time.

The spectral peaks that disappear when the spectrum is taken with λ = 355 nm are puzzling. If the ~1.83 eV peak is present in the λ = 355 nm spectrum, then it is likely obscured due to the decrease in the experimental resolution at eBE = 1.83 eV. However, this spectral peak is assigned to the $OH^-(O_2)$ complex where the complex photodissociates to OH^- and O_2, and a second photon photodetaches the electron from OH^-. The likely reason for the disappearance of the ~1.46 and ~2.25 eV peaks when the photodetachment energy changes is that they are also a result of a multiphoton process. However, it is not obvious what parent anion(s) contributes to these two peaks, and two possibilities are O_3^- and/or branched-$[O–O(H)–O]^-$. The O_3^- contaminant seems unlikely since the ratio of intensities between the mass-to charge ratio 48 and 49 changes in the mass spectrum as the anion source is varied, but the spectral peaks in the 532-

nm spectrum do not change intensity as the anion source is changed. Therefore, the multiphoton species are more likely from the branched-$[O–O(H)–O]^-$ isomer than from O_3^-.

According to calculations (CCSD(T) at MP2 geometries) by Anne McCoy, the branched-$[O–O(H)–O]^-$ isomer lies 0.83 eV higher in energy than the cis-HO_3^- isomer.[146] The weakest bond in this structure is the O–O bond ($D_0[O–O(H)O]^- = 0.99$ eV), which could photodissociate to O^- and HO_2. Subsequent photodetachment from O^- would give a peak at an eBE of 1.46 eV. Also, the H–O bond could break ($D_0[OO–(H)O]^- = 1.67$ eV). Breaking the H–O bond gives O_3^- and H atom, leading to the spectral peak at an eBE of ~2.25 eV. However, the analysis becomes more complicated because McCoy predicts the branched-$[O–O(H)–O]^-$ isomer to have a vertical detachment energy of ~3.24 eV and an electron affinity of 2.86 eV, which we did not observe.[146] Therefore, more data are required to determine if the branched-$[O–O(H)–O]^-$ isomer is present and contributing to the multiphoton peaks in the 532-nm spectrum. The absence of direct photodetachment of the branched-$[O–O(H)–O]^-$ isomer in the 355-nm spectrum suggests that this isomer might not be the parent anion contributing to the smaller peaks in Fig.7.3.

7.2.3 Variations to the Ion Source

As mentioned earlier, the anion source is greatly varied (both the ionization technique and mixture of gases) in an attempt to change the 532-nm spectrum, and the 532-nm spectrum in Fig.7.3 is invariant to changes in the anion conditions. In the initial approach, two techniques are used to ionize the gas pulse. The first is with a continuous beam of electrons generated from an electron gun. This is the ionization technique described in Chapter II and used in the other experimental chapters. A second technique is using a pulsed, electrical discharge source. The discharge occurs when gas flows between a pulsed, high voltage electrode and a grounded

electrode. A high voltage pulser supplies the pulsed voltage (~ -1000 V) to one electrode. To stabilize the discharge pulse, resistors (10 – 20 kΩ) are placed between the high voltage pulser and the charged electrode.[151] We have also found that a small, continuous current of electrons (~50 μA) generated by the electron gun helps to stabilize the discharge and increase the ion production when using the pulsed discharge as the main ionization source.

There are various setups for creating a pulsed discharge source, which involve one electrode being grounded and the other electrode being pulsed at a negative or positive voltage. For these experiments, the following three setups have been tried. The first pulsed discharge setup consists of two pins at 180° with 1 to 2 mm between the pins. One pin is held at ground and the other pin is pulsed to high voltage. These pins are made of stainless steel and held in place by a Teflon ring that is attached to the General Valve faceplate. This technique produces a steady pulse of ions; however, the ion intensity is low. The second setup involves having a long (2 cm), narrow channel (~1 or 2 mm inner diameter) attached to the faceplate with a cone on the other end. Inside the channel two pins produce the pulsed discharge; however, this second method is very unstable because the narrow channel becomes dirty and charges up. A third setup is to have rings with a ~1 mm inner diameter stacked onto the General Valve faceplate. The stainless steel plates are insulated from each other with Teflon rings and again one plate is grounded while the other is pulsed to high voltage. This third setup is usually used for the pulsed discharge source because it produces the most intense and stable ions.

Both the continuous beam of electrons and pulsed discharge techniques are used to ionize different mixtures of gases. All the mixtures of gases are expanded through the General Valve at various backing pressures (5 – 60 psig) and stem from previous experiments on HOOO or

HOOOH, where HO_3 and a slow electron could combine in a three-body collision or OH^- could combine with O_2 in a three-body collision.[152-155] At first, we flowed pure Ar or ~0.1 – 98% O_2 with Ar over $H_2O_2(l)$. The vapor pressure of H_2O_2 is high enough to be mixed with Ar. However, we must be careful about surfaces. H_2O_2 is very corrosive to Buna o-rings. Therefore, the Buna o-rings are replaced with Kalrez o-rings when H_2O_2 is being used; otherwise, carbon clusters will form in the anion source. We also tried flowing a mixture of ~0.1 – 98% O_2 in Ar/He over H_2O (+20°C – -10°C), where the ratio of the Ar and He are varied, and this strategy was also not successful. In addition, mixtures of $O_2/H_2/Ar$ were used in an attempt to produce cis-HO_3^- but this ion was not generated. Lastly we used combinations of $CH_4/N_2O/Ar$; unfortunately, the $OH^-(CH_4)_2$ cluster also resides at mass-to-charge ratio 49, which produces a strong background signal. Many combinations of different gases were used in varying concentrations in an attempt to produce the cis-HO_3^- isomer; however, all of the variations to the ion source resulted in the same 532-nm spectrum as shown in Fig. 7.3.

7.3 Improvements/Changes to Anion Source

From these initial experiments, we learned that our current approaches do not generate the cis-HO_3^- isomer. According to Fig. 7.2, the dissociation limit for the cis-HO_3^- isomer corresponds to OH^- and O_2 ($a\ ^1\Delta$). If the cis-HO_3^- anions are to be made by collisions between OH^- and O_2, then the O_2 molecule must be in the metastable $a\ ^1\Delta$ state. This cis-HO_3^- complex also needs to be stabilized before it dissociates because the density of the expansion is too low to stabilize the cis-HO_3^- complex. Therefore, the OH^- should be solvated by Ar, such that the Ar can be evaporated following collisions with O_2 ($a\ ^1\Delta$) to stabilize the newly formed complex:

$$OH^-(Ar)_n + O_2\ (a\ ^1\Delta) \rightarrow \text{cis-}HO_3^- + nAr. \qquad \text{Eqn. 7.2}$$

In order to generate the Ar tagged OH^- and the excited state of O_2, some modifications must be made to the anion source. The formation of $OH^-(Ar)_n$ depends critically on the gas expansion characteristics, which can be changed by increasing/decreasing the General Valve tension. Also, by modifying the anion source to mix gases in real time, the composition of the gas expansion can be adjusted "on the fly", which eliminates the need to make the gas mixtures in advance and allows for incompatible gases to interact in the vacuum chamber. Both of these modifications to the anion source will be addressed first. The second improvement to the anion source is then discussed, which introduces a chemical-based method for making O_2 ($a\ ^1\Delta$) and injecting the excited state O_2 after the formation of the $OH^-(Ar)_n$ clusters.

7.3.1 Making $OH^-(Ar)_n$

To make sufficient Ar clusters, it is helpful to have an externally rotatable General Valve and the ability to mix the gases near the origin (throat) of the gas expansion. The tightness of the valve is directly correlated to the spring tension and, therefore, the motion of the poppet retracting from the opening of the faceplate. By changing the valve tension, the characteristics of the gas expansion can be changed. For all previous experiments, the valve tightness was adjusted prior to evacuating the vacuum chamber and could not be adjusted without venting the vacuum chamber. Therefore, a valve that can be rotated external to the vacuum chamber while monitoring the ion intensity is a very important modification. The adjustable valve is implemented by securing the General Valve face plate to the vacuum chamber and rotating the body of the solenoid external to the vacuum chamber. A drawing of the rotatable General Valve holder is shown in Appendix D, Fig. D.1.

In addition to rotating the valve, it is helpful to mix the gases internally. This is done with an entrainment block, which is shown in Fig. D.2 within Appendix D. The entrainment block is based upon designs from Mark Johnson's and Mathias Weber's groups.[156-158] This block has attachments for three General Valve faceplates with the central valve producing the main expansion. The valve design channels the gas from the two side valves into the throat of the main expansion. For our setup, only the main valve is rotated, and all three valves can be independently pulsed. Controlling the individual timings allows the side valves to be pulsed prior to the main valve, which mixes the gases from the side valves with the main-gas expansion. The entrainment block is currently setup to be used only with a beam of electrons from an electron gun; therefore, a magnet is attached to the outside of the block to help guide the electron beam. When the pulsed discharge source is being used as the ionization technique, the rotatable General Valve holder (Fig. D. 1) is used.

Again, various combinations of gases are used in an attempt to make the largest $OH^-(Ar)_n$ clusters. This includes mixing the gases external to the vacuum chamber and using the rotatable-valve holder or the central valve on the entrainment block. There is also the option to have real time mixing with the entrainment block. To make intense $OH^-(Ar)_n$ cluster beams, we tried many of the combinations mentioned earlier and new combinations, such as H_2O_2/Ar, H_2O/Ar, CH_4/N_2O/Ar, C_2H_6/N_2O/Ar, neo-C_5H_{12}/N_2O/Ar, and NH_3/N_2O/Ar, where the external adjustment of the valve is rotated to optimize clustering in both types of holders and with both ionization techniques. The most successful way to make the $OH^-(Ar)_n$ clusters to date has been with the CH_4/N_2O/Ar mixture and a beam of electrons. However, this setup is currently only making up to $n \approx 4$ for the $OH^-(Ar)_n$ clusters, which is not enough to carry out the planned experiments (Eqn. 7.2), as is shown later. The mechanism for making OH^- is multistep:

$N_2O + e^- \rightarrow O^- + N_2$, Eqn. 7.3

$O^- + CH_4 \rightarrow OH^- + CH_3$, Eqn. 7.4

and the OH^- may be forming downstream from the throat of the nozzle where the density of the gas is too low for the Ar to effectively cluster with the OH^-. Therefore, we also tried forming OH^- from directly breaking a bond, such as in methanol, diols, formic acid, etc. In these examples, when OH^- was formed, it did not successfully cluster with Ar. Currently, our best option for forming $OH^-(Ar)_n$ clusters is using a mixture of CH_4/N_2O/Ar ionized by a beam of electrons.

7.3.2 Making O_2 (a $^1\Delta$)

The $OH^-(Ar)_n$ clusters need to collide with O_2 (a $^1\Delta$), Eqn. 7.2, in order to form cis-HO_3^-. It is clear from our previous attempts that large quantities of O_2 (a $^1\Delta$) are not being made in the ionization region but need to be intentionally generated. There are two obvious ways to make excited state O_2: a microwave discharge source and a chemical-based method.[159-163] The microwave discharge produces many other products, such as O and O_3. Therefore, we turn to the chemical based method and setup designed by Viggiano and coworkers.[159,160]

The O_2 (a $^1\Delta$) generator is a chemical-based method that produces both ground and excited state O_2:[159,160,162,163]

$H_2O_2 + Cl_2 + 2KOH \rightarrow O_2$ ($\tilde{X}\ ^3\Sigma$ and a $^1\Delta$) + 2KCl + $2H_2O$. Eqn. 7.5

A schematic of the setup for the production of excited state O_2 is shown on the left side of Fig. 7.4. Chlorine gas bubbles through a chilled, basic solution containing hydrogen peroxide, where

the salt remains behind and the water becomes trapped in a sequential water trap. The flow of the chlorine gas and temperature of the H_2O_2/KOH solution and water trap are varied to maximize O_2 ($a\ ^1\Delta$) generation. The 1270-nm emission from the O_2 ($a\ ^1\Delta$) $\rightarrow$ O_2 ($\tilde{X}\ ^3\Sigma$) transition[164] is monitored in an emission cell that is located between the water trap and the vacuum chamber, where the conversion efficiency is about 15%. Isolated O_2 ($a\ ^1\Delta$) has a ~72 min radiative lifetime;[165-168] however, the excited state of O_2 can be quenched by wall collisions, where collisions on stainless steel surfaces result in more efficient quenching than Teflon and glass.[169] Therefore, the exposure of the O_2 ($a\ ^1\Delta$) molecule to stainless steel, such as the General Valve, is reduced, and Teflon and glass are used whenever possible.

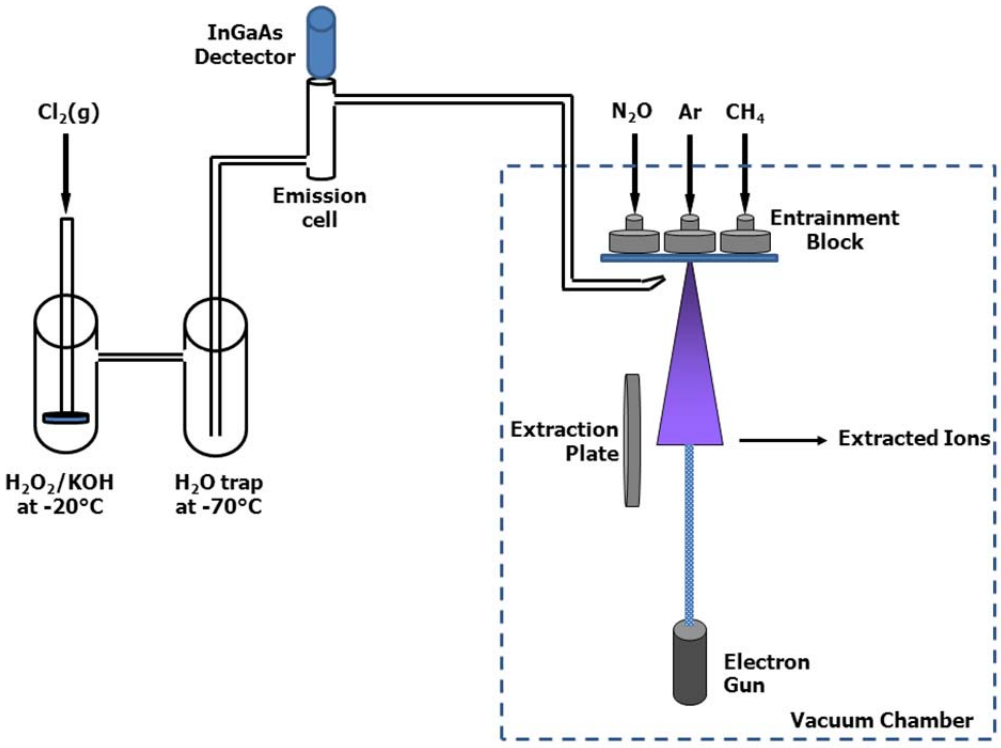

Figure 7.4 Schematic setup for cis-HO_3^- generation. The chemical-based method for producing O_2 (a $^1\Delta$) is shown on the left. Inside the vacuum chamber shows the setup for the entrainment block with three General Valves operating to produce $OH^-(Ar)_n$ clusters. The O_2 (a $^1\Delta$) is introduced by the capillary tube directed into the throat of the expansion.

As can be seen in Fig. 7.4, the O_2 (a $^1\Delta$) is combined with the gas from the entrainment block in an attempt to produce cis-HO_3^- via Eqn. 7.2. The $OH^-(Ar)_n$ clusters are optimized using the entrainment block assembly, where the main expansion is Ar and the side valves contain the CH_4 and N_2O. The glass capillary tube that carries the O_2 into the chamber is directed towards the throat of the gas expansion. The O_2 source is continuous and, therefore, must be leaked slowly into the chamber so that the pumps for the vacuum chamber do not become flooded. To date, the cis-HO_3^- has not been successfully made. However this setup does make $OH^-(O_2)$ when the O_2 is introduced into the source chamber. There may be a few reasons for not making

the desired ion. First, the intensity of the $OH^-(Ar)_n$ clusters might not be enough. Second, we might not be making enough O_2 (a $^1\Delta$). Third, the cis-HO_3^- is calculated to be slightly stable, but perhaps the anion is not stable and, therefore, cannot be made. Before we accept the third possibility, additional efforts will be made to find ways for making larger $OH^-(Ar)_n$ clusters.

7.4 Future Projects

Even if the cis-HO_3^- project is not successful, these improvements and modifications that have been introduced to the experimental setup can be adapted to other chemical investigations. If $OH^-(Ar)_n$ clusters can be made larger, there are other atmospherically relevant species that we would be able to study with this setup, such as HOCO, HONO, $HOCO_2$, or $HOSO_2$. Also, the ability for making large Ar clusters, which we have successfully demonstrated with O^- and $(H_2O)^-_6$, opens additional possibilities. Previous studies by our group and the Johnson group have found that $O^-(CH_4)$ is not stable and forms a trapped $OH^-(CH_3)$ complex.[170] However, if we start with $O^-(Ar)_n$ and displace some of the Ar with a gas pulse of CH_4 that is farther downstream from the gas expansion, then we could form $O^-(Ar)_m(CH_4)$, where n > m. By vibrationally exciting the C–H stretch in the $O^-(Ar)_m(CH_4)$ cluster, the energized cluster could undergo an H-abstraction reaction by O^-. This reaction could be followed in real time by time-resolved photoelectron spectroscopy.

A similar study involves $(H_2O)_6^-(Ar)_n$ clusters combined with nitromethane, NM.[158,171-173] The $(H_2O)_6^-(Ar)_n$ clusters combine with a gas pulse of NM downstream from the expansion. The NM displaces Ar as it gently attaches to the $(H_2O)_6^-$ cluster. NM has a higher electron affinity than $(H_2O)_6$, and energetically the electron favors the NM to produce NM^- solvated by

H_2O. If the displacement of the Ar is gentle enough, the electron stays bound to the H_2O cluster to form $(H_2O)_6^-(NM)$ that we can interrogate in a time-resolved experiment:

$$(H_2O)_6^-(NM) + h\nu_{pump} \rightarrow NM^-(H_2O)_3 + h\nu_{probe} + 3H_2O \rightarrow$$

$$NM(H_2O)_3 + e^- + 3H_2O \qquad \text{Eqn. 7.3}$$

The pump-probe experiment involves exciting the C–H stretch within the NM with an IR pump pulse, which perturbs the $(H_2O)_6^-(NM)$ cluster to initiate the charge transfer to the NM.[158] The probe pulse monitors the time for charge transfer by photodetaching the electron as it transfers to $NM^-(H_2O)_3$. These are only a few examples of new experiments that can be performed in our lab by combining Ar tagging and a gas pulse downstream from the gas expansion.

Bibliography

1. A. Ellis, M. Feher, and T. Wright, *Electronic and photoelectron spectroscopy* (Cambridge University Press, Cambridge, 2005).

2. H. Hotop and W. C. Lineberger, "Binding-energies in atomic negative-ions .2," *J. Phys. Chem. Ref. Data* **14,** 731-50 (1985).

3. P. G. Wenthold and W. C. Lineberger, "Negative ion photoelectron spectroscopy studies of organic reactive intermediates," *Acc. Chem. Res.* **32,** 597-604 (1999).

4. D. M. Neumark, "Transition state spectroscopy," *Science* **272,** 1446-47 (1996).

5. D. M. Neumark, "Slow electron velocity-map imaging of negative ions: Applications to spectroscopy and dynamics," *J. Phys. Chem. A* **112,** 13287-301 (2008).

6. D. M. Neumark, "Probing chemical dynamics with negative ions," *J. Chem. Phys.* **125,** 132303 (2006).

7. A. Sanov and R. Mabbs, "Photoelectron imaging of negative ions," *Int. Rev. Phys. Chem.* **27,** 53-85 (2008).

8. K. M. Ervin and W. C. Lineberger, Photoelectron spectroscopy of molecular anions in *Advances in Gas Phase Ion Chemistry*, Vol. 1, edited by N. G. Adams and L. M. Babcock (JAP Press, Greenwich), p. 121-66 (1992).

9. P. C. Engelking, "Approximate rotational band shifts," *J. Phys. Chem.* **90,** 4544-45 (1986).

10. C. Y. Cha, G. Gantefor, and W. Eberhardt, "New experimental setup for photoelectron spectrocopy on cluster anions," *Rev. Sci. Instrum.* **63,** 5661-66 (1992).

11. J. Cooper and R. N. Zare, "Angular distribution of photoelectrons," *J. Chem. Phys.* **48,** 942-43 (1968).

12. E. P. Wigner, "On the behavior of cross sections near thresholds," *Phys. Rev.* **73,** 1002-09 (1948).

13. K. M. Ervin, PESCAL Fortran Program, 2008.

14. A. W. Castleman and R. G. Keesee, "Gas-phase clusters - spanning the states of matter," *Science* **241,** 36-42 (1988).

15. A. W. Castleman and K. H. Bowen, "Clusters: Structure, energetics, and dynamics of intermediate states of matter," *J. Phys. Chem.* **100,** 12911-44 (1996).

16. M. L. Alexander, N. E. Levinger, M. A. Johnson, D. Ray, and W. C. Lineberger, "Recombination of Br_2^- photodissociated within mass selected ionic clusters," *J. Chem. Phys.* **88,** 6200-10 (1988).

17. K. R. Asmis, T. R. Taylor, C. S. Xu, and D. M. Neumark, "Anion photoelectron spectroscopy of I_2^- and $I_2^-Ar_n$ (n = 1-14, 16, 20) clusters," *J. Chem. Phys.* **109,** 4389-95 (1998).

18. I. Yourshaw, Y. X. Zhao, and D. M. Neumark, "Many-body effects in weakly bound anion and neutral clusters: Zero electron kinetic energy spectroscopy and threshold photodetachment spectroscopy of Ar_nBr^-(n=2-9) and Ar_nI^-(n=2-19)," *J. Chem. Phys.* **105,** 351-73 (1996).

19. C. E. Klots, "The evaporative ensemble," *Z. Phys. D: At, mol. and clus* **5,** 83-89 (1987).

20. W. H. Robertson and M. A. Johnson, "Molecular aspects of halide ion hydration: The cluster approach," *Annu. Rev. Phys. Chem.* **54,** 173-213 (2003).

21. K. F. Willey, P. Y. Cheng, C. S. Yeh, D. L. Robbins, and M. A. Duncan, "Electronic spectroscopy of silver dimer rare-gas complexes," *J. Chem. Phys.* **95,** 6249-56 (1991).

22. M. Z. Kamrath, E. Garand, P. A. Jordan, C. M. Leavitt, A. B. Wolk, M. J. Van Stipdonk, S. J. Miller, and M. A. Johnson, "Vibrational characterization of simple peptides using cryogenic infrared photodissociation of H_2 tagged, mass-selected ions," *J. Am. Chem. Soc.* **133,** 6440-48 (2011).

23. X. B. Wang and L. S. Wang, "Development of a low-temperature photoelectron spectroscopy instrument using an electrospray ion source and a cryogenically controlled ion trap," *Rev. Sci. Instrum.* **79** (2008).

24. L. Sheps, E. M. Miller, and W. C. Lineberger, "Photoelectron spectroscopy of small $IBr^-(CO_2)_n$, (n=0-3) cluster anions," *J. Chem. Phys.* **131,** 064304 (2009).

25. L. Sheps, E. M. Miller, S. Horvath, M. A. Thompson, R. Parson, A. B. McCoy, and W. C. Lineberger, "Solvent-mediated electron hopping: Long-range charge transfer in $IBr^-(CO_2)$ photodissociation," *Science* **328,** 220-24 (2010).

26. L. Sheps, E. M. Miller, S. Horvath, M. A. Thompson, R. Parson, A. B. McCoy, and W. C. Lineberger, "Solvent-mediated charge redistribution in photodissociation of IBr^- and $IBr^-(CO_2)$," *J. Chem. Phys.* **134,** 184311 (2011).

27. A. S. Case, E. M. Miller, J. P. Martin, Y.-J. Lu, L. Sheps, A. B. McCoy, and W. C. Lineberger, "Dynamic mapping of CN rotation following photoexcitation of ICN^- " *Angew. Chem., Int. Ed. Engl.* **51,** 2651-53 (2012).

28. E. M. Miller, L. Sheps, Y. J. Lu, A. S. Case, A. B. McCoy, and W. C. Lineberger, "New view of the ICN A continuum using photoelectron spectroscopy of ICN^-," *J. Chem. Phys.* **136,** 044313 (2012).

29. V. Dribinski, A. Ossadtchi, V. A. Mandelshtam, and H. Reisler, "Reconstruction of abel-transformable images: The Gaussian basis-set expansion abel transform method," *Rev. Sci. Instrum.* **73,** 2634-42 (2002).

30. T. Sanford, S. Y. Han, M. A. Thompson, R. Parson, and W. C. Lineberger, "Photodissociation dynamics of $IBr^-(CO_2)_n$, n < 15," *J. Chem. Phys.* **122,** 054307 (2005).

31. G. J. Rathbone, T. Sanford, D. Andrews, and W. C. Lineberger, "Photoelectron imaging spectroscopy of $Cu^-(H_2O)_{1,2}$ anion complexes," *Chem. Phys. Lett.* **401,** 570-74 (2005).

32. M. A. Johnson and W. C. Lineberger, Pulsed methods for cluster ion spectroscopy in *Techniques for the Study of Gas-Phase Ion-Molecule Reactions*, edited by J. M. Farrar and J. W. Saunders (Wiley, New York), p. 591-636 (1988).

33. T. J. Sanford, Photodissociation Dynamics and Photoelectron Imaging Spectroscopy of Anions and Anion Clusters, Ph.D. Thesis, University of Colorado, Boulder, 2004.

34. D. H. Andrews, Anion Photoelectron Spectroscopy, Ph.D. Thesis, University of Colorado, Boulder, 2006.

35. M. Hillenkamp, S. Keinan, and U. Even, "Condensation limited cooling in supersonic expansions," *J. Chem. Phys.* **118,** 8699-705 (2003).

36. W. C. Wiley and I. H. McLaren, "Time-of-flight mass spectrometer with improved resolution," *Rev. Sci. Instrum.* **26,** 1150-57 (1955).

37. A. Eppink and D. H. Parker, "Velocity map imaging of ions and electrons using electrostatic lenses: Application in photoelectron and photofragment ion imaging of molecular oxygen," *Rev. Sci. Instrum.* **68,** 3477-84 (1997).

38. D. W. Chandler and P. L. Houston, "Two-dimensional imaging of state-selected photodissociation products detected by multiphoton ionization," *J. Chem. Phys.* **87,** 1445-47 (1987).

39. D. H. Parker and A. T. J. B. Eppink, Velocity map imaging: applications in molecular dynamics and experimental aspects in *Imaging in Molecular Dynamics: Technology and Applications*, edited by B. Whitaker (Cambridge University Press, Cambridge) (2003).

40. L. M. Smith and D. R. Keefer, "Abel inversion using transform techniques," *J. Quant. Spectrosc. Radiat. Transfer* **39,** 367-73 (1988).

41. M. Meot-Ner, "The ionic Hydrogen bond," *Chem. Rev.* **105,** 213-84 (2005).

42. A. Sanov and W. C. Lineberger, "Dynamics of cluster anions: a detailed look at condensed-phase interactions," *PhysChemComm* **5,** 165-77 (2002).

43. M. A. Thompson, J. P. Martin, J. P. Darr, W. C. Lineberger, and R. Parson, "A combined experimental/theoretical investigation of the near-infrared photodissociation of $IBr^-(CO_2)_n$," *J. Chem. Phys.* **129,** 224304 (2008).

44. V. Dribinski, J. Barbera, J. P. Martin, A. Svendsen, M. A. Thompson, R. Parson, and W. C. Lineberger, "Time-resolved study of solvent-induced recombination in photodissociated $IBr^-(CO_2)_n$ clusters," *J. Chem. Phys.* **125,** 133405 (2006).

45. M. Thompson, From Femtoseconds to Nanoseconds: Simulations of IBr^- Photodissociation Dynamics in CO_2 clusters, Ph.D Thesis, University of Colorado, 2007.

46. J. O. Clevenger, Q. P. Ray, J. Tellinghuisen, X. Zheng, and M. C. Heaven, "Spectroscopy of metastable species in a free-jet expansion - The β-A transition in IBr," *Can. J. Phys.* **72,** 1294-306 (1994).

47. D. J. Auerbach, M. M. Hubers, A. P. M. Baede, and J. Los, "Chemi-ionization in alkali-heteronuclear halogen collisions: Role of excited molecular ion states," *Chem. Phys.* **2,** 107-18 (1973).

48. S. Patchkovskii, "Ab initio investigation of potential energy curves of the 23 electronic states of IBr correlating to neutral ^{2}P atoms," *Phys. Chem. Chem. Phys.* **8,** 926-40 (2006).

49. D. T. Radzykewycz, C. D. Littlejohn, M. B. Carter, J. O. Clevenger, J. H. Purvis, and J. Tellinghuisen, "The D'- A' transition in IBr - A detperturbation analysis," *J. Mol. Spectrosc.* **166,** 287-303 (1994).

50. D. R. T. Appadoo, P. F. Bernath, and R. J. Leroy, "High-resolution visible spectrum for the $a^3\Pi_1$-$X^1\Sigma^+$ System of IBr," *Can. J. Phys.* **72,** 1265-72 (1994).

51. X. N. Zheng, M. C. Heaven, and J. Tellinghuisen, "Spectroscopy of metastable species in a free-jet expansion - the D'-a' transition of IBr," *J. Mol. Spectrosc.* **164,** 135-51 (1994).

52. T. Yukiya, N. Nishimiya, and M. Suzuki, "High-resolution laser spectroscopy of the $A^3\Pi_1$ <- $X\ ^1\Sigma^+$ system of IBr with a titanium:sapphire ring laser," *J. Mol. Spectrosc.* **214,** 132-43 (2002).

53. M. M. Hubers, A. W. Kleyn, and J. Los, "Ion-pair formation in alkali-halogen collisions at high velocities," *Chem. Phys.* **17,** 303-25 (1976).

54. W. A. Chupka, J. Berkowitz, and D. Gutman, "Electron affinites of halogen diatomic molecules as determined by endoergic charge transfer," *J. Chem. Phys.* **55,** 2724 (1971).

55. C. E. Moore, *Atomic energy levels, 2nd ed.* (National Bureau of Standards, Washington, DC, 1971).

56. M. T. Zanni, T. R. Taylor, B. J. Greenblatt, B. Soep, and D. M. Neumark, "Characterization of the I_2^- anion ground state using conventional and femtosecond photoelectron spectroscopy," *J. Chem. Phys.* **107,** 7613-19 (1997).

57. B. Nelander, V. Sablinskas, M. Dulick, V. Braun, and P. F. Bernath, "High resolution far infrared spectroscopy of IBr using a synchrotron source," *Mol. Phys.* **93,** 137-44 (1998).

58. E. M. Weinstock, "Laser-induced fluorescence of IBr^{79}," *J. Mol. Spectrosc.* **61,** 395-402 (1976).

59. J. Ho, K. M. Ervin, and W. C. Lineberger, "Photoelectron-spectroscopy of metal cluster anions - Cu_n^-, Ag_n^-, and Au_n^-," *J. Chem. Phys.* **93,** 6987-7002 (1990).

60. K. J. Reed, A. H. Zimmerman, H. C. Andersen, and J. I. Brauman, "Cross-sections for photodetachment of electrons from negative-ions near threshold," *J. Chem. Phys.* **64,** 1368-75 (1976).

61. B. M. Hughes, C. Lifshitz, and T. O. Tiernan, "Electron affinites from endothermic negative-ion charge-transfer reactions. 3. NO, NO_2, SO_2, CS_2, Cl_2, Br_2, I_2, and C_2H," *J. Chem. Phys.* **59,** 3162-81 (1973).

62. H. Dispert and K. Lacmann, "Chemionization in alkali-halogen reactions - Evidence for ion formation by alkaki dimers," *Chem. Phys. Lett.* **47,** 533-36 (1977).

63. J. A. Ayala, W. E. Wentworth, and E. C. M. Chen, "Electron-attachment to halogens," *J. Phys. Chem.* **85,** 768-77 (1981).

64. E. Wrede, S. Laubach, S. Schulenburg, A. J. Orr-Ewing, and M. N. R. Ashfold, "Velocity map imaging of the near-threshold photodissociation of IBr: accurate determination of D_e(I-Br)," *Chem. Phys. Lett.* **326,** 22-32 (2000).

65. Y. X. Zhao, C. C. Arnold, and D. M. Neumark, "Study of the $I.CO_2$ van der Waals Complex by Threshold Photodetachment Spectroscopy of I^-CO_2," *J. Chem. Soc., Faraday Trans.* **89,** 1449-56 (1993).

66. H. Gomez, T. R. Taylor, and D. M. Neumark, "Anion photoelectron spectroscopy of $I_2^-(CO_2)_n$(n=1-8) clusters," *J. Chem. Phys.* **116,** 6111-17 (2002).

67. D. W. Arnold, S. E. Bradforth, E. H. Kim, and D. M. Neumark, "Study of $I^-(CO_2)_n$, $Br^-(CO_2)_n$, and $I^-(N_2O)_n$ clusters by anion photoelectron-spectroscopy," *J. Chem. Phys.* **102,** 3510-18 (1995).

68. D. W. Arnold, S. E. Bradforth, E. H. Kim, and D. M. Neumark, "Anion photoelectron-spectroscopy of iodine-carbon dioxide clusters," *J. Chem. Phys.* **97,** 9468-71 (1992).

69. D. W. Arnold, S. E. Bradforth, E. H. Kim, and D. M. Neumark, "Study of halogen carbon-dioxide clusters and the fluoroformyloxyl radical by photodetachment of $X^-(CO_2)$ (X=I,Cl,Br) and FCO_2^-," *J. Chem. Phys.* **102,** 3493-509 (1995).

70. A. Stolow, "Femtosecond time-resolved photoelectron spectroscopy of polyatomic molecules," *Annu. Rev. Phys. Chem.* **54,** 89-119 (2003).

71. A. W. Jasper, S. Nangia, C. Y. Zhu, and D. G. Truhlar, "Non-Born-Oppenheimer molecular dynamics," *Acc. Chem. Res.* **39,** 101-08 (2006).

72. L. J. Butler, "Chemical reaction dynamics beyond the Born-Oppenheimer approximation," *Annu. Rev. Phys. Chem.* **49,** 125-71 (1998).

73. C. T. Middleton, K. de La Harpe, C. Su, Y. K. Law, C. E. Crespo-Hernandez, and B. Kohler, "DNA excited-state dynamics: from single bases to the double helix," *Annu. Rev. Phys. Chem.* **60,** 217-39 (2009).

74. R. W. Schoenlein, L. A. Peteanu, R. A. Mathies, and C. V. Shank, "The 1^{st} step in vision - femtosecond isomerization of rhodopsin," *Science* **254,** 412-15 (1991).

75. C. E. Crespo-Hernandez, B. Cohen, P. M. Hare, and B. Kohler, "Ultrafast excited-state dynamics in nucleic acids," *Chem. Rev.* **104,** 1977-2019 (2004).

76. A. E. Bragg, G. U. Kanu, and B. J. Schwartz, "Nanometer-scale phase separation and preferential solvation in THF-water mixtures: ultrafast electron hydration and recombination dynamics following CTTS excitation of I^-," *J. Phys. Chem. Lett.* **2,** 2797-804 (2011).

77. A. E. Bragg, M. C. Cavanagh, and B. J. Schwartz, "Linear response breakdown in solvation dynamics induced by atomic electron-transfer reactions," *Science* **321,** 1817-22 (2008).

78. R. Parson, J. Faeder, and N. Delaney, "Charge flow and solvent dynamics in the photodissociation of solvated molecular ions," *J. Phys. Chem. A* **104,** 9653-65 (2000).

79. J. M. Papanikolas, V. Vorsa, M. E. Nadal, P. J. Campagnola, H. K. Buchenau, and W. C. Lineberger, "I_2^- photodissociation and recombination dynamics in size-selected $I_2^-(CO_2)_n$ Cluster Ions," *J. Chem. Phys.* **99,** 8733-50 (1993).

80. J. M. Papanikolas, J. R. Gord, N. E. Levinger, D. Ray, V. Vorsa, and W. C. Lineberger, "Photodissociation and geminate recombination dynamics of I_2^- in mass-selected $I_2^-(CO_2)_n$ Cluster Ions," *J. Phys. Chem.* **95,** 8028-40 (1991).

81. M. E. Nadal, P. D. Kleiber, and W. C. Lineberger, "Photofragmentation of mass-selected $ICI^-(CO_2)_n$ cluster ions: Solvation effects on the structure and dynamics of the ionic chromophore," *J. Chem. Phys.* **105,** 504-14 (1996).

82. N. Delaney, J. Faeder, and R. Parson, "Simulation of UV photodissociation of $I_2^-(CO_2)_n$: Spin-orbit quenching via solvent mediated electron transfer," *J. Chem. Phys.* **111,** 651-63 (1999).

83. T. Sanford, D. Andrews, J. Rathbone, M. Taylor, F. Muntean, M. Thompson, A. B. McCoy, R. Parson, and W. C. Lineberger, "Time resolved solvent rearrangement dynamics," *Faraday Discuss.* **127,** 383-94 (2004).

84. R. Mabbs, K. Pichugin, and A. Sanov, "Time-resolved imaging of the reaction coordinate," *J. Chem. Phys.* **122,** 174305 (2005).

85. S. Horvath, R. M. Pitzer, and A. B. McCoy, "Theoretical Investigations of the time-resolved photodissociation dynamics of IBr^-," *J. Phys. Chem. A* **114,** 11337-46 (2010).

86. S. Horvath, Spectroscopy and Dynamics of Weakly-Bound Anions using Full- and Reduced-dimensional Theoretical Methods, Ph.D. Thesis, The Ohio State Univeristy, 2010.

87. P. E. Maslen, J. Faeder, and R. Parson, "An effective Hamiltonian for an electronically excited solute in a polarizable molecular solvent," *Mol. Phys.* **94,** 693-706 (1998).

88. J. Faeder, N. Delaney, P. E. Maslen, and R. Parson, "Modeling structure and dynamics of solvated molecular ions: Photodissociation and recombination in $I_2^-(CO_2)_n$," *Chem. Phys.* **239,** 525-47 (1998).

89. H.-J. Werner, P. J. Knowles, R. Lindh, F. R. Manby, M. Shültz, P. Celani, T. Korona, A. Mitrushenkov, G. Rauhut, T. B. Adler, R. D. Amos, A. Bernhardsson, A. Berning, D. L. Cooper, M. J. O. Deegan*, et. al.*, MOLPRO, version 2002.6 (2003).

90. H. C. Andersen, "Molecular-dynamics simulations at constant pressure and-or temperature," *J. Chem. Phys.* **72,** 2384-93 (1980).

91. J. C. Tully, "Molecular-dynamics with electronic-transitions," *J. Chem. Phys.* **93,** 1061-71 (1990).

92. S. Hammes-Schiffer and J. C. Tully, "Proton-transfer in solution - molecular-dynamics with quantum transitions," *J. Chem. Phys.* **101,** 4657-67 (1994).

93. H.-J. Werner, P. J. Knowles, R. Lindh, F. R. Manby, M. Shültz, P. Celani, T. Korona, A. Mitrushenkov, G. Rauhut, T. B. Adler, R. D. Amos, A. Bernhardsson, A. Berning, D. L. Cooper, M. J. O. Deegan*, et. al.*, MOLPRO 1, (2008).

94. K. A. Peterson, B. C. Shepler, D. Figgen, and H. Stoll, "On the spectroscopic and thermochemical properties of ClO, BrO, IO, and their anions," *J. Phys. Chem. A* **110,** 13877-83 (2006).

95. K. A. Peterson, D. Figgen, E. Goll, H. Stoll, and M. Dolg, "Systematically convergent basis sets with relativistic pseudopotentials. II. Small-core pseudopotentials and correlation consistent basis sets for the post-d group 16-18 elements," *J. Chem. Phys.* **119,** 11113-23 (2003).

96. P. Wernet, M. Odelius, K. Godehusen, J. Gaudin, O. Schwarzkopf, and W. Eberhardt, "Real-time evolution of the valence electronic structure in a dissociating molecule," *Phys. Rev. Lett.* **103,** 013001 (2009).

97. D. T. Colbert and W. H. Miller, "A novel discrete variable representation for quantum-mechanical reactive scattering via the s-matrix Kohn Method," *J. Chem. Phys.* **96,** 1982-91 (1992).

98. Z. Bacic and J. C. Light, "Theoretical methods for rovibrational staets of floppy molecules," *Annu. Rev. Phys. Chem.* **40,** 469-98 (1989).

99. V. S. Batista, M. T. Zanni, B. J. Greenblatt, D. M. Neumark, and W. H. Miller, "Femtosecond photoelectron spectroscopy of the I_2^- anion: A semiclassical molecular dynamics simulation method," *J. Chem. Phys.* **110,** 3736-47 (1999).

100. M. S. Taylor, J. Barbera, C. P. Schulz, F. Muntean, A. B. McCoy, and W. C. Lineberger, "Femtosecond dynamics of $Cu(H_2O)_2$," *J. Chem. Phys.* **122,** 054310 (2005).

101. F. Muntean, M. S. Taylor, A. B. McCoy, and W. C. Lineberger, "Femtosecond study of $Cu(H_2O)$ dynamics," *J. Chem. Phys.* **121,** 5676-87 (2004).

102. W. P. Hess and S. R. Leone, "Absolute I* quantum yields for the ICN A-state by diode-laser gain-vs-absorption spectroscopy," *J. Chem. Phys.* **86,** 3773-80 (1987).

103. J. F. Black, J. R. Waldeck, and R. N. Zare, "Evidence for 3 interacting potential-energy surfaces in the photodissociation of ICN at 249 nm," *J. Chem. Phys.* **92,** 3519-38 (1990).

104. W. M. Pitts and A. P. Baronavski, "Wavelength dependence of the $I(5^2P_{1/2,3/2})$ branching ration from ICN A state photolysis," *Chem. Phys. Lett.* **71,** 395-99 (1980).

105. J. H. Ling and K. R. Wilson, "Photofragment spectrum of ICN," *J. Chem. Phys.* **63,** 101-09 (1975).

106. W. J. Marinelli, N. Sivakumar, and P. L. Houston, "Photodissociation dynamics of nozzle-cooled ICN," *J. Phys. Chem.* **88,** 6685-92 (1984).

107. I. Nadler, D. Mahgerefteh, H. Reisler, and C. Wittig, "The 266 nm photolysis of ICN - recoil velocity anisotropies and nascent E, V, R, T exciations for the CN + ($^2P_{3/2}$) and CN + I($^2P_{1/2}$) channels," *J. Chem. Phys.* **82,** 3885-93 (1985).

108. G. E. Hall, N. Sivakumar, and P. L. Houston, "Rotational alignment of the CN fragment of ICN photodissociation," *J. Chem. Phys.* **84,** 2120-28 (1986).

109. S. Yabushita and K. Morokuma, "Abinitio potential-energy surfaces for rotational-excitation of CN product in the A-band photodissociation of ICN," *Chem. Phys. Lett.* **175,** 518-24 (1990).

110. Y. Amatatsu, S. Yabushita, and K. Morokuma, "Ab-Initio potential-energy surfaces and trajectory studies of A-band photodissociation dynamics - ICN* to I+CN and I*+CN," *J. Chem. Phys.* **100,** 4894-909 (1994).

111. A. C. Moskun and S. E. Bradforth, "Photodissociation of ICN in polar solvents: Evidence for long lived rotational excitation in room temperature liquids," *J. Chem. Phys.* **119,** 4500-15 (2003).

112. C. A. Rivera, N. Winter, R. V. Harper, I. Benjamin, and S. E. Bradforth, "The dynamical role of solvent on the ICN photodissociation reaction: connecting experimental observables directly with molecular dynamics simulations," *Phys. Chem. Chem. Phys.* **13,** 8269-83 (2011).

113. A. I. Krylov and R. B. Gerber, "Photodissociation of ICN in solid and in liquid Ar - Dynamics of the cage effect and of excited-state isomerization," *J. Chem. Phys.* **100,** 4242-52 (1994).

114. N. Winter, I. Chorny, J. Vieceli, and I. Benjamin, "Molecular dynamics study of the photodissociation and photoisomerization of ICN in water," *J. Chem. Phys.* **119,** 2127-43 (2003).

115. N. Winter and I. Benjamin, "Photodissociation of ICN at the liquid/vapor interface of water," *J. Chem. Phys.* **121,** 2253-63 (2004).

116. J. Helbing, M. Chergui, S. Fernandez-Alberti, J. Echave, N. Halberstadt, and J. A. Beswick, "Caging and excited state emission of ICN trapped in cryogenic matrices: experiment and theory," *Phys. Chem. Chem. Phys.* **2,** 4131-38 (2000).

117. J. Helbing and M. Chergui, "Spectroscopy and photoinduced dynamics of ICN and its photoproducts in solid argon," *J. Phys. Chem. A* **104,** 10293-303 (2000).

118. Y. Amatatsu and K. Morokuma, "A theoretical-study on the photochemical-reaction of ICN in liquid Ar," *Chem. Phys. Lett.* **245,** 469-74 (1995).

119. M. L. Costen, S. W. North, and G. E. Hall, "Vector signatures of adiabatic and diabatic dynamics in the photodissociation of ICN," *J. Chem. Phys.* **111,** 6735-49 (1999).

120. M. L. Costen and G. E. Hall, "Coherent and incoherent orientation and alignment of ICN photoproducts," *Phys. Chem. Chem. Phys.* **9,** 272-87 (2007).

121. G. Cazzoli, C. D. Esposti, and P. G. Favero, "Equilibrium structure of cyanogen iodide," *J. Mol. Struct.* **48,** 1-8 (1978).

122. A. B. McCoy, "Potential energy surfaces and properties of ICN^- and ICN," *Int. J. Quantum Chem.* **DOI: 10.1002/qua.24011** (2012).

123. B. Bak and A. Hillebert, "Cyanogen Iodide," *Org. Synth.* **Collectives vol. 4,** 207 (1963).

124. S. Hemple and E. R. Nixon, "Infrared spectrum of cyanogen iodide," *J. Chem. Phys.* **47,** 4273 (1967).

125. S. Hemple and E. R. Nixon, "correction," *J. Chem. Phys.* **48,** 5288 (1968).

126. J. A. Blazy, B. M. Dekoven, T. D. Russell, and D. H. Levy, "Binding-energy of iodine rare-gas VanderWaals molecules," *J. Chem. Phys.* **72,** 2439-44 (1980).

127. M. Mladenovic and Z. Bacic, "Rovibrational states of Ar-HCN Van der Waals complex, A localized representation calculation," *J. Chem. Phys.* **94,** 4988-5003 (1991).

128. S. E. Bradforth, E. H. Kim, D. W. Arnold, and D. M. Neumark, "Photoelectron-spectroscopy of CN^-, NCO^-, and NCS^-," *J. Chem. Phys.* **98,** 800-10 (1993).

129. J. P. Martin, Q. Gu, A. S. Case, J. P. Darr, A. B. McCoy, and W. C. Lineberger, "Photodissociation of a solvated triatomic pseudo-dihalide: absorption cross section and dynamics of bare and solvated ICN^-," *J. Chem. Phys.* **in progress** (2012).

130. V. Vorsa, S. Nandi, P. J. Campagnola, M. Larsson, and W. C. Lineberger, "Photodissociation dynamics of mass-selected anions and anionic clusters," *J. Chem. Phys.* **106** (1997).

131. D. J. Goebbert and A. Sanov, "Photodetachment, photofragmentation, and fragment autodetachment of $[O_{2n}(H_2O)_m]^-$ clusters: Core-anion structures and fragment energy partitioning," *J. Chem. Phys.* **131,** 104308 (2009).

132. F. Lepine, B. Baguenard, B. Concina, M. A. Lebeault, and C. Bordas, "From molecular autoionization to thermionic emission," *Mol. Phys.* **105,** 1631-41 (2007).

133. B. Baguenard, J. C. Pinare, F. Lepine, C. Bordas, and M. Broyer, "Thermionic emission in small carbon cluster anions," *Chem. Phys. Lett.* **352,** 147-53 (2002).

134. E. Surber and A. Sanov, "Imaging of direct photodetachment and autodetachment of $(OCS)_2^-$: Excited-state dynamics of the covalent dimer anion," *Phys. Rev. Lett.* **90,** 093001 (2003).

135. R. J. Li, K. A. Hanold, M. C. Garner, A. K. Luong, and R. E. Continetti, "Excited state dynamics in clusters of oxygen," *Faraday Discuss.* **108,** 115-30 (1997).

136. X. P. Xing, X. B. Wang, and L. S. Wang, "Photoelectron Imaging of Doubly Charged Anions, $^-O_2C(CH_2)_nCO_2^-$ (n=2-8): Observation of near 0 eV electrons due to secondary dissociative autodetachment," *J. Phys. Chem. A* **114,** 4524-30 (2010).

137. C. L. Adams, H. Schneider, and J. M. Weber, "Vibrational autodetachment-intramolecular vibrational relaxation translated into electronic motion," *J. Phys. Chem. A* **114,** 4017-30 (2010).

138. I. S. A. Isaksen, C. Granier, G. Myhre, T. K. Berntsen, S. B. Dalsoren, M. Gauss, Z. Klimont, R. Benestad, P. Bousquet, W. Collins, T. Cox, V. Eyring, D. Fowler, S. Fuzzi, P. Jockel*, et. al.*, "Atmospheric composition change: Climate-chemistry interactions," *Atmos. Envrion.* **43,** 5138-92 (2009).

139. I. S. A. Isaksen and S. B. Dalsoren, "Getting a better estimate of an atmospheric radical," *Science* **331,** 38-39 (2011).

140. C. Murray, E. L. Derro, T. D. Sechler, and M. I. Lester, "Weakly bound molecules in the atmosphere: A case study of HOOO," *Acc. Chem. Res.* **42,** 419-27 (2009).

141. S. D. Le Picard, M. Tizniti, A. Canosa, I. R. Sims, and I. W. M. Smith, "The thermodynamics of the elusive HO_3 Radical," *Science* **328,** 1258-62 (2010).

142. M. E. Varner, M. E. Harding, J. Vazquez, J. Gauss, and J. F. Stanton, "Dissociation energy of the HOOO radical," *J. Phys. Chem. A* **113,** 11238-41 (2009).

143. J. Stanton, private communitcation, 2011.

144. M. Varner, private communication, 2011.

145. J. M. Beames, M. I. Lester, C. Murray, M. E. Varner, and J. F. Stanton, "Analysis of the HOOO torsional potential," *J. Chem. Phys.* **134** (2011).

146. A. B. McCoy, private communication, 2010 and 2011.

147. E. Kraka, D. Cremer, J. Koller, and B. Plesnicar, "Peculiar structure of the $HOOO^-$ anion," *J. Am. Chem. Soc.* **124,** 8462-70 (2002).

148. G. Herzberg, *Molecular spectra and molecular structure: I. spectra of diatomic molecules*, 2nd ed. (Van Nostrand Reinhold Company, NY, 1950).

149. J. B. Kim, P. G. Wenthold, and W. C. Lineberger, "Photoelectron spectroscopy of $OH^-(N_2O)$(n=1-5)," *J. Chem. Phys.* **108,** 830-37 (1998).

150. J. R. Smith, J. B. Kim, and W. C. Lineberger, "High-resolution threshold photodetachment spectroscopy of OH^-," *Phys. Rev. A* **55,** 2036-43 (1997).

151. D. L. Osborn, D. J. Leahy, D. R. Cyr, and D. M. Neumark, "Photodissociation spectroscopy and dynamics of the $N_2O_2^-$ anion," *J. Chem. Phys.* **104,** 5026-39 (1996).

152. K. Suma, Y. Sumiyoshi, and Y. Endo, "The rotational spectrum and structure of the HOOO radical," *Science* **308,** 1885-86 (2005).

153. K. Suma, Y. Sumiyoshi, and Y. Endo, "The rotational spectrum and structure of HOOOH," *J. Am. Chem. Soc.* **127,** 14998-99 (2005).

154. F. Cacace, R. Cipollini, G. de Petris, and A. Troiani, "The impervious route to the elusive $HOOO^-$ anion," *Int. J. Mass Spectrom.* **228,** 717-22 (2003).

155. M. C. McCarthy, V. Lattanzi, D. Kokkin, O. Martinez, and J. F. Stanton, "On the molecular structure of HOOO," *J. Chem. Phys.* **136** (2012).

156. J. M. Weber, private communication, 2011.

157. W. H. Robertson, J. A. Kelley, and M. A. Johnson, "A pulsed supersonic entrainment reactor for the rational preparation of cold ionic complexes," *Rev. Sci. Instrum.* **71,** 4431-34 (2000).

158. M. Johnson, private communication, 2011.

159. A. Midey, I. Dotan, J. V. Seeley, and A. A. Viggiano, "Reactions of small negative ions with O_2 ($a\ ^1\Delta_g$) and O_2 ($X\ ^3\Sigma^{-g}$)," *Int. J. Mass Spectrom.* **280,** 6-11 (2009).

160. A. Midey, I. Dotan, S. Lee, W. T. Rawlins, M. A. Johnson, and A. A. Viggiano, "Kinetics for the reactions of O^- and O_2^- with O_2 ($a^1\Delta_g$) measured in a selected ion flow tube at 300 K," *J. Phys. Chem. A* **111,** 5218-22 (2007).

161. D. G. Leopold, K. K. Murray, A. E. S. Miller, and W. C. Lineberger, "Methylene - A study of the $X\ ^3B_1$ and $A\ ^1A_1$ states by photoelectron-spectroscopy of CH_2^- and CD_2^-," *J. Chem. Phys.* **83,** 4849-65 (1985).

162. H. H. Seliger, "A photoelectric method for the measurement of spectra of light sources of rapidly varying intensities," *Anal. Biochem.* **1,** 60-65 (1960).

163. W. E. McDermott, N. R. Pchelkin, D. J. Benard, and R. R. Bousek, "Electronic-transition chemical-laser," *Appl. Phys. Lett.* **32,** 469-70 (1978).

164. R. M. Badger, A. C. Wright, and R. F. Whitlock, "Absolute intensities of discrete and continuous absorption bands of oxygen gas at 1.26 and 1.065 μ and radiative lifetime of $^1\Sigma_g$ state of oxygen," *J. Chem. Phys.* **43,** 4345-50 (1965).

165. C. Schweitzer and R. Schmidt, "Physical mechanisms of generation and deactivation of singlet oxygen," *Chem. Rev.* **103,** 1685-757 (2003).

166. O. Spalek, J. Kodymova, P. Stopka, and I. Micek, "Experimental verification of the Einstein A-coefficient used for evaluation of $O_2(^1\Delta_g)$ concentration in the chemical oxygen-iodine laser," *J. Phys. B: At., Mol. Opt. Phys.* **32,** 1885-92 (1999).

167. H. C. Miller, J. E. McCord, J. Choy, and G. D. Hager, "Measurement of the radiative lifetime of $O_2(a^1\Delta_g)$ using cavity ring down spectroscopy," *J. Quant. Spectrosc. Radiat. Transfer* **69,** 305-25 (2001).

168. S. M. Newman, A. J. Orr-Ewing, D. A. Newnham, and J. Ballard, "Temperature and pressure dependence of line widths and integrated absorption intensities for the O_2 $a^1\Delta_g$ - $X^3\Sigma_g$ (0,0) transition," *J. Phys. Chem. A* **104,** 9467-80 (2000).

169. N. Eyet and A. A. Viggiano, private communication, 2011.

170. E. G. Diken, G. H. Weddle, J. M. Headrick, J. M. Weber, and M. A. Johnson, "Argon cluster-mediated trapping and vibrational spectroscopic characterization of an OH^-HCH_2 intermediate in the O^- + CH_4 reaction," *J. Phys. Chem. A* **108,** 10116-21 (2004).

171. R. Nakanishi and T. Nagata, "Formation and photodestruction of dual dipole-bound anion $(H_2O)_6\{e^-\}CH_3NO_2$," *J. Chem. Phys.* **130,** 224309 (2009).

172. H. Motegi, T. Takayanagi, T. Tsuneda, K. Yagi, R. Nakanishi, and T. Nagata, "Theoretical study on the excess electron binding mechanism in the $(CH_3NO_2)(H_2O)_n^-$ (n=1-6) Anion Clusters," *J. Phys. Chem. A* **114,** 8939-47 (2010).

173. J. C. Marcum and J. M. Weber, "Microhydration of nitromethane anions from both a solute and solvent perspective," *J. Phys. Chem. A* **114,** 8933-38 (2010).

Appendix A: Making the Infinity Spatial Filter

Making the spatial filter:

Figure A.1 shows the drawing for making the pyrex tube and aperture. The aperture can be ordered from Woodburn Diamond Die, Inc. (phone: 260-632-4217), Fig. A2. The purchase order for the aperture can be found on common and in the VMI lab's filing cabinet. The lenses on each end of the spatial filter are described in the drawing made by Coherent, Inc. The last batch of lenses was purchased at Rainbow Research Optics, Inc. (phone: 303-371-3000). The lens purchase order can be found on common and in the VMI lab's filing cabinet. Once you have the body of the spatial filter (pyrex tube with aperture attached in the middle) and the lenses you can begin making the spatial filter.

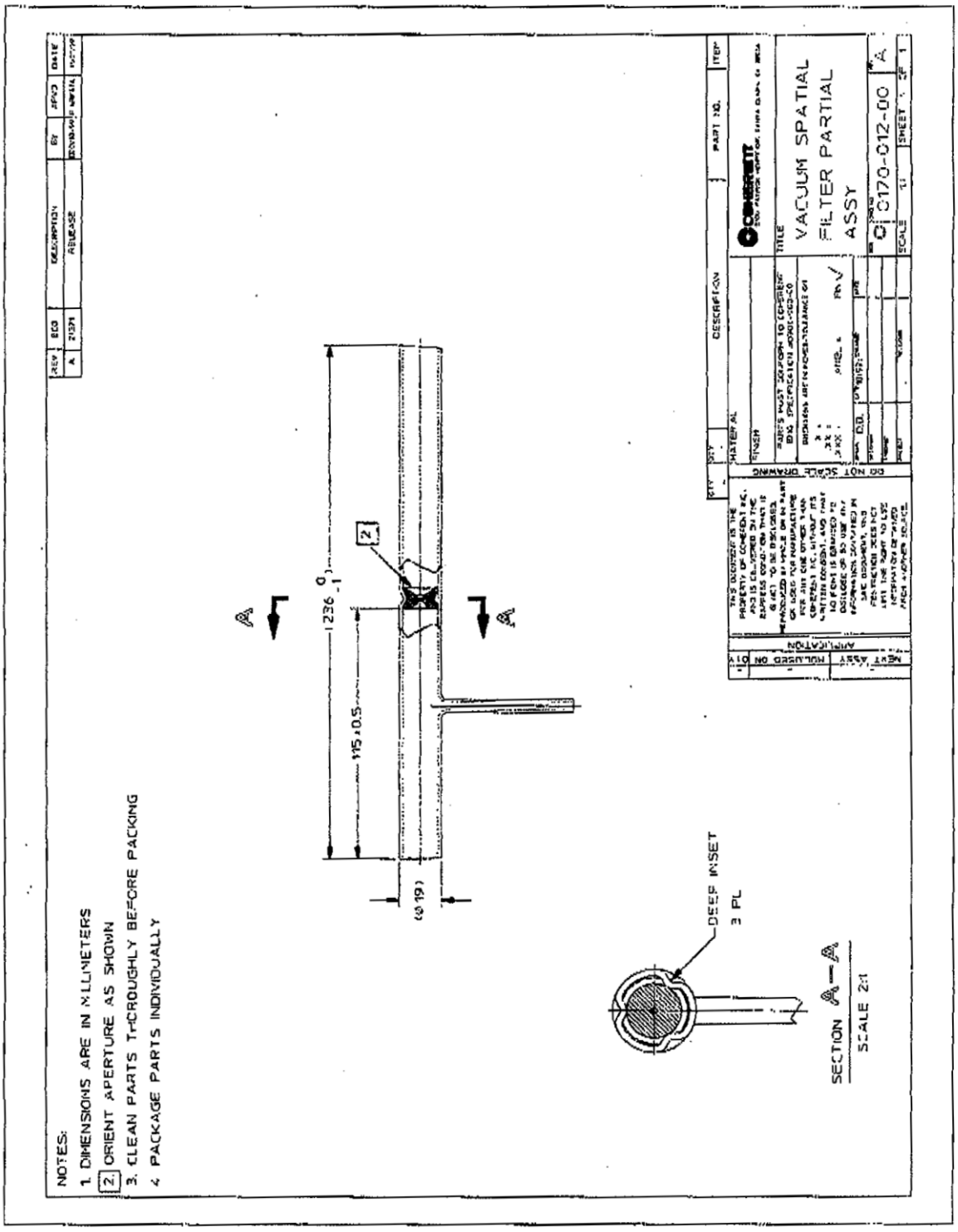

Figure A.1 The drawing for the pyrex tube and aperture.

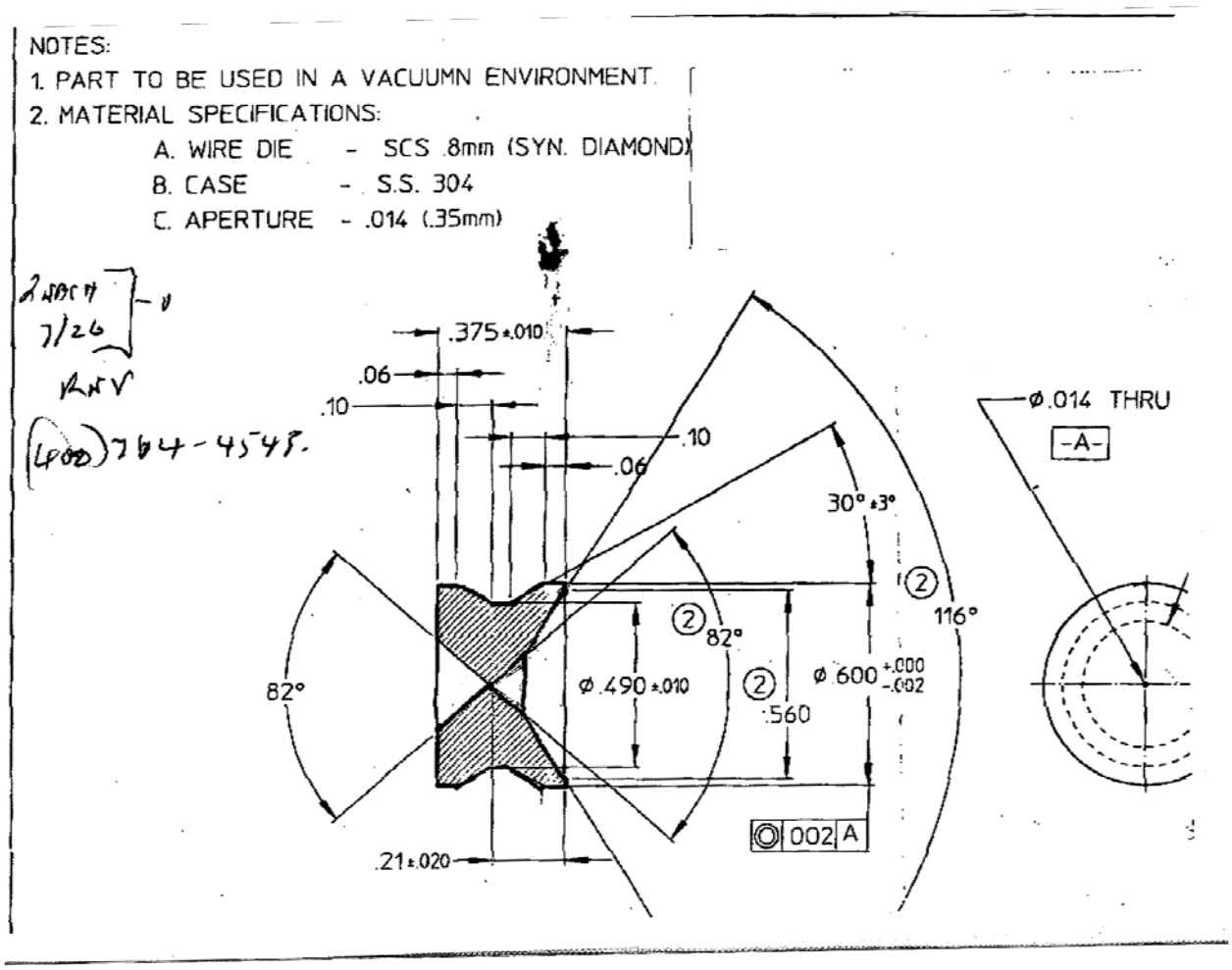

Figure A.2 The drawing for the aperture only.

Below is the procedure for placing the lenses on the pyrex tube with the aperture already in place. Figure A.3 shows the setup in a clean room. The breadboard is secured to the table. The three pictures, (a) – (c), are different views of the setup and will be helpful to refer to throughout the procedure.

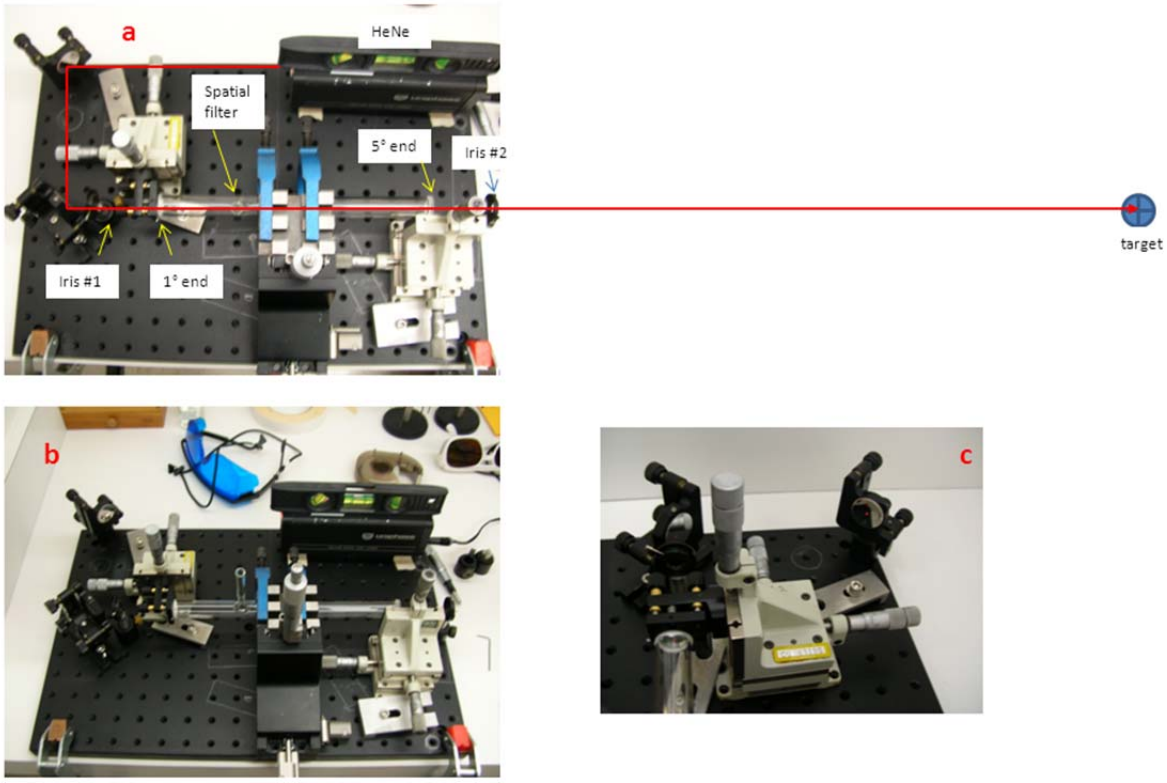

Figure A.3 (a) – (c) show three different views of the setup for attaching the lenses to the spatial filter body. (c) shows how the homemade optic holder is mounted to the translation stage.

- Must be done in a clean room or a room where dust is minimized
- Clean the spatial filter with acetone and methanol then bake (do not bake over 150°C because the Torr Seal holding the aperture will undergo a chemical reaction)
- Need the HeNe parallel to the table. Do this by setting the height of the HeNe with two irises (iris #1 and #2). Have a target as far away from setup as possible
- Place the spatial filter on a translation stage and ensure that it is parallel to the table. In the picture, we have mounted the spatial filter in a V-block and then mounted the V-block

to the translation stage (making sure it was parallel to the table). Ensure that the 5° bend is closest to iris #2 and the 1° bend is closest to iris #1

- Center the spatial filter aperture on the HeNe. The light should be near the center on both the entrance and exit of the tube. (There is no guarantee that the pinhole is centered, so the light might not be exactly centered on the tube but still be centered on the aperture)
- Mount the lens on the 5° end first.
    - The lens needs to be mounted on a 3D translation stage that allows for manipulation of the lens. We have made an optic holder for the correct dimensions of the lens and epoxied the optic mount to the translation stage. (See the close-up picture in Fig. A.3c)
    - Set the lens at the correct angle by matching it to the angle of the tube.
    - Then translate the lens to bring the HeNe spot back onto the target. Check that the angle still looks good.
    - Before torr sealing the lens, practice moving the lens up to the end of the tube and then retracting. Know exactly the micrometer position that the translation stage needs to be in order to make a connection. Practice, practice, practice! When you are confident, retract the stage one more time, apply torr seal to the tube, and bring the lens back to the predetermined micrometer position! Allow to dry for 24 hours. Do not move the stage until the other lens is mounted and dried!!
- Mount the lens on the 1° end second

    - do the same procedure as above. Allow to dry for 24 hours

- remove lenses from optic mounts
- apply a bead of torr-seal around lens and pyrex on both sides to make a solid seal
- allow to dry for 24 hours
- Leak test
- Pull vacuum on spatial filter (needs to be less than $1x10^{-6}$ Torr) and flame seal it!
- Put in laser and go through alignment procedure in Infinity manual.

Appendix B: Nanosecond Laser System Timing Scheme for SRS boxes

Table B.1 Nanosecond laser system timing scheme for SRS boxes. Mass gate not used.

Left Box				
I/O	**Description**	**Value**	**Output to**	**Output Type**
EXT TRIG	external trigger input	n/a	none	n/a
To	time zero output	0	right box	50 ohm / TTL / normal
A	general valve open pulse	To+~1.5ms	none	n/a
B	general valve close pulse	A + ~300 μs	none	n/a
A high B	general valve open time pulse	~300 μs	IOTA ONE valve driver	HighZ / TTL
A low B	not used	n/a	none	n/a
C	ion extraction plate pulse	A + ~900 μs	extraction plate pulser *and* DEI Controller PVX 4140 Trigger	50 ohm / TTL / normal
D	mass gate open pulse	C + ~30 μs	NIM rack mass gate trigger close	HighZ / TTL / normal
C high D	mass gate open time pulse	~30 μs	NIM rack mass gate trigger open	HighZ / TTL
C low D	scope trigger	~30 μs	Channel 4 on scope	HighZ / TTL
Right Box				
I/O	**Description**	**Value**	**Output to**	**Output Type**
EXT TRIG	external trigger input	n/a	from Left Box	n/a
To	not used	n/a	none	n/a
A	Infinity Lamp Trigger	B - 301.1 μs	Infinity LAMP TRIG	50 ohm / TTL / Inverted
B	Infinity Q-Switch Trigger	To + 2.511707ms	Infinity QS TRIG	50 ohm / TTL / Inverted
A high B	not used	n/a	none	n/a
A low B	not used	n/a	none	n/a
C	electron extraction plate	B + 130ns	DEI Controller PVM 4210 Trigger In	50 ohm / TTL / normal
D	MCP ON pulse	B - 2.5 μs	DEI Controller PVM 4140 Trigger In	50 ohm / TTL / normal
C high D	not used	n/a	none	n/a
C low D	not used	n/a	none	n/a

Appendix C: Femtosecond Laser System Timing Scheme for SRS boxes

Table C.1 Femtosecond laser system timing scheme for SRS boxes. Mass gate not used.

Left Box				
I/O	**Description**	**Value**	**Output to**	**Output Type**
EXT TRIG	external trigger input	n/a	from fs laser, triggered at 100Hz	n/a
To	time zero output	0	right box	high Z / TTL / normal
A	general valve open pulse	To + ~1.5ms	none	n/a
B	general valve close pulse	A + ~300 μs	none	n/a
A high B	general valve open time pulse	~300 μs	IOTA ONE valve driver	HighZ / TTL
A low B	not used	~300 μs	none	n/a
C	ion extraction plate pulse	A + ~1ms	extraction plate pulser *and* DEI Controller PVX 4140 Trigger	50 ohm / TTL / normal
D	mass gate open pulse	C + ~30 μs	NIM rack mass gate trigger open	HighZ / TTL / normal
C high D	mass gate open time pulse	~30 μs	NIM rack mass gate trigger close	HighZ / TTL
C low D	analog scope trigger	~30 μs	Channel 4 on scope	HighZ / TTL
Right Box				
I/O	**Description**	**Value**	**Output to**	**Output Type**
EXT TRIG	external trigger input	n/a	from Left Box	n/a
To	not used	n/a	none	n/a
A	not used	To + 2.5 ms	none	n/a
B	not used	A+ 1 ms	none	n/a
A high B	not used	1 ms	none	n/a
A low B	photodiode trigger	1 ms	photodiode trigger	high Z / TTL
C	electron extraction plate	To + 2.51185 ms	DEI Controller PVM 4210 Trigger In	50 ohm / TTL / normal
D	MCP ON pulse	To + 2.508 ms	DEI Controller PVM 4140 Trigger In	50 ohm / TTL / normal
C high D	digital scope trigger	-3 μs	digital scope	high Z / TTL
C low D	not used	-3 μs	none	n/a

Appendix D: General Valve Holders

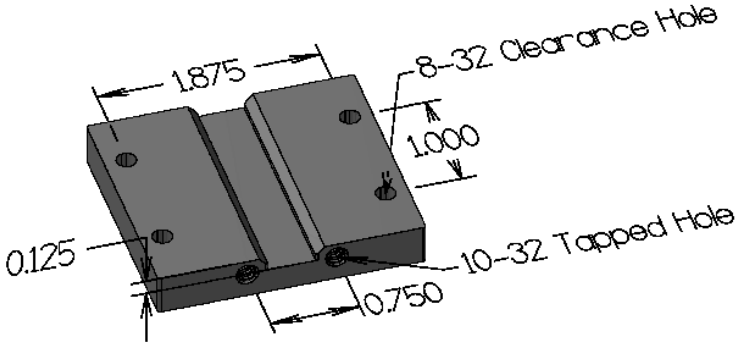

Figure D.1 Drawing of the adjustable-valve holder for General Valve. The two holes on the front are tapped and secure the bottom of the General Valve faceplate. The groove down the center is cut out so that the body of the solenoid can rotate freely. This holder is attached to a metal block inside the chamber through four 8-32 screws.

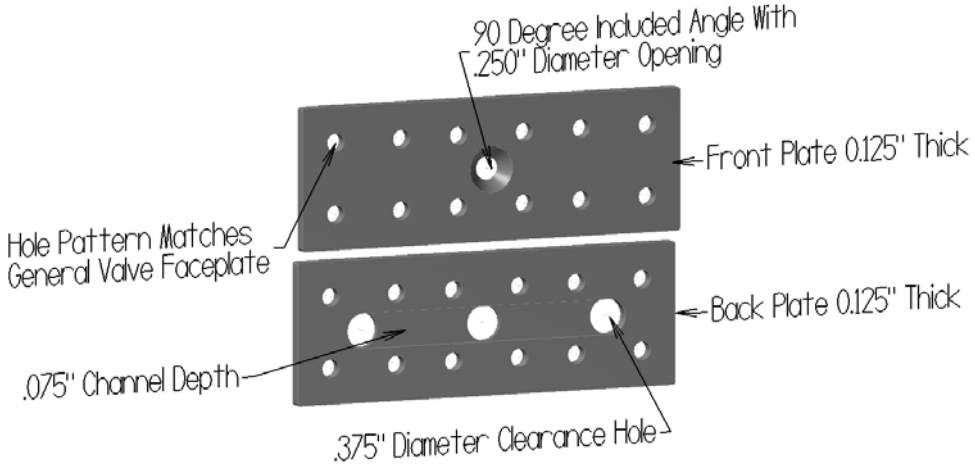

Figure D.2 Drawing of the entrainment-block assembly. The front and back plates are held together with three General Valves by using a nut and bolt for each of the clearance holes. The top drawing is the front of the entrainment block. Only a hole is cut out for the central valve, which produces the main expansion. The bottom drawing is the back of the entrainment block. The three faceplates attach to the reverse side that is shown. The side of the entrainment block that is shown has a groove cutout for the gases introduced by the two end valves; therefore, the gases produced from the two side valves are entrained into the main expansion.